The Massive Star Population in M101

A DISSERTATION
SUBMITTED TO THE FACULTY OF THE GRADUATE SCHOOL
OF THE UNIVERSITY OF MINNESOTA
BY

Skyler H. Grammer

IN PARTIAL FULFILLMENT OF THE REQUIREMENTS
FOR THE DEGREE OF
Doctor of Philosophy

Roberta M. Humphreys, Advisor

August, 2014

Acknowledgements

I would like to first acknowledge my adviser, Roberta Humphreys, for her years of tutelage. She has always been there to impart her knowledge or correct my course when I have gone astray. Over the years, she has always treated me with the utmost respect; never did she make me feel like an underling. Roberta has always afforded me the freedom to pursue my scientific interests, even when they did not necessarily align with her own. I am greatly appreciative of her guidance and support.

The entire University of Minnesota Astrophysics graduate-student body, past and present, also deserve my gratitude. Unlike many other graduate departments, the grads here have always been supportive, friendly, have encouraged camaraderie, and facilitated the transfer of knowledge.

Though remotely, my friends and family have provided me with constant support and understanding when I was busy and communication became sparse. Particularly, I am grateful to my parents and Dylan Morgan for our frequent chats about science, nonsense, relationships, and climbing.

Locally, I am grateful to the Gordon twins. Mike's friendship has been an invariant quantity over the last couple of years and I have greatly enjoyed (and continue to enjoy) his unique, honest, frequent, and reliable existence in my life. Robyn is a more recent addition, and despite being insane, I have truly appreciated her company.

Finally, I am most grateful to Breanne Byiers for everything. After a long, frustrating, rage-inducing day, only 30 seconds in her presence is needed to make me feel human again.

Dedication

To Breanne Byiers, my favorite human.

Abstract

An increasing number of non-terminal giant eruptions are being observed by modern supernova and transient surveys. Very little is known about the origin of these giant eruptions and their progenitors which are presumably very-massive, evolved stars such as luminous blue variables, hypergiants, and supergiants. Motivated by the small number of progenitors positively associated with these giant eruptions, we have begun a survey of the luminous and evolved massive star populations in several nearby galaxies. We aim to identify the likely progenitors of the giant eruptions, study the spatial variations in the stellar populations, and examine the relationship between massive star populations and their environment.

The work presented here is focused on stellar populations in the relatively nearby, giant, spiral galaxy M101 from sixteen archival BVI *HST*/ACS images. We create a catalog of stars in the direction to M101 with photometric errors $< 10\%$ for $V < 24.5$ and 50% completeness down to $V \sim 26.5$ even in regions of high stellar crowding. Using color and magnitude criteria we have identified candidate luminous OB type stars and blue supergiants, yellow supergiants, and red supergiants for future observation. We examine their spatial distributions across the face of M101 and find that the ratio of blue to red supergiants decreases by two orders of magnitude over the radial extent.

From our catalog, we derive the the star formation history (SFH) for the stellar populations in five $2'$ wide annuli by fitting the color-magnitude diagrams. Binning the SFH into time frames corresponding to populations traced by Hα, far ultraviolet (FUV), and near ultraviolet (NUV) emission, we show that the fraction of stellar populations young enough to contribute in Hα is $15\% - 35\%$ in the inner regions, compared to less than 5% in the outer regions. This provides a sufficient explanation for the lack of Hα emission at large radii.

We also model the blue to red supergiant ratio in our five annuli, examine the effects that a metallicity gradient and variable SFH have on the predicted ratios, and compare to the observed values. We find that the radial behavior of our modeled blue to red supergiant ratios is highly sensitive to both spatial variations in the SFH and metallicity. Incorporating the derived SFH into the modeled ratios, we are able to reproduce the

observed values at large radii (low metallicity), but at small radii (high metallicity) the modeled and observed ratios are discrepant.

Though photometry has proven to be a powerful tool to identify candidate evolved massive stars and their effects on their host galaxy, spectroscopy is necessary to study the physical properties of individual stars. We observed moderate-resolution optical spectra for 56 of the brightest stars in the direction to M101 using the Multiple Mirror Telescope. We also created light curves for each target using multi-epoch $UBVR$ images from the Large Binocular Telescope. We separate the spectroscopially confirmed members of M101 into four groups: hot supergiants, intermediate supergiants, emission-line stars, and LBVs. Several stars in each group are discussed in detail.

Of the spectroscopically confirmed members, we find that eight meet our criterion for variability. We present light curves for the known LBV candidates, V2, V4, and V9, and introduce a new candidate: 9492_14_11998. Additionally, we identify 20 new variables in M101. Lacking spectra, we separated the variables, by their photometric properties, into three groups: hot, intermediate, and cool. We find two hot stars with V-band variability of ± 1 magnitude; we flag these stars as LBV candidates. Of the intermediate and cool variables, we identify several stars with low- to moderate-amplitude variability ($0.1 - 0.5$ magnitudes).

Contents

List of Tables

List of Figures

Chapter 1

Introduction

1.1 The Evolution of the Most Massive Stars

Massive stars play a pivotal role in the evolution of galaxies. They inject energy into the interstellar medium (ISM) through their strong stellar winds and supernovae (SNe) explosions which influences the formation of new stars. The main sequence (MS) evolution of massive stars corresponds to the burning of H in the core. In low mass stars (M $<5\mathrm{M}_{\odot}$), this phase of stellar evolution is fairly quiescent; this is not the case for massive stars. Through strong stellar winds ($\dot{M}\sim 10^{-6}-10^{-7}$ $\mathrm{M}_{\odot}\mathrm{yr}^{-1}$) as much as half of the initial mass of the star may be lost during the core H-burning stage alone.

Beyond the MS phase of evolution, the evolution of massive stars is highly mass dependent. Of the most luminous hot stars (the blue supergiants), the maximum luminosity declines with decreasing temperature (Humphreys & Davidson, 1979). The yellow and red supergiants show a temperature-independent maximum luminosity at $\log(\mathrm{L}/\mathrm{L}_{\odot})\approx 5.8$ (Humphreys & Davidson, 1979) indicating that the most massive stars do not evolve to cooler temperatures. Humphreys & Davidson (1979, 1984) suggest that the most massive stars ($\mathrm{M}\gtrsim 60$ $\mathrm{M}_{\odot}$) do not evolve to red supergiants due to high mass loss, exemplified in giant eruption stars such as η Car and P Cygni, and the Luminous Blue Variables (LBV).

The classical or normal LBVs are observationally identified as luminous and hot stars that exhibit photometric and spectroscopic variability. In most cases, LBVs undergo "eruptions" which are characterized by photometric variability of $1-2$ magnitudes

and significantly enhanced mass loss rates (Humphreys & Davidson, 1994; Vink, 2012); variabiles of this nature have also been called S Dor variables after the prototype of this class, S Doradus, in the Large Magellanic Cloud. The increased mass loss rates result in an optically-thick wind with an apparent spectral type of A to F (T_{eff} ∼7000 K). As a result, the visual luminosity of the star increases, although the bolometric luminosity remains unchanged. The duration of which range between 10-40 years with the minima and maxima lasting several years.

Very rarely, LBVs display extreme outbursts similar to the giant eruption of η-Car and P-Cygni. These objects have been called giant eruptions LBVs (Humphreys & Davidson, 1994), the η Car variables (Humphreys et al., 1999), and η Car analogs (Van Dyk, 2005). These giant eruptions have luminosities that approach the lower limit for true supernovae ($M_V \approx -14$) and have spectroscopic features similar to Type IIn supernovae from the strong interaction between the ejecta and the circumstellar medium from prior mass loss episodes (Turatto et al., 1993). As a result, giant eruptions are often mis-classified as supernovae. However, the temporal evolution of their photometric and spectroscopic properties reveal that they are sub-luminous and their spectra do not evolve into true supernovae: hence the terminology "supernova impostors" (Van Dyk & Matheson (2012) and references therein).

Recently, supernova surveys have lead to the identification of an increasing number of these non-terminal optical transients with a wide range of properties. Some appear to be similar to the giant eruptions characteristic of η Car variables, while others are more akin to the variability of normal LBVs. A very small fraction of the optical transients originate from lower luminosity, heavily-obscured progenitors that may be extreme asymptotic giant branch (AGB) stars or in a post red supergiant stage of evolution (Thompson et al., 2009; Khan et al., 2010; Bond, 2011). The physical mechanism that triggers these giant eruptions is not known and very little is known about the progenitors. The observed diversity in the properties of the transients raises questions regarding the connection between the giant eruptions and the normal LBV outbursts. They may come from a range of initial masses and different evolutionary states.

The continued monitoring of these optical transients has led to the realization that in some cases the apparent supernova explosion is preceded by smaller eruptions, e.g. SN2005gl (Gal-Yam et al., 2007; Gal-Yam & Leonard, 2009), SN2006jc (Pastorello et al.,

2007) and most recently the peculiar SN2009ip (Mauerhan et al., 2013; Pastorello et al., 2013; Fraser et al., 2013; Margutti et al., 2013). Consequently, the connection between the giant eruptions and true supernovae has come into question. Due to the extreme rarity of the giant eruption LBVs, very little is known about their progenitors and evolutionary state. To shed light on the nature of these rare stars and evolutionary states, an improved census of the most massive, evolved stars is necessary. Since the number of known LBVs and hypergiants is very small, our understanding of the late stages of stellar evolution is greatly hindered by small number statistics. To improve our statistics, the work presented here is part of a larger survey of the evolved massive star populations in several nearby galaxies (Humphreys et al., 2013; Grammer & Humphreys, 2013; Humphreys et al., 2014).

1.2 The Relationship Between Massive Star Populations and their Environment

Early observations of the massive star content in M33 demonstrated that the B/R ratio decreases with distance from the center (Walker, 1964). Later, it was suggested by van den Bergh (1968) that this trend could be due to the radial metallicity gradient. Subsequent studies of the radial variation in the massive star content in the Galaxy (Humphreys, 1979; Humphreys & McElroy, 1984; Eggenberger et al., 2002), M33 (Humphreys, 1980), and M101 (Grammer & Humphreys, 2013) have found similarly decreasing trends in the B/R ratio with radius both in the field-star populations, and stellar associations and clusters. Assuming that in spiral galaxies metallicity declines with radius, there is a positive correlation between the B/R ratio and metallicity.

One explanation for the metallicity dependence of the B/R ratio is that the length of time that a star spends as a He-burning red supergiant decreases with metallicity. Stellar winds, in hot stars, are powered by the transfer of momentum from photons to metallic ions through atomic spectral lines, also known as line driven winds (Castor et al., 1975). Since line driven winds are powered by the absorption of metallic ions, the strength of a wind, and thus the mass loss rate, is necessarily metallicity dependent. Mass loss via line driven winds was first used to explain the broad emission lines of nuclear-processed material in the spectra of Wolf-Rayet (WR) stars (Conti, 1978). Since then, it has been

suggested that the length of time that a star spends as a He-burning red supergiant should decrease with metallicity (Maeder et al., 1980). Enhanced mass loss during MS results in the star either foregoing the red supergiant stage altogether and undergoing He burning as a WR star, or spending significantly less time as a red supergiant and evolving rapidly to a WR star. Thus the minimum mass for a star to become a WR star decreases with metallicity. Massey & Johnson (1998) provide support for this scenario by examining the WR and red supergiant populations in NGC 6822, M33, and M31 showing that the ratio of WR to red supergiants is particularly sensitive to metallicity; they find a decrease in the ratio of WR to red supergiants by roughly 100 over a 0.9 dex change in metallicity.

While the observational support for a metallicity dependence is strong, it is well known that the B/R ratio is highly luminosity dependent (Stothers & Chin, 1969; Langer & Maeder, 1995) and therefore has a strong mass and age dependence. To properly calculate the B/R, one must be certain that the mass distributions of the red and blue supergiants are identical. Consequently, to compare the B/R ratio between galaxies, or even different regions in the same galaxy, the star formation histories (SFH) must be identical or the age dependence removed. Shown by Dohm-Palmer & Skillman (2002), the shape of the observed age dependence is adequately reproduced using non-rotating stellar evolution models. However, the ratios themselves are discrepant by a factor of two; they attribute the discrepancy to stellar rotation. Often, the B/R ratio is used as a model diagnostic (Langer & Maeder, 1995, and references therein), however to be useful as a model diagnostic, it is important to know which parameters – metallicity, SFH, stellar rotation – it is most sensitive to.

Given the effects of metallicity and age on the distribution of stars in color-magnitude space, host-galaxy abundance gradients and SFH necessarily manifest spatial variations in the resolved stellar populations. Broad- and narrow-band imaging, from IR to X-Ray, indicates that similar to the stellar populations, the emission properties of galaxies vary spatially. Recently, deep observations of galaxies using *Galaxy Evolution Explorer (GALEX)* have demonstrated ultraviolet (UV) emission is considerably more extended than optical emission, a property described as an extended UV disk (XUV; Thilker et al., 2005, 2007). Moreover, the UV disk is roughly twice that of Hα (Boissier et al., 2007; Goddard et al., 2010) suggesting that in the outskirts of XUV galaxies, O stars

are rare but B- and A-type stars are abundant.

A truncated initial mass function (IMF) in low-density, star-forming regions or statistical sampling of the IMF could suppress the formation of massive O stars, thereby leading to the absence of Hα at large radii (Boissier et al., 2007; Meurer et al., 2009; Goddard et al., 2010; Lee et al., 2011; Koda et al., 2012). Or alternatively, the star forming-regions are, on average, older in the outskirts (Thilker et al., 2005; Zaritsky & Christlein, 2007). Comparing the stellar populations in complexes observed in both UV and Hα to complexes seen only in UV, suggests the lack of Hα may be attributed to differences in stellar population age (Thilker et al., 2005; Gogarten et al., 2009; Alberts et al., 2011). Although the two explanations are generally difficult to disentangle due to the age-IMF degeneracy.

1.3 The Structure of this Thesis

As part of a survey on the massive star populations in several nearby galaxies, the focus of this thesis is on the stellar populations in the nearby, face-on, giant-spiral galaxy M101. Our main goals are to assemble a catalog of luminous, evolved stars for future studies, study the relationship between stellar populations and metallicity, and SFH, and to identify the likely progenitors to the giant eruptions based on spectra and multi-epoch imaging. The chapters are in chronological order. In chapter 2, we present the identification and spatial distribution of the visually luminous stars in M101 (Grammer & Humphreys, 2013). The spatial variations in the recent SFH are discussed in chapter 3 (Grammer & Humphreys, 2014). The photometric variability and spectroscopy for the most luminous stars in M101 are discussed in chapter 4, the results of which will be published in Grammer et al. (2014). Finally, chapter 5 summarizes the results of the previous chapters.

Chapter 2

The Identification and Spatial Distribution of the Visually Luminous Stars (Grammer & Humphreys, 2013)

Abstract

An increasing number of non-terminal giant eruptions are being observed by modern supernova and transient surveys. But very little is known about the origin of these giant eruptions and their progenitors, many of which are presumably very massive, evolved stars. Motivated by the small number of progenitors positively associated with these giant eruptions, we have begun a survey of the evolved massive star populations in nearby galaxies. The nearby, nearly face on, giant spiral M101 is an excellent laboratory for studying a large population of very massive stars. In this paper, we present BVI photometry obtained from archival *HST*/ACS WFC images of M101. We have produced a catalog of luminous stars with photometric errors $< 10\%$ for $V < 24.5$ and 50% completeness down to $V \sim 26.5$ even in regions of high stellar crowding. Using color and luminosity criteria we have identified candidate luminous OB type stars and blue supergiants, yellow supergiants,

and red supergiants for future observation. We examine their spatial distributions across the face of M101 and find that the ratio of blue to red supergiants decreases by two orders of magnitude over the radial extent of M101 corresponding to 0.5 dex in metallicity. We discuss the resolved stellar content in the giant star forming complexes NGC 5458, 5453, 5461, 5451, 5462, and 5449 and discuss their color-magnitude diagrams in conjunction with the spatial distribution of the stars to determine their spatio-temporal formation histories.

2.1 Introduction

Most massive stars will ultimately end their lives as core collapse supernovae however there are several famous examples where massive stars have experienced spectacular non-terminal giant eruptions that rival true supernovae. The modern supernova surveys have produced an increasing number of these non-terminal optical transients with a wide range of properties. Many of these objects are initially mis-classified as supernovae due to peak luminosities approaching the lower limit for core-collapse supernovae. Their spectral features are also similar to the Type IIn supernovae arising from the strong interaction between the ejecta and the circumstellar medium from prior mass loss episodes (Turatto et al., 1993). Subsequent observations reveal that these objects are sub-luminous and that their temporal spectral and photometric evolution is not typical of true supernovae. Consequently, these events are sometimes called "SN impostors" (Van Dyk & Matheson (2012) and references therein). In some cases the apparent terminal eruption is preceded by smaller eruptions e.g. SN2005gl (Gal-Yam et al., 2007; Gal-Yam & Leonard, 2009), SN2006jc (Pastorello et al., 2007) and most recently the peculiar SN2009ip (Mauerhan et al., 2013; Pastorello et al., 2013; Fraser et al., 2013; Margutti et al., 2013). This of course raises questions about the origin of these giant eruptions and their possible relation to true supernovae. The physical mechanism that triggers these giant eruptions is not known and very little is known about the progenitors. They may come from a range of initial masses and different evolutionary states. An improved census of the likely progenitor classes is now needed; i.e. the evolved most massive stars, the Luminous Blue Variables (LBVs), and the hypergiant stars. The

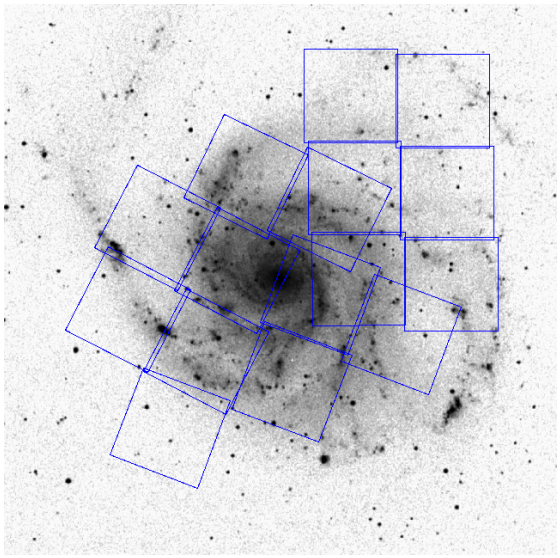

Figure 2.1: POSS-II red image of M101 from the Digitized Sky Survey. The *HST*-ACS fields are shown overlayed onto the image.

work presented here is part of a larger survey of the evolved massive star populations in nearby galaxies (Humphreys et al., 2013). [hbt!]

The nearby, face-on, giant spiral M101 provides an ideal laboratory for the study of luminous massive stars. Beginning with the early work of Sandage & Tammann (1974) on the brightest blue stars, the vast population of luminous massive stars in M101 has been a subject of interest for the last 40 years (Humphreys, 1980; Sandage, 1983; Humphreys & Strom, 1983; Humphreys et al., 1986; Humphreys & Aaronson, 1987). With the launch of *The Hubble Space Telescope* in 1990, the study of the resolved stellar content of M101 became possible and since then many studies have examined and characterized the immense population of Cepheid variables (Shappee & Stanek (2011) and references therein), stellar clusters (Bresolin et al., 1996; Chen et al., 2005; Barmby et al., 2006), H II regions (Rosa & Benvenuti, 1994; Pleuss et al., 2000; García-Benito et al., 2011; Sun et al., 2012), and supernova remnants (Lai et al., 2001; Franchetti et al., 2012). The next logical step is the identification of its large population of luminous stars including OB type stars, blue supergiants, yellow supergiants, and red supergiants. In a similar survey, Shara et al. (2013) are using narrowband imaging of M101 to identify

Table 2.1. HST/ACS Observations

Field Name	α_{J2000}	δ_{J2000}	Filters	t_{exp}(s)	$m_{50\%}$
9490_01	14:03:22.61	+54:21:27.98	F435W, F555W, F814W	2×450, 2×360, 2×360	26.8, 26.2, 26.0
9490_02	14:03:02.15	+54:20:36.80	F435W, F555W, F814W	2×450, 2×360, 2×360	26.9, 26.3, 25.9
9490_03	14:03:20.05	+54:24:51.49	F435W, F555W, F814W	2×450, 2×360, 2×360	27.0, 26.3, 26.0
9490_a1	14:03:30.06	+54:18:31.08	F435W, F555W, F814W	2×450, 2×360, 2×360	27.0, 26.4, 26.1
9490_a2	14:03:09.05	+54:17:28.24	F435W, F555W, F814W	2×450, 2×360, 2×360	27.0, 26.4, 26.1
9490_a3	14:02:59.92	+54:23:43.48	F435W, F555W, F814W	2×450, 2×360, 2×360	26.9, 26.3, 26.1
9490_b1	14:03:49.57	+54:20:00.69	F435W, F555W, F814W	2×450, 2×360, 2×360	27.2, 26.6, 26.3
9490_b2	14:03:38.87	+54:15:45.84	F435W, F555W, F814W	2×450, 2×360, 2×360	27.1, 26.4, 26.1
9490_c1	14:03:42.32	+54:22:59.34	F435W, F555W, F814W	2×450, 2×360, 2×360	27.0, 26.4, 26.2
9490_c2	14:02:41.90	+54:19:13.46	F435W, F555W, F814W	2×450, 2×360, 2×360	26.8, 26.3, 26.2
9492_09	14:02:53.70	+54:27:35.70	F435W, F555W, F814W	3×360, 3×360, 3×360	27.4, 26.8, 26.7
9492_10	14:02:52.53	+54:24:17.80	F435W, F555W, F814W	3×360, 3×360, 3×360	27.3, 26.6, 26.5
9492_11	14:02:51.42	+54:20:59.90	F435W, F555W, F814W	3×360, 3×360, 3×360	27.3, 26.6, 26.4
9492_12	14:02:30.78	+54:27:25.88	F435W, F555W, F814W	3×360, 3×360, 3×360	27.4, 26.8, 26.6
9492_13	14:02:29.60	+54:24:07.97	F435W, F555W, F814W	3×360, 3×360, 3×360	27.3, 26.6, 26.4
9492_14	14:02:28.42	+54:20:50.06	F435W, F555W, F814W	3×360, 3×360, 3×360	27.3, 26.8, 26.5

emission line stars such as the Wolf-Rayet (WR) stars.

In this first paper we discuss the creation of a catalog of candidate luminous stars. In the next section, we describe the observations, data reduction, and photometry. In §3 we discuss the identification of luminous stars of different types. We explore their spatial distributions and how their relative numbers vary with radius in §4. In §5, we examine the massive star content within the giant star forming complexes NGC 5458, 5453, 5461, 5451, 5462, and 5449. We summarize our conclusions in the last section. Subsequent papers will be dedicated to the discussion of the massive star formation history in M101 (Paper II), the variability and evidence for instabilities in several of our massive stars (Paper III), and the spectroscopy of several of the most luminous and variable stars in M101 (Paper IV).

2.2 Observations and Photometry

Sixteen fields in M101 were imaged with *The Hubble Space Telescope (HST)* Advanced Camera for Surveys (ACS) Wide Field Camera (Figure 2.1) November 13-16 2002 and January 14-23 2003 (proposal IDs 9490 and 9492). In Table 2.1, we list the field centers, observation dates, filters, exposure times, and 50% completeness magnitudes from the artificial star tests (discussed below). Each exposure was bias subtracted and flat-fielded by the STScI On-the-Fly-Reprocessing system.

We used DOLPHOT, a modified version of HSTphot (Dolphin, 2000), with the ACS

module to measure the photometry. DOLPHOT performs the photometry by fitting the ACS point-spread-function (PSF), calculated with TinyTim[1], to all sources in each individual frame. The PSF magnitudes are aperture corrected using the most isolated stars in each frame and the results from individual exposures are combined. Count rates are then converted to magnitudes on the VEGAMAG system. The *HST*/ACS instrumental magnitudes were transformed to the Landolt *BVI* magnitudes using the equations from Sirianni et al. (2005). We corrected the photometry for foreground extinction using $E(B-V) = 0.01$ (Schlegel et al., 1998) and the Galactic extinction curve from Cardelli et al. (1989).

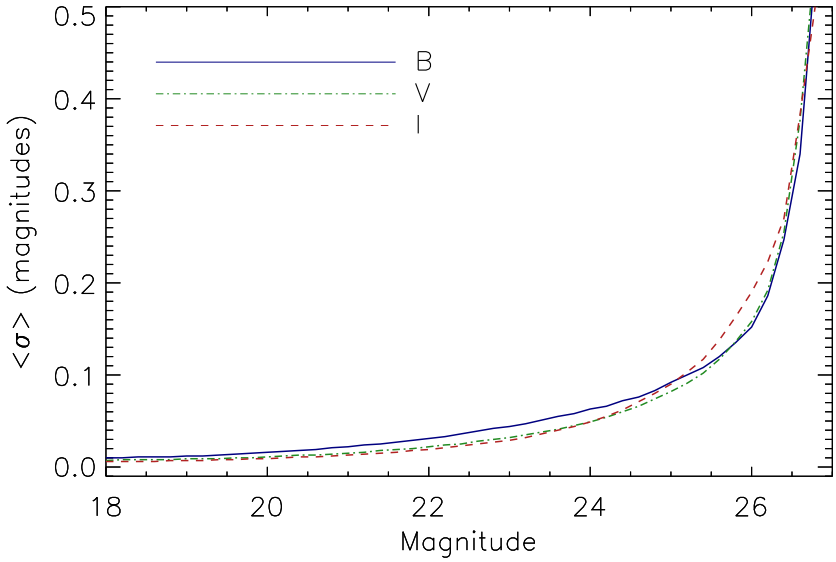

Figure 2.2: Mean photometric errors as a function of magnitude. Errors are the quadrature sum of the Poisson errors and the photometric error functions derived from the artificial star tests.

[ht!]

To transform the raw output of DOLPHOT to a catalog of stellar sources, we used the following parameters: object classification, error flag, signal-to-noise (S/N), sharpness, and crowding. Sources with non-stellar radial profiles, error flags indicating seriously compromised photometry, and/or S/N < 4 were immediately removed. We

[1] http://www.stsci.edu/software/tinytim/

Table 2.2. M101 Catalog

ID	Field	α_{J2000}	δ_{J2000}	V	σ_V	$B-V$	σ_{B-V}	$V-I$	σ_{V-I}
J140328.24+541658.12	9490_a1	14:03:28.24	54:16:58.12	18.430	0.002	0.177	0.002	0.123	0.003
J140331.33+542114.40	9490_01	14:03:31.33	54:21:14.40	18.490	0.002	-0.060	0.002	-0.067	0.003
J140341.49+541904.98	9490_b1	14:03:41.49	54:19:04.98	18.552	0.002	0.188	0.003	0.371	0.003
J140236.66+542145.47	9492_14	14:02:36.66	54:21:45.47	18.578	0.002	0.145	0.003	0.684	0.003
J140248.72+541756.47	9490_c2	14:02:48.72	54:17:56.47	18.615	0.002	0.306	0.003	0.435	0.003
J140334.05+541836.94	9490_a1	14:03:34.05	54:18:36.94	18.633	0.002	0.082	0.003	-0.235	0.003
J140312.49+542053.74	9490_02	14:03:12.49	54:20:53.74	18.641	0.002	0.158	0.003	0.215	0.003
J140255.00+542226.94	9492_11	14:02:55.00	54:22:26.94	18.670	0.002	-0.015	0.002	-0.056	0.003
J140221.40+542541.02	9492_13	14:02:21.40	54:25:41.02	18.902	0.002	1.080	0.004	1.239	0.003
J140301.20+541839.71	9490_a2	14:03:01.20	54:18:39.71	18.961	0.002	0.312	0.003	0.487	0.003

required that the radial profiles be well fit by the ACS PSF using the sharpness parameter and that the photometry not be dramatically affected by neighboring sources using the crowding parameter. Sharpness is defined to be zero for a perfectly fit PSF, negative for an extended source, and positive for a narrower source (e.g cosmic rays). Crowding quantifies the degree by which neighboring stars have affected the photometry of an individual star by calculating the difference, in magnitudes, before and after PSF subtraction; large values of the crowding parameter suggest that the photometry may be unreliable. We experimented with the sharpness and crowding parameters by imposing a range of acceptable values, after which we visually inspected the color-magnitude diagrams (CMD) produced from the accepted and rejected objects. The final values of sharpness and crowding were adopted when the CMD of rejected objects no longer contained any discernible features, such as a main-sequence or red supergiant branch, and visual inspection of the *HST*/ACS images showed that the accepted objects were not associated with artifacts, diffraction spikes, or background galaxies. The precise sharpness and crowding criteria that we used to create the final catalog of stellar sources are $|B_{sharp} + V_{sharp} + I_{sharp}| < 0.6$ and $(B_{crowd} + V_{crowd} + I_{crowd}) < 1.5$ magnitudes.

The photometric errors and completeness functions were calculated using artificial stars tests. We estimated the photometric error functions for each field by injecting 500,000 artificial stars into each frame and then calculated the difference between the input and output magnitudes as a function of input magnitude. The root-mean-square widths of the error functions were determined at intervals of 0.2 magnitudes and added in quadrature to the Poisson errors generated by DOLPHOT. Figure 2.2 shows the mean error as a function of magnitude for the full catalog. We find that the photometric

errors are less than 10% for $B < 24.5$, $V < 24.3$, and $I < 24.0$. The completeness of our catalog as a function of magnitude, color, and position was determined by subjecting the artificial star photometry to the same quality criteria as described above. Color and position averaged completeness functions were generated for each field and the 50% completeness magnitudes are given in the final column of Table 2.1. The catalog is complete at the 50% level at $B = 27$, $V = 26.5$, and $I = 26.2$ for the fields from proposal ID 9490, and $B = 27.3$, $V = 26.8$, and $I = 26.4$ for fields from proposal ID 9492, which had longer integration times.

Very massive stars are found in OB associations and clusters where stellar crowding will be problematic, we therefore examined the photometric errors and completeness in regions of high stellar density. For example, field 9490_01 contains the center of M101 where crowding is high and photometric precision is bound to suffer. By isolating stars located in the visually most crowded regions of field 9490_01, we find that the photometric errors are better than 10% down to $B = 24.1$, $V = 23.8$, and $I = 23.6$ and the 50% completeness magnitudes are $B = 26.5$, $V = 26.2$, and $I = 25.9$. Therefore even in the most crowded regions of the galaxy, the photometry is still reliable.

WCS positions were converted to the SDSS DR8 FK5 J2000 reference frame by cross-correlating the ACS positions of stars also detected by the SDSS. An astrometric solution was performed for each frame with errors in the solutions on the order of $0''.15$. To remove duplicate entries in the overlapping ACS fields we determined the area of overlap between the two fields and removed stars in the overlapping region from the field with the shorter integration time. We iteratively applied this process to all field pairs to create the final catalogs for each field. The individual fields were combined to create the final photometric catalog which contains 539,825 stars in the magnitude range $18.4 < V < 27.6$ and are sorted by increasing V magnitude.

The full version of our catalog is available online but a sample of the catalog is shown in Table 2.2 which contains the first ten entries. The following columns are included: identification, ACS field number, right ascension, declination, V, σ_V, $(B-V)$, σ_{B-V}, $(V-I)$, and σ_{V-I}. The identifications are based on their $J2000$ coordinates such that J140331.33+542114.40 refers to a star located at $\alpha_{J2000.00}$ = 14:03:31.33 and $\delta_{J2000.00}$ = +54:21:14.40. The 50% completeness magnitude of $V \approx 26.5$ corresponds to an absolute magnitude of $M_V \approx -2.5$ at our adopted distance modulus to M101,

$\mu_0 = 29.05 \pm 0.06(random) \pm 0.12(systematic)$, from Shappee & Stanek (2011). In Figure 2.3 we show the CMDs containing all catalog entries.

2.3 Identifying the Massive Star Candidates

To select the different subsets of luminous stars from this very large and comprehensive catalog, we created a subcatalog of stars in the magnitude range $18.5 \leq V \leq 24.2$ where the bright end includes the visually brightest stars in our catalog. At the distance to M101, the faint limit corresponds to $M_V \approx -4.9$, which will include the luminous, hot

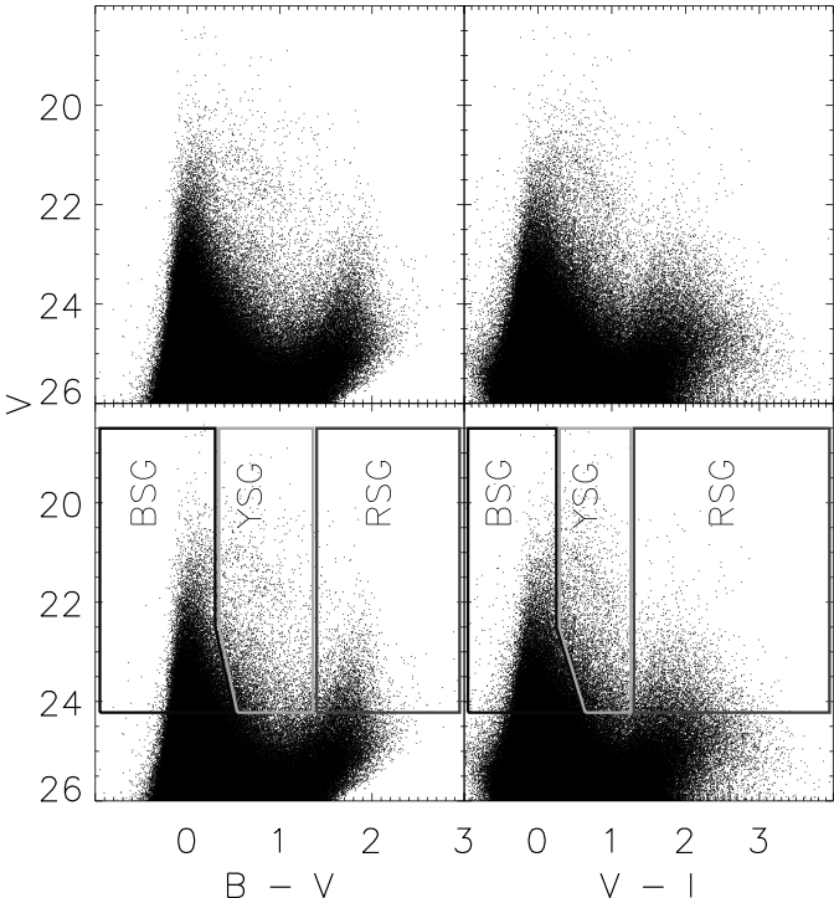

Figure 2.3: *Top*: Color-magnitude diagrams of M101. *Bottom*: Color-magnitude diagrams showing the selection criteria for luminous massive stars in the BSG, YSG, and RSG subsets (see §3 for details).

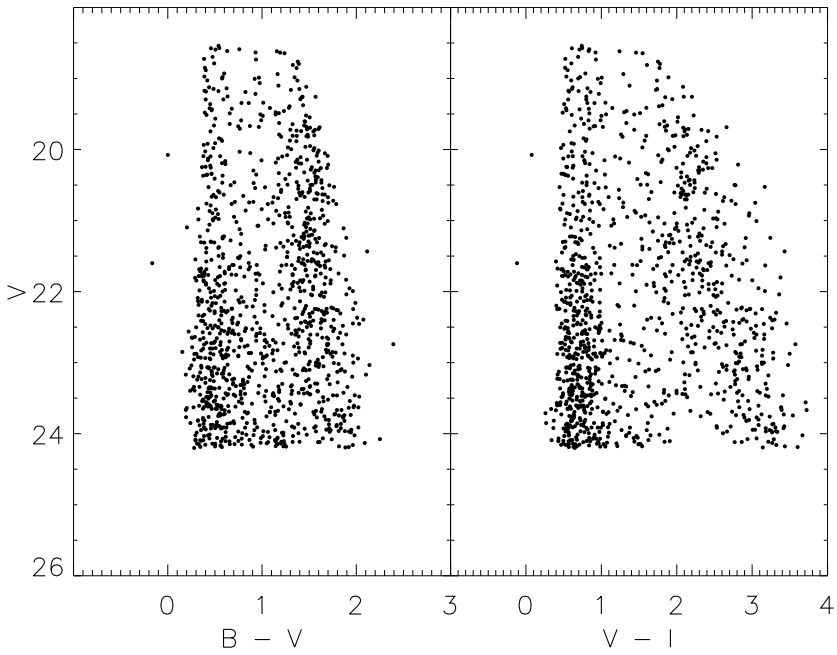

Figure 2.4: Color-magnitude diagrams of the anticipated Galactic foreground contaminants resulting from the Besançon Galactic population synthesis model (Robin et al., 2003) in the direction of M101.

OB type stars and the most luminous stars at all temperatures. Fainter than $V = 24.2$ the photometric errors are larger than 10% and are no longer reliable. This subcatalog includes 35,705 stars. The CMD in Figure 2.3 shows two well-populated branches which we identify respectively with the blue supergiants and luminous OB type stars, hereafter referred to BSGs, and the red supergiants (RSG) which are located at $(B-V) \geq 1.4$ and $(V-I) \geq 1.3$. The locus of the BSG group is identified in our CMDs as $(B-V) \leq 0.3$ and $(V-I) \leq 0.25$ for $V < 22.5$. Fainter than $V = 22.5$, the BSG locus systematically broadens to redder $(B-V)$ and $(V-I)$ colors which may be due to a broadened main-sequence at lower initial masses, interstellar reddening, or to some RSGs evolving back to warmer temperatures. We therefore adopt somewhat redder $(B-V)$ and $(V-I)$ cutoffs for the magnitude range $22.5 < V \leq 24.2$. Furthermore we identify the intermediate color, or yellow supergiants (YSGs), as stars with colors in the CMD between the BSG and RSG populations. Our color and magnitude criteria for the BSG, YSG, and RSG populations are summarized in Table 2.3 and are shown superimposed on the CMDs in

Table 2.3. Massive Star Candidate Selection Criteria

Group	Color Criteria	Magnitude Criteria
BSG	$(B-V) \leq 0.3$, $(V-I) \leq 0.25$	$18.5 \leq V \leq 22.5$
	$(B-V) \leq 0.5$, $(V-I) \leq 0.6$	$22.5 \leq V \leq 24.2$
YSG	$0.3 < (B-V) < 1.4$	$18.5 \leq V \leq 22.5$
	$0.25 < (V-I) < 1.3$	
	$0.5 < (B-V) < 1.4$	$22.5 \leq V \leq 24.2$
	$0.6 < (V-I) < 1.3$	
RSG	$(B-V) \geq 1.4$, $(V-I) \geq 1.3$	$18.5 \leq V \leq 22.5$

the bottom half of Figure 2.3.

The use of broad band photometry to identify luminous massive star candidates from our subcatalog increases the likelihood that contaminating sources may be included. Foreground contamination is commonly estimated by observing a field that is offset from the galaxy, however no such archival field in the same filter set was available for M101. Consequently we have modeled the Galactic line-of-sight contributions using the Besançon Galactic population synthesis model (Robin et al., 2003) over the area covered by the ACS fields. We used our photometric error functions (Figure 2.2) in the model to obtain the most realistic CMDs of likely foreground stars stars shown in Figure 2.4. As expected, the F through M dwarfs and red giant branch stars make up the largest foreground contribution with colors that are consistent with our defined YSG and RSG groups. Massey (1998) showed that RSGs can be photometrically separated from dwarfs in a color-color diagram due to lower surface gravity resulting in redder $(B-V)$ colors for a given $(V-I)$. We take a similar approach and use a color-color diagram to differentiate probable massive stars from other sources of contamination. In Figure 2.5 we show the $(B-V)$ versus $(V-I)$ diagram for our subcatalog and model stars with $V \leq 24.2$. In addition we show the theoretical luminosity class I sequence, hereafter the supergiant sequence, from Bertelli et al. (1994) as a solid line. While there is some scatter in Figure 2.5, stars from the subcatalog form a clear sequence that closely follows the supergiant sequence. Stars from the Besançon model also form a sequence, hereafter called the Besançon sequence, that deviates from the supergiant sequence redward of $(V-I) \approx 1$. Assuming that the Besançon model is an accurate representation of the foreground component, we find that the RSGs are separable from foreground stars on a $(B-V)$ versus $(V-I)$ diagram whereas the YSGs are not.

Asymptotic Giant Branch (AGB) stars are known to overlap in color and luminosity with the RSGs (Brunish et al., 1986). However our imposed magnitude limit of $V \leq 24.2$, corresponding to $M_V \lesssim -4.9$, is more luminous than the theoretical visual upper luminosity limit for AGB stars at Z = 0.004 (Bertelli et al., 1994). At higher metallicities the AGB visual upper luminosity limit is fainter thereby reducing the likelihood that AGB stars populate our RSG sample.

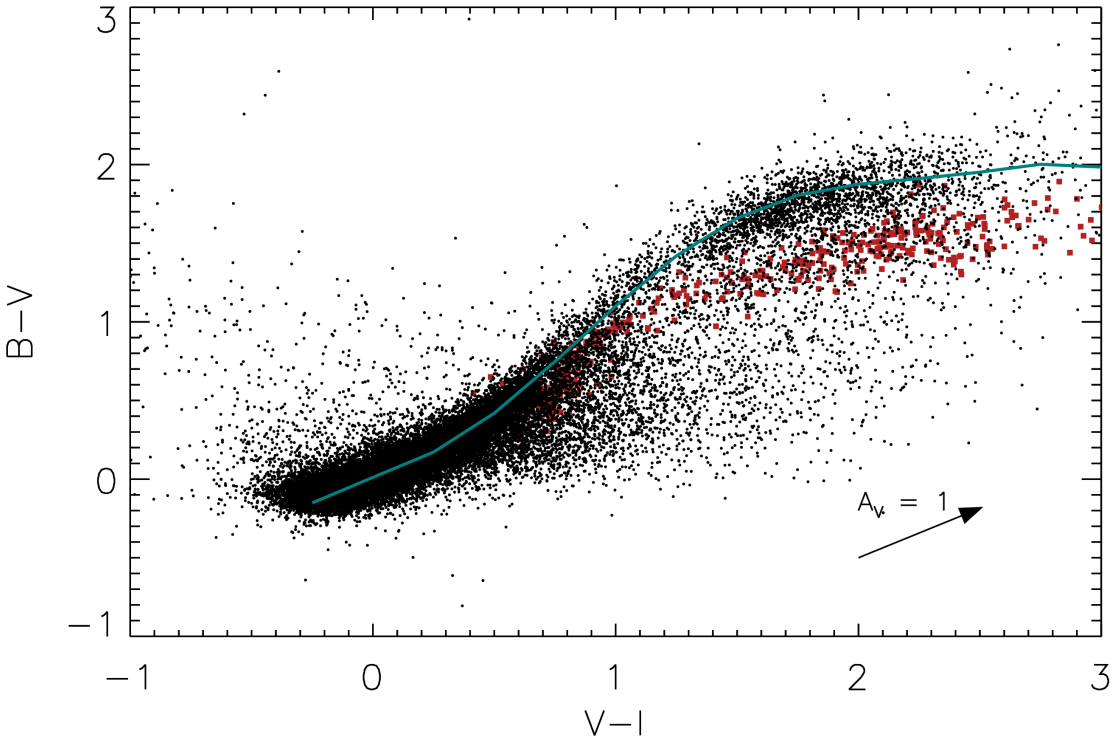

Figure 2.5: Color-color diagram of stars with $V \leq 24.2$ magnitudes. We show the theoretical supergiant sequence from (Bertelli et al., 1994) superimposed as a solid line. Stars from the Besançon Galactic population synthesis model with $V \leq 24.2$ are shown as red squares. Additionally we show the reddening resulting from $A_V = 1$ assuming a Galactic extinction law (Cardelli et al., 1989)

The presence of stars below the Besançon sequence in Figure 2.5 and those with very blue $(V-I)$ and red $(B-V)$ colors have photometric properties that cannot be explained by foreground contamination and are likely a mixture of blended objects, unresolved clusters, and reddened stars. Barmby et al. (2006) found that clusters would appear to be "slightly resolved" at the distance of M101. While we have removed sources

with radial profiles that deviate appreciably from the ACS PSF using the sharpness parameter, very small clusters may be included in our catalog. Based on the size distribution and luminosity function of the Barmby et al. (2006) cluster candidates, we expect around 500 may be included in our subcatalog. Barmby et al. (2006) show that the cluster candidates span the range $0 < (V - I) < 1.75$ and $0 < (B - V) < 1$. Cluster candidates in M51 (Bik et al., 2003) and M81 (Chandar et al., 2001) are similarly distributed in size, luminosity, and color-color space, thus we find it likely that a large fraction of the stars with anomalous colors may be unresolved clusters. There are ~ 1500 stars with anomalous colors, roughly a factor of three greater than than the expected number unresolved clusters. A fraction of the remaining stars with anomalous colors may be accounted for by blended objects, particularly those with very red $(B - V)$ colors and very blue $(V - I)$ colors and vice versa.

To account for the remaining stars with anomalous colors, we show a fiducial $A_V = 1$ reddening vector in Figure 2.5 which corresponds to $E(B-V) = 0.32$ and $E(V-I) = 0.54$ (Cardelli et al., 1989). Stars with the intrinsic colors of $(B - V)_0 < 0.5$ and $(V - I)_0 < 0.6$, reddened by $0.5 - 1$ magnitudes, would migrate to the region of the color-color diagram which contains the highest density of anomalously colored stars. Consequently it is likely that the remaining stars with anomalous colors are moderately reddened blue stars. Making the assumption that all the stars that do not follow the supergiant sequence (Figure 2.5) are a mix of unresolved clusters, blended objects, reddened blue stars, and foreground stars, then we may remove a large fraction of the contaminating sources, at the expense of reducing the completeness of the BSG group, by requiring that candidate luminous massive stars follow the supergiant sequence to within a given tolerance. The observed width of the subcatalog sequence is $\sim$0.5 magnitudes, thus we further constrain our selection criteria by requiring that colors be consistent with the supergiant sequence to within ± 0.25 magnitudes.

We have taken measures to reduce the amount of foreground contamination to our sample of luminous massive star candidates through the use of a color-color diagram, however as mentioned above, the BSGs and YSGs are not well separated from foreground stars. Therefore we have characterized the degree by which foreground stars likely contribute to each group by subjecting the Besançon model stars to our selection criteria and comparing the relative number of stars in each group. We have identified 25,603

BSGs, 3,105 YSGs, and 2,294 RSGs and based on the Besançon model, we expect the remaining foreground contribution in the BSGs, YSGs, and RSGs to be $\sim$ 0%, $\sim$ 20%, and $\sim$ 5% respectively. Considering the brightest stars in each group ($V < 22$), foreground contamination remains very low in the BSGs ($\ll$ 1%) but increases dramatically in the YSGs and RSGs. Approximately 40% of the bright YSGs are likely foreground stars due to degenerate photometric properties in intermediate color dwarfs and supergiants.

Based on the model, the brightest RSGs are expected to suffer from a large amount of contamination ($50 - 100\%$) attributed to the overlap between the subcatalog and the Besançon stars with $(V - I) > 2$. However of the 22 brightest RSGs, only 2 have $(V - I) > 2$ therefore the contaminating fraction is likely to be considerably lower for the majority. We illustrate this point by noting that there are 20 bright RSGs with $(V - I) < 2$ whereas there are 3 stars from the Besançon model that have similar photometry. Consequently the brightest RSGs have a contaminating fraction that is more likely to be $\sim$ 15%. In summary, we find that using our selection criteria 100% of the 25,603 BSGs, $60 - 80\%$ of the 3,105 YSGs, and $85 - 95\%$ of the 2,294 RSGs are members of M101.

2.4 Radial Stellar Population Variations

A massive, face on, spiral galaxy such as M101 provides an opportunity to examine variations in the stellar content with changes in environment. M101 is known to have a steep abundance gradient and many regions of intense star formation interspersed throughout that may manifest various effects in the spatial distributions of luminous stars and their CMDs. First we examine the spatial distributions of the luminous stars in the BSG, YSG, and RSG groups, shown in Figure 2.6, which have been separated into three magnitude bins: $V < 22$, $22 \leq V < 23$, and $V \geq 23$. In the top panel of Figure 2.6, the brightest BSGs are distributed across the entire face of M101 but show large density enhancements in the spiral arms and massive OB associations. Though less clumpy and fewer in number, the brightest YSGs appear to have a spatial distribution similar to BSGs. The brightest RSGs are significantly more scarce and a large fraction may be foreground stars. In the two fainter bins, the distributions of the luminous massive star

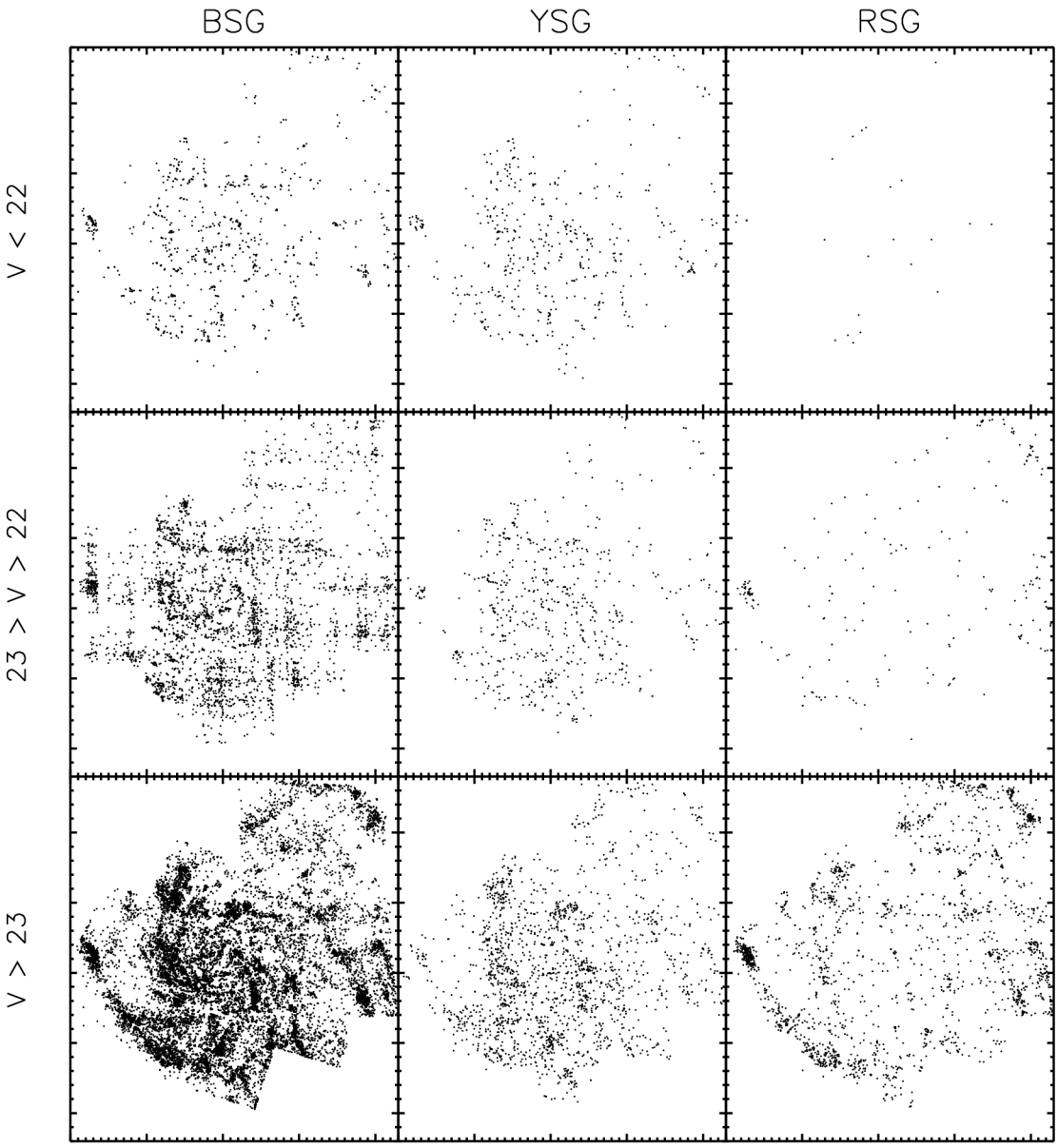

Figure 2.6: Spatial distributions of the luminous massive star candidates with North up and East to the left. The columns show the candidates separated into the BSG, YSG, and RSG subsets (see §3 for details) and the rows show the dependence on magnitude interval.

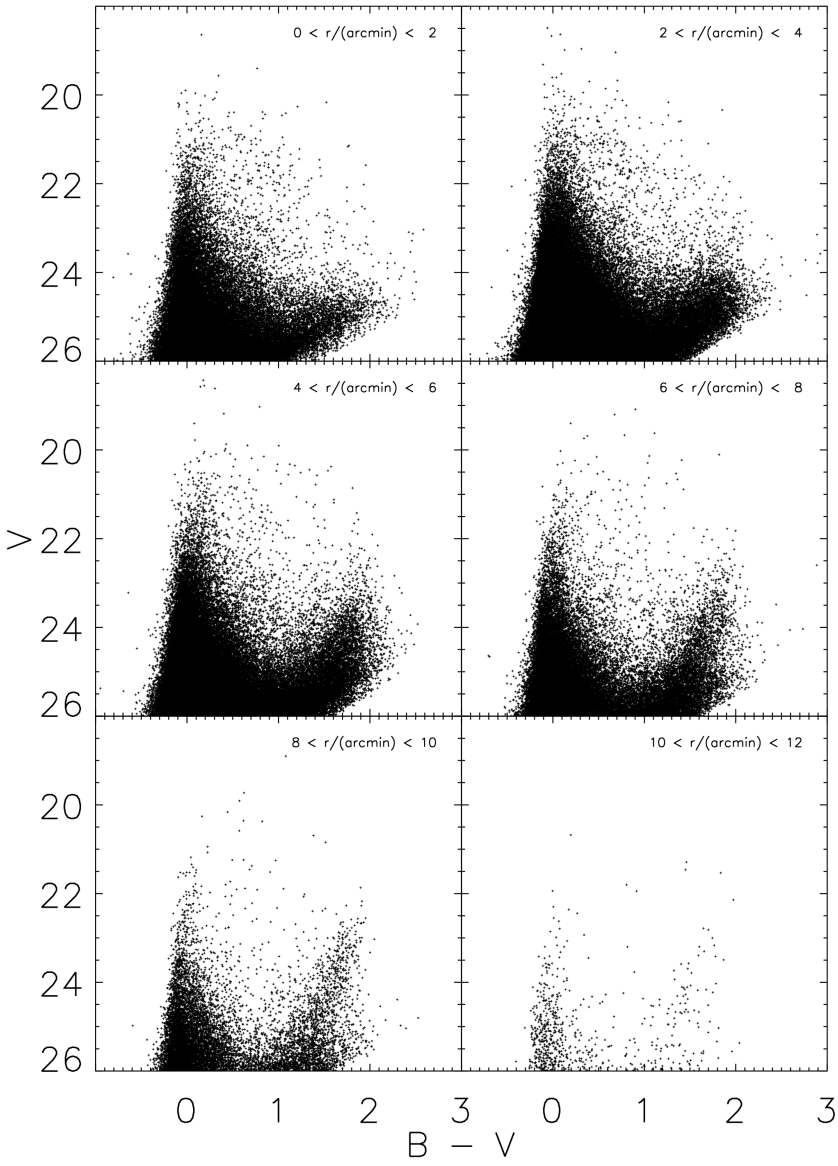

Figure 2.7: Radial variation of the color-magnitdue diagrams in M101. The radial distances from the center of M101 were deprojected for each star using an inclination of 18° and position angle of 39° (Bosma et al., 1981).

candidates are more or less the same except for the RSGs, which become increasingly more prevalent at larger radii. Adopting an inclination angle of 18° and position angle of 39° for M101 (Bosma et al., 1981), we computed the deprojected angular distance,

relative to the center of M101, for each star in our catalog and plotted CMDs in six 2′ wide annuli (Figure 2.7). At a glance, Figure 2.7 exhibits the same qualitative behavior seen in the spatial distributions: with increasing radius the RSGs become more prevalent while the number of bright ($V < 22$) BSGs decreases.

The monotonic decrease in the ratio of blue to red supergiants (B/R) with increasing radius and metallcity is a phenomenon that has been well documented by many observers. Langer & Maeder (1995) and Eggenberger et al. (2002) have reviewed the observational studies of the blue-to-red supergiant ratio. There are a number of factors that may contribute to the observed ratio. Maeder et al. (1980) suggested that the length of time that a star spends as a He burning RSG decreases with increasing metallicity due to enhanced mass loss thereby increasing the time spent as a He burning WR star. Massey & Johnson (1998) provide support for this scenario by examining the WR and RSG populations in NGC 6822, M33, and M31 showing that the ratio of WR to RSGs monotonically increased with metallicity. Similarly, studies of the Magellanic clouds, along with OB associations and open clusters in the the Milky Way at various radii, have shown that the B/R ratio displays a marked decrease with metallicity (Meylan & Maeder, 1982; Humphreys & McElroy, 1984; Eggenberger et al., 2002).

We have quantified the apparent trends in the CMDs by calculating the number ratio of candidate BSGs to RSGs as a function of radius and metallicity for three magnitude intervals: (i) $V < 22$, (ii) $22 \leq V < 23$, and (iii) $V \geq 23$ in bins of 0′.5. The radii were converted to metallicity using the oxygen abundance gradient from Kennicutt et al. (2003) and adopting a solar oxygen abundance of $12 + \log(\mathrm{O/H}) = 8.65$ (Allende Prieto et al., 2001). The resulting B/R ratio versus radius and metallicity trends are shown in Figure 2.8. We find that while the relative offsets between each magnitude interval differ, the slopes are comparable and agree to within <10% when comparing the two fainter magnitude intervals (ii) and (iii). However we note that the slope in the brightest magnitude interval (i) differs by ∼25% when compared to the two fainter ones. RSGs brighter than $V = 22$ are quite scarce, as seen in Figure 2.7, and our analysis of the foreground contribution indicates that at least 15% may be foreground stars, therefore the B/R ratio may not be trustworthy in this magnitude interval. Consequently we have taken the average of the slopes from magnitude intervals (ii) and (iii) and find a B/R ratio gradient of $\Delta\log(\mathrm{B/R})/\Delta\mathrm{Z} = 95\pm20$ roughly consistent with the ∼65

found by Humphreys & McElroy (1984), ∼45 by Meylan & Maeder (1982), and ∼80 by Eggenberger et al. (2002). We are hesitant to interpret the observed radial decline in the B/R ratio as being solely due to the decreasing metal abundance of M101 given that a spatially varying mean stellar age could also manifest a B/R ratio radial dependence. In order to disentangle the effects of age and metallicity on the B/R ratio, knowledge of the radial star formation history is required, thus we defer to a future paper a more thorough analysis.

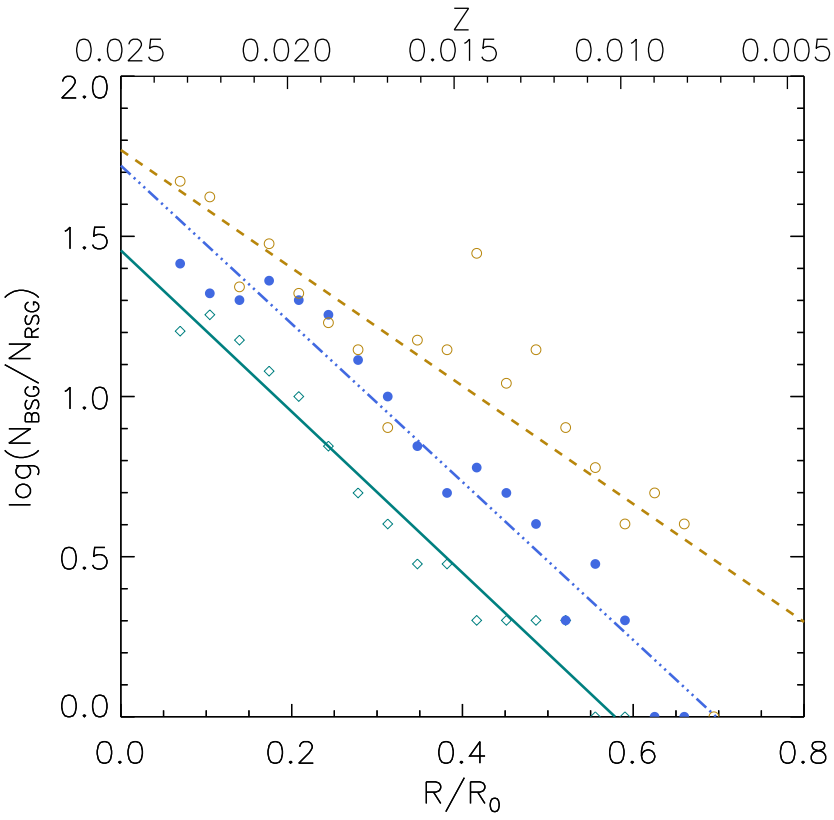

Figure 2.8: Radial trend of blue-to-red supergiant ratio using the luminous massive star candidates in the BSG and RSG subsets (see §3 for details). The ratio of BSG to RSG stars have been calculated in three different magnitude intervals in 0″.5 bins. The magnitude intervals are $V < 22$ (gold), $22 < V < 23$ (blue), and $V > 23$ (green), and the best fit lines are shown for each. Radii have been converted to metallicity using the oxygen abundance gradient from Kennicutt et al. (2003) assuming a solar oxygen abundance of $12 + log(O/H)_{\odot} = 8.69$ (Allende Prieto et al., 2001).

2.5 The Massive Star Content of Giant Star Forming Complexes

The large star forming complexes, or giant H II regions (GHR), of a galaxy are small-scale examples of extreme star formation that are similar to starburst galaxies. GHRs contain many young spatially coincident star clusters but the formation history could be coeval or separated by several million years. The CMD is a powerful tool used to gain insights into the stellar populations present as well as extinction properties. Studying the visual morphology and spatial locations of stars, in conjunction with the CMDs, provides clues into the formation of the GHRs. In this context we present and discuss the resolved stellar content, which has not been previously studied in detail, within the GHRs NGC 5458, NGC 5453, NGC 5461, NGC 5451, NGC 5462, and NGC 5449.

We have selected stars from inside a $30''$ box centered on each GHR and have created CMDs shown in Figure 2.9. Stellar isochrones between the ages $5-100$ Myrs and masses $1-100$ $M_{\odot}$ (Bertelli et al., 1994) and have been included to aid in the interpretation of the stellar content and star formation history. The GHRs in the inner regions are expected to contain a sizable contribution from the disk which decreases in density exponentially with increasing radius. We have gauged the degree of disk contribution to the GHR CMDs by extracting stars in $30''$ boxes from regions in M101 that do not show any obvious signs of star formation. While the density of stars decreases with radius, the overall morphology of the CMDs remains more or less the same. Figure 2.10 shows a representative disk CMD at a radius of $3'$. Comparing the CMDs of the GHRs to disk stars, we see that our analysis of the the massive star populations should not be affected by contamination since the density of bright main-sequence/blue supergiants stars is low and the number of stars with $(B-V) > 1.3$ and $V < 25$ is effectively zero. At larger radii, the exponential nature of the disk will further reduce the contamination.

In addition to CMDs, we have analyzed the spatial distributions of BSGs and RSGs present in each GHR visually and quantitatively, through the use of a two dimensional Kolmogorov-Smirnov (2-D KS) test, to look for spatial variability in the mean stellar age. We have separated the stars into three groups: $B1, B2$, and R. We have chosen $B1$ and $B2$ to correspond to BSGs with $V < 22$ and $22 < V < 23.5$, respectively. BSGs in $B1$ only exist on the optical CMD between the ages of 5 and 10 Myrs while

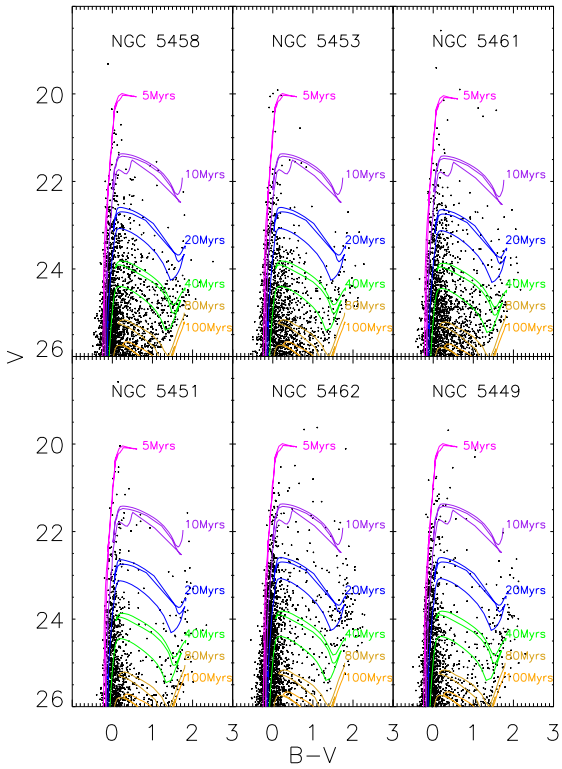

Figure 2.9: Color-magnitude diagrams for the giant H II regions with NGC designations. Regions are sorted by increasing distance from the center and have radial angular distances of $3'.1$, $3'.5$, $4'.5$, $5'.3$, $6'.0$, and $6'.6$, respectively.

those in $B2$ may exist anywhere between 0 and 30 Myrs. RSGs with $22 < V < 24$ are assigned to R and may be present on the CMD between the ages of 10 and 20 Myrs. By comparing the spatial distributions of all three groups, we are able to determine the spatio-temporal formation history for each GHR. We show the spatial distributions of each group in Figure 2.11 for visual inspection and make use of the 2-D KS test for a quantitative comparison. In the 2-D KS test, the test statistic, D_{KS}, is defined as the maximum cumulative difference between the empirical $F(\alpha, \delta)$ distribution functions. The probability of drawing a smaller D_{KS}, assuming the two distribution functions are identical (ie. the null hypothesis is true), is given by $100\% \times p$.

As with any statistical test, it is important to know how various parameters affect the results, thus we have performed Monte Carlo simulations to test the sensitivity of the 2-D KS test to sample size and distribution function parameters such as spatial

extent and offset. Using the same 30″ FOV, we simulated Gaussian spatial distributions and varied the $FWHM$ by 6″.5 - 20″, and offset the two distributions by 0″-5″. We tested several different scenarios where the distribution functions were identical and where they differed by either FHWM, offset, or both. For each scenario, we performed 10^4 iterations and performed the 2-D KS test each time. We found that the 2-D KS test was extremely sensitive to spatial offsets and rejected the null hypothesis at high significance ($p < 0.005$) when identical distributions were offset by $\geq 1''$. When the distributions were spatially coincident, but differed in $FWHM$, the null hypothesis was reliably rejected to high significance ($p \ll 0.001$ and no greater than $p = 0.05$) when $|1 - FWHM1/FWHM2| \geq 0.1$. For cases when $|1 - FWHM1/FWHM2| < 0.1$, the 2-D KS test was incapable of telling the distributions apart at high significance and the p values ranged between 0.09 and 0.15. Furthermore when we forced the distributions to be equal but varied the $FWHM$, we found that p values were always ≥ 0.2. Based on our Monte Carlo simulations we conclude that it is safe to assume that two distributions are significantly different when $p \lesssim 0.08$ and identical when $p > 0.2$. For intermediate values, $0.08 < p < 0.15$, we take a conservative approach and assume that the distributions are similar enough to be considered identical. When varying the sample sizes, we found that our conclusions held as long as the sample size of each distribution was N $\geq$ 10. When a distribution had N $<$ 10, the 2-D KS test was no longer capable of separating distributions that were slightly or even moderately different.

2.5.1 NGC 5458

The CMD of NGC 5458 in Figure 2.9 shows a well defined main-sequence and BSGs extending up to $V \approx 20$ indicative of star formation as recent as 5 Myrs ago. Integrated spectroscopic observations in the FUV indicate that NGC 5458 is dominated by stellar populations 5.5 to 6.0 Myrs old consisting of 150 O type stars and 18 WR stars (Pellerin, 2006). In addition to a young population of stars, we see that there are red stars ranging between $23.5 < V < 25$ thus NGC 5458 also contains a more evolved component between 20 and 40 Myrs old. Fainter than $V = 25$, the CMD is dominated by the disk of M101 (Figure 2.10). The spatial distributions of stars in $B1$, $B2$, and R do not show any obvious differences by eye (Figure 2.11) which is confirmed by the 2-D KS test. NGC 5458 thus appears to be a single complex of star formation that has been producing

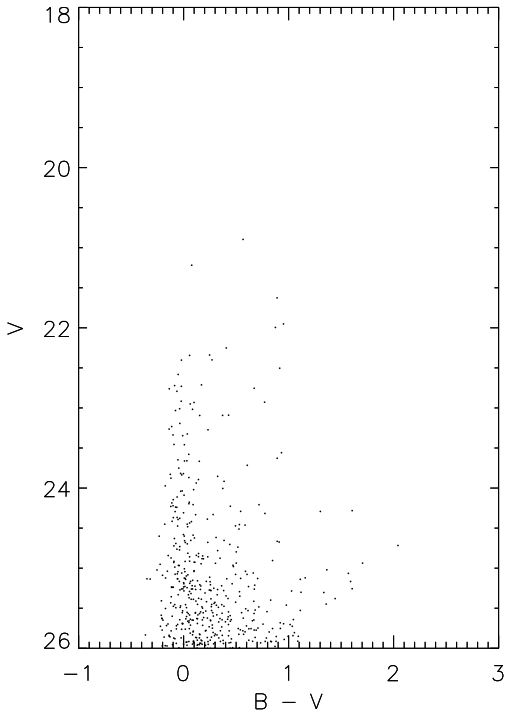

Figure 2.10: Representative color-magnitude diagram of the disk component at a radius of 3′. At larger radii, the color-magnitude diagrams look similar however there are fewer stars due to the stellar exponential density profile.

stars continuously over the last ∼40 Myrs.

2.5.2 NGC 5453

The CMD of NGC 5453 is similar to NGC 5458 although it lacks the population of stars with ages ∼5 Myrs. Eight candidate clusters are located within 30″ of the center of NGC 5453 (Barmby et al., 2006) and account for the brightest blue objects with $V < 20.5$ in Figure 2.9. The diffuse X-ray luminosity generated by powerful stellar winds and supernovae is time-dependent and increases by almost two orders of magnitude for ages between 3 and 10 Myrs then disappears for ages greater than 40 Myrs (Oskinova, 2005). For a single 10^6 $M_\odot$ cluster at 10 Myrs, the X-ray luminosity is $\log(L_X/L_\odot) \sim 3$ (Oskinova, 2005) which, at the distance of M101, corresponds to a flux that is below the detection threshold of the *CHANDRA* image of M101 (Kuntz et al., 2003) in the hard bandpass and only a few times brighter than the detection threshold of the

soft bandpass. NGC 5453 was undetected by *CHANDRA* (Kuntz et al., 2003) and is consistent with models of cluster X-ray luminosity if the dominant population is $\geq$10 Myrs and the brightest objects are $10 - 20$ Myr clusters with masses $\lesssim 10^4$ $M_\odot$. The spatial distributions of $B1, B2$, and R stars do not differ at high significance leading us to suspect that the star formation in NGC 5453 has been uninterrupted and spatially invariant, similar to NGC 5458.

2.5.3 NGC 5461

NGC 5461 is one of the brightest GHRs within 10 Mpc (Kennicutt, 1984) with a surface brightness commensurate to the most active starburst regions and an Hα flux on par with the ionizing flux of super star clusters (Kennicutt, 1988; Luridiana & Peimbert, 2001). At a glance the CMD tells us that there are at least two dominant populations, one that is $\leq$5 Myrs old and another that is >10 Myrs. Spectral synthesis of the optical to NUV wavelengths indicate that the dominant stellar population is very young, (3 to 4.5 Myrs) and from the ratio of Hα to Hβ, extinction is on the order of $E(B-V) = 0.23$ (Rosa & Benvenuti, 1994). The FUV spectrum of NGC 5461 is best fit by a stellar population consisting of 175 O stars and 18 WR stars between the ages of 3.3 and 4 Myrs, in agreement with optical data, although the FUV spectrum is best fit by zero reddening (Pellerin, 2006). Integrated FUV observations of a region with variable extinction are likely to under-represent the most reddened stars due to the steep extinction curve from optical to UV (Cardelli et al., 1989) hence the discrepancy in the measured extinction. The visual image of NGC 5461 shows a filamentary core indicating that there are regions that may be highly reddened. The width of the main-sequence, at magnitudes where uncertainties are small, supports the proposition of differential reddening on the order of $\Delta A_V \approx 1$ magnitude.

Examining the spatial distributions of stars, we find that $B1$ and R stars are primarily located to the Southwest of the extremely bright Hα source H1105 (Hodge et al., 1990) which contains six massive clusters with ages <5 Myrs (Chen et al., 2005). Comparing the $B1$ stars R stars confirms that they arise from the same spatial distribution ($p = 0.3$) whereas the comparison between $B2$ and R exhibits differences that are statistically significant ($p = 0.08$). Comparing $B1$ to $B2$, the 2-D KS test yields $p = 0.09$ which we are not comfortable interpreting as definitively different given the results of

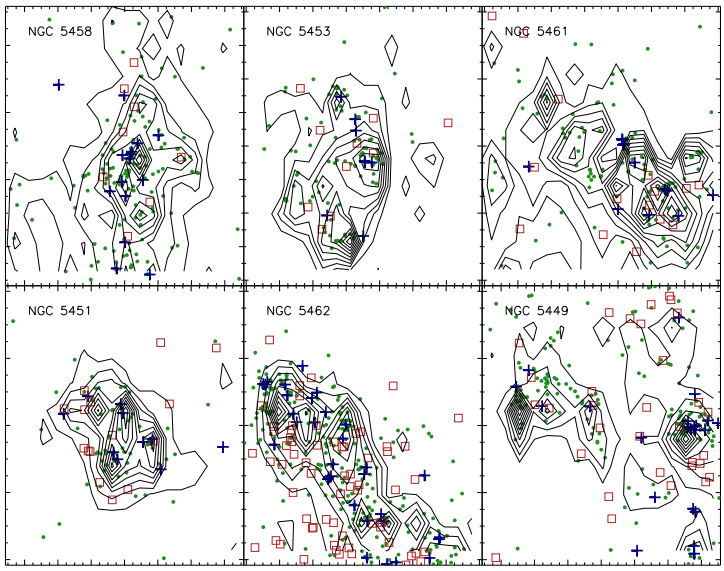

Figure 2.11: Spatial distribution of stars in the giant H II regions. The subgroups $R, B1$, and $B2$, which are defined in the text, are shown as red squares, navy crosses, and green points, respectively. Stellar density contours for stars with $V < 25$ are shown for reference.

our Monte Carlo tests. However when we removed the Easternmost $B1$ star, which is much further away from its nearest neighbors than any other $B1$ star, the significance increased to $p = 0.03$ which is well within the our limits for a significant difference. Combining the results of the 2-D KS test with the CMD and previous studies of NGC 5461, we come to the conclusion that star formation occurred first in the Southwest, $5 - 20$ Myrs ago, and has propagated to the Northeast to create the youngest stars and clusters which make up H1105.

2.5.4 NGC 5451

The CMD of NGC 5451 (Figure 2.9) exhibits a clear RSG sequence which extends from $V = 25$ to $V = 21.5$ showing that star formation has been ongoing between 15 and 40 Myrs ago. The existence of main-sequence stars or BSGs as bright as $V = 20$ along with the presence of several H II regions (Hodge et al., 1990) indicates that star formation is ongoing. Comparing the spatial locations of blue to red stars in Figure 2.11, we find that the overall distributions do not differ considerably thus star formation in NGC

5451 has been continuous and monolithic within the last 40 Myrs.

2.5.5 NGC 5462

NGC 5462 is one of the largest GHRs in M101 and has been shown to contain as many as 25 young massive clusters (Chen et al., 2005). Inspection of the CMD (Figure 2.9) reveals an interesting mix of stellar populations with the youngest stars consistent with ages of ∼10 Myrs. RSGs span roughly three magnitudes starting at $V = 24$ indicating star formation additionally occurred between 15 and 40 Myrs ago. While constant, the amplitude of the star formation rate may have been extremely high during the period of $15-30$ Myrs ago given that RSGs are significantly overabundant in that age range. The maximum mass of a cluster and star formation rate are tightly correlated parameters (Larsen, 2002). Chen et al. (2005) find that the two most massive clusters in NGC 5462 have ages >10 Myrs which may support the presence of an epoch of enhanced star formation rate occurring ≥10 Myrs ago.

$B1$ and $B2$ stars are tightly distributed along the major axis of NGC 5462 while the R stars are spread throughout showing the highest density Southeast of the major axis. The 2-D KS test substantiates these apparent trends to high significance ($p \leq 0.02$) indicating that the $B1$ and $B2$ stars differ in spatial distribution from R stars while $B1$ and $B2$ stars are identically distributed ($p = 0.8$). NGC 5462 is the brightest GHR in X-rays with a strong diffuse component, due to heating from the stellar winds of extremely massive stars, Southeast and spatially offset from the H II emission in the Northwest (Williams & Chu, 1995; Wang et al., 1999; Kuntz et al., 2003; Sun et al., 2012). Visually there exists a clear separation between the stellar concentrations and the nebular emission which in conjunction with the analysis of the spatial distributions of $B1$, $B2$, and R stars, suggests that star formation began in the Southeast between 20 and 30 Myrs ago and has propagated in the Northwest direction subsequently producing the <10 Myr population.

2.5.6 NGC 5449

The CMD (Figure 2.9) of NGC 5449 shows a spread of ∼3 magnitudes in the RSG luminosities and the presence of blue stars extending up to $V = 20$. Star formation

over the last ∼40 Myrs therefore appears to have been continuous and is ongoing given that there are many H II regions within (Hodge et al., 1990). Figure 2.11 shows that the spatial distribution of the stars is bimodal and the division of $B1$, $B2$, and R stars is not uniform. By eye, there appears to be more $B1$ and R stars in the West and when comparing $B1$ stars to $B2$ and R stars, we find that to very high significance ($p \ll 0.01$) the $B1$ stars have a spatial distribution that is significantly different from $B2$ and R stars. Comparing the $B2$ and R stars, we find that they are statistically identical but not to high significance ($p = 0.15$), therefore the only statistically significant difference between the two concentrations of stars is the overabundance of $B1$ stars in the West. Furthermore the location of the most luminous H II region within the NGC 5449 star forming complex is to the East (Hodge et al., 1990) and given that the visually brightest blue stars are not the most massive, due to large bolometric corrections associated with high effective temperatures, we suggest that the Western concentration is likely to be more evolved than the Eastern concentration.

2.6 Summary and Future Work

Using archival *BVI HST*/ACS images we have created a catalog of luminous stars covering most of the optical disk in M101. Unprecedented spatial resolution paired with excellent characterization of the *HST*/ACS point spread function and detectors have allowed for the minimization in the numbers of non-stellar sources, such as background galaxies and unresolved clusters, and the ability to maintain high photometric precision and depth even in regions of M101 where stellar crowding is extreme. Using the catalog we have studied the massive star content of M101 and our main results are the following:

1. We have identified luminous massive star candidates, for future study, using color-magnitude and color-color diagrams. We separated the luminous massive star candidates into three subsets: luminous OB type stars and blue supergiants, yellow supergiants, and red supergiants. We modeled the foreground contamination in the direction of M101 using the Besançon Galactic population synthesis model (Robin et al., 2003) and conclude that using our selection criteria, $\sim 100\%$ of the 25,603 luminous OB type stars and blue supergiants, $60 - 80\%$ of the 3,105 yellow supergiants, and $85 - 95\%$ of the 2,294 red supergiants are members of M101.

2. Examining the spatial distributions of our candidates, we find that the blue and yellow supergiants share a common distribution however the red supergiants are more common in the outer parts of the galaxy, supported by color-magnitude diagrams at various radii. The blue to red supergiant ratio decreases smoothly with radius and after converting radius to metallicity, we observe a decrease of roughly two orders of magnitude over 0.5 dex in metallicity. However as mentioned in the text, the dependence on metallicity remains uncertain since a spatially variable star formation history could result in a blue to red supergiant ratio that decreases radially.

3. We discuss the resolved stellar content of giant H II regions NGC 5458, 5453, 5461, 5451, 5462, and 5449. Through the use of a 2-D Kolmogorov-Smirnov test, we quantitatively compare the spatial distributions of blue and red supergiants in different magnitude intervals in order to determine the spatio-temporal formation history for each region. We find that in all the star forming regions, the color-magnitude diagrams display evidence for continuous star formation over the last 40 Myrs. The analysis of the spatial distributions of stars in NGC 5458, 5453, and 5451 showed no statistically significant differences between young and more evolved stars whereas NGC 5461, 5462, and 5449 showed differences that were statistically significant indicating the presence of a spatially varying mean stellar age.

Future work on the subject of massive star population in M101 will address its formation history and the properties of its most luminous stars. Paper II will be a comparison and inter-comparison of the star formation histories in arm, inter-arm, and regions of intense star formation. Papers III and IV will focus on the properties of the most luminous and variables stars. We are using the LBT multi-color four year imaging survey of nearby galaxies (Kochanek et al., 2008) to identify the luminous stars in M101 that show evidence for instability from their short-term variability. Their light curves and photometric properties will be discussed in Paper III. In the fourth and final paper in this series, we will report on spectroscopy of the luminous variables and other high luminosity stars selected from our catalog.

2.7 Acknowledgments

Our research on massive stars is supported by the National Science Foundation AST-1019394 (R. Humphreys, P.I.). All of the data presented in this paper were obtained from the Mikulski Archive for Space Telescopes (MAST). STScI is operated by the Association of Universities for Research in Astronomy, Inc., under NASA contract NAS5-26555. Support for MAST for non-HST data is provided by the NASA Office of Space Science via grant NNX09AF08G and by other grants and contracts.

Chapter 3

Spatial Variations in the Recent Star Formation History (Grammer & Humphreys, 2014)

Abstract

We investigate the star formation history (SFH) as a function of radius in M101 using archival *HST* ACS photometry. We derive the SFH from the resolved stellar populations in five $2'$ wide annuli. Binning the SFH into time frames corresponding to stellar populations traced by Hα, far ultraviolet (FUV), and near ultraviolet (NUV) emission, we find that the fraction of stellar populations young enough to contribute in Hα is $15\% - 35\%$ in the inner regions, compared to less than 5% in the outer regions. This provides a sufficient explanation for the lack of Hα emission at large radii. We also model the blue to red supergiant ratio in our five annuli, examine the effects that a metallicity gradient and variable SFH have on the predicted ratios, and compare to the observed values. We find that the radial behavior of our modeled blue to red supergiant ratios is highly sensitive to both spatial variations in the SFH and metallicity. Incorporating the derived SFH into modeled ratios, we find that we are able to reproduce the observed values at large radii (low metallicity), but at small radii (high metallicity) the modeled

and observed ratios are discrepant.

3.1 Introduction

Observations of spiral galaxies indicate that the stellar populations and emission properties are strongly dependent on radius. Early observations of the massive star content in M33 demonstrated that the ratio of blue to red supergiants (B/R ratio) decreases with distance from the center (Walker, 1964). Subsequently, many other authors have observed similar phenomena, in a variety of galaxies, which have been attributed to an abundance gradient (Hartwick, 1970; Humphreys, 1979; Humphreys & Davidson, 1979; Humphreys, 1980; Humphreys & McElroy, 1984; Eggenberger et al., 2002; Grammer & Humphreys, 2013). As discussed in Langer & Maeder (1995), and more recently Meynet et al. (2011), stellar evolution models are able to reproduce the observed B/R ratios at either high or low metallicity. However, there is not yet a set of models that reproduce the B/R ratios at both high and low metallicity (see Meynet et al. (2011) and references therein). In addition to metallicity, the B/R ratio is also dependent on mass and thus the star formation history (SFH) (Langer & Maeder, 1995; Dohm-Palmer & Skillman, 2002; Vázquez et al., 2007; McQuinn et al., 2011). To compare the B/R ratios between galaxies, or even different regions in a single galaxy, one must be certain that the underlying SFH is identical. Any systematic variation in the star formation history necessarily affects the radial dependence of the B/R ratio.

Broad and narrow band imaging from IR to X-Ray suggest that similar to the stellar populations, the emission properties of galaxies vary radially. Recently, deep observations of galaxies using *Galaxy Evolution Explorer (GALEX)* have demonstrated ultraviolet (UV) emission that is considerably more extended than optical emission, a property characterized as an extended UV disk (XUV) (Thilker et al., 2005, 2007). Moreover, the UV disk is roughly twice that of Hα (Boissier et al., 2007; Goddard et al., 2010) suggesting that in the outskirts of XUV galaxies, O stars are rare but B and A type stars are abundant. A truncated initial mass function (IMF) in low density star forming regions or statistical sampling of the IMF could suppress the formation of massive O stars, thereby leading to the absence of Hα at large radii (Boissier et al., 2007; Meurer et al., 2009; Goddard et al., 2010; Lee et al., 2011; Koda et al., 2012). An alternative

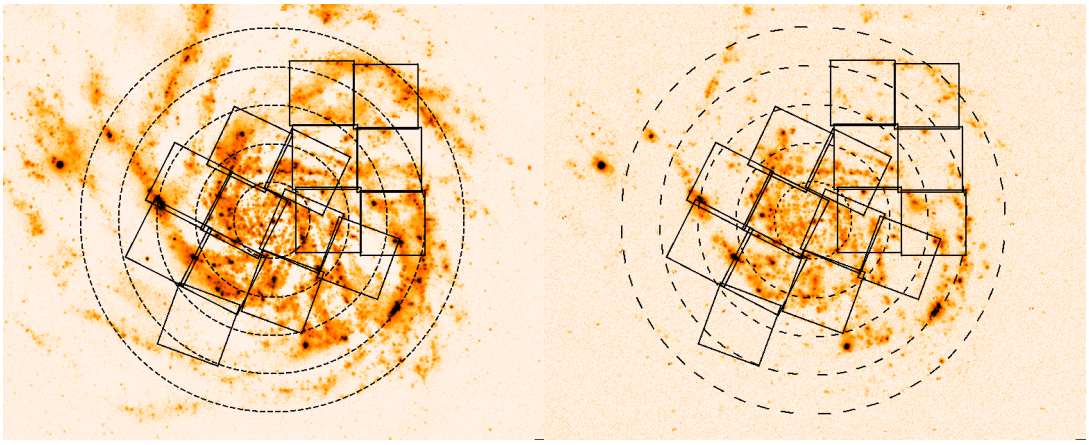

Figure 3.1: Images of M101: *GALEX* FUV (left) and KPNO Schmidt Hα (right). Overlaid are five dashed annuli $2'$ wide and extend out to $10'$. The ACS fields-of-view are given by the solid black lines. Pixel values are displayed logarithmically and range from zero to the maximum. The contrast for both images is identical.

explanation is that the star forming regions are, on average, older in the outskirts (Thilker et al., 2005; Zaritsky & Christlein, 2007). Comparing the stellar populations in complexes observed in both UV and Hα to complexes seen only in UV, suggests the lack of Hα may be attributed to differences in stellar population age (Thilker et al., 2005; Gogarten et al., 2009; Alberts et al., 2011). Thus, discrepancies between the UV and Hα profiles, and the radial dependence in the B/R ratio, may share a common origin: radial variations in the recent SFH.

Multi-band photometry of M101 has demonstrated that not only does it possess an XUV disk (Thilker et al., 2007), but that the Hα emission is considerably less extended than the UV emission (Mihos et al., 2013) (Figure 3.1). Resolved stellar population studies have also shown that the B/R ratio decreases dramatically with radius (Grammer & Humphreys, 2013, hereafter Paper I). These properties make M101 an ideal target for studies of massive star formation and its connection between the observed stellar populations and global emission properties. For this work, we aim to derive the radial SFH by modeling the resolved stellar populations in radial bins (annuli). Our goal is to examine the variations in the radial SFH and their connection to the radial dependence in the B/R ratio as well as differences in the UV and Hα radial profiles.

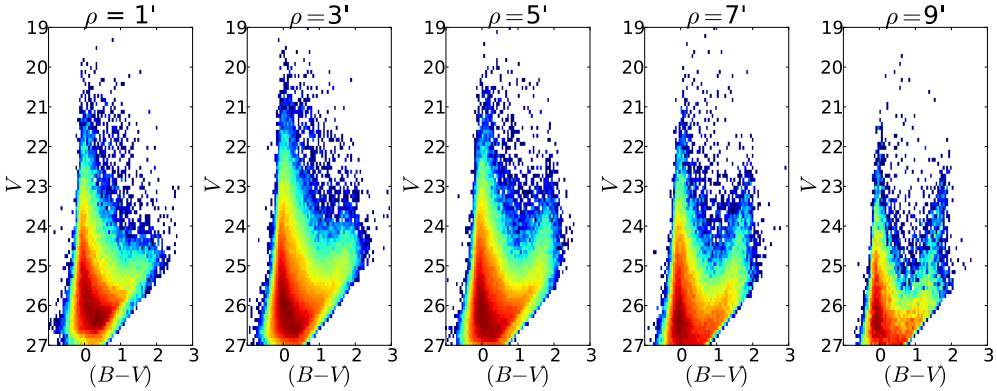

Figure 3.2: V vs. $(B-V)$ CMDs for each annulus. The radial center is denoted at the top of each CMD. The color map is linear in stellar density with lighter colors indicating higher densities. A color version is available online with blue indicating low stellar density and dark red indicating high stellar density. The V vs. $(V-I)$ CMDs are shown in the Appendix of the online version.

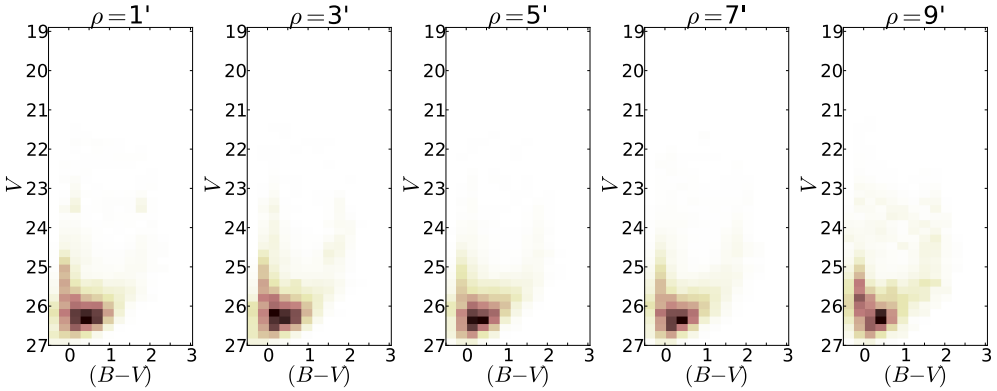

Figure 3.3: Residual V vs. $(B-V)$ CMDs. Residuals were produced by taking the difference between the model and observations and median filtering the results using a 0.25×0.25 mag^2 filter. The color map is linear with darker regions indicating larger residuals. The largest residuals systematically occur at magnitudes fainter than $V = 26$ due to incompleteness.

The resolved stellar photometry is summarized in §2. In §3 we discuss our methods for determining the SFH. We examine the radial variations in the SFH in §4. Finally, we evaluate the likelihood that the radial variations in the SFH are responsible for the

differences in the Hα and UV radial profiles as well as the shape of the B/R ratio and its dependence on radius. The results are summarized in the last section.

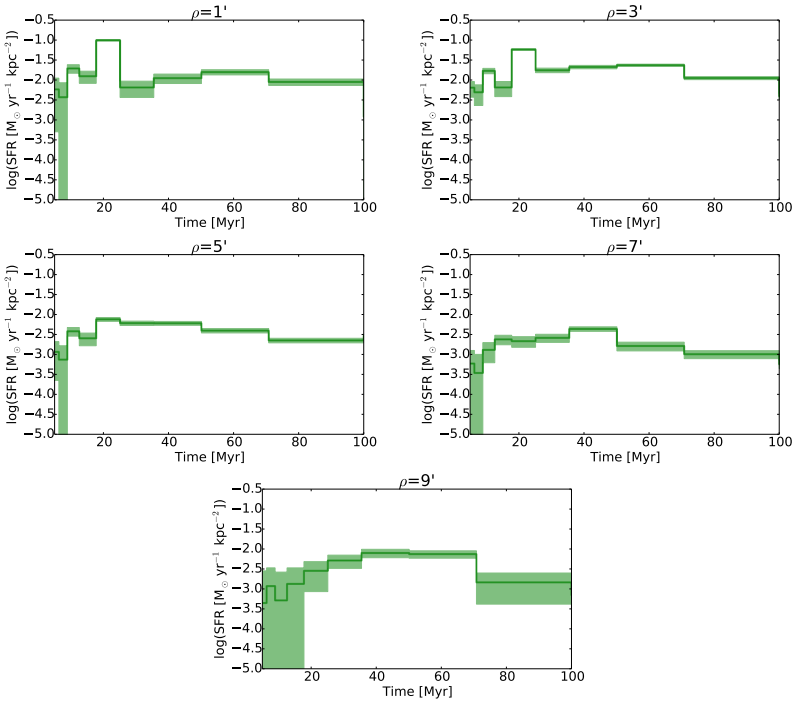

Figure 3.4: The SFHs for the five annuli. Each annulus is identified by its radial mid-point in arcminutes. The SFHs were determined by comparing observed CMDs to synthetic CMDs. The shaded regions denote the 68% confidence intervals.

3.2 Data and Photometry

We used archival observations of M101 from the *The Hubble Space Telescope (HST)* Advanced Camera for Surveys (ACS) Wide Field Camera to produce a catalog of $\sim$ 500000 resolved stars [1]. Our catalog has photometric errors that are less than 10% for $B < 24.5$, $V < 24.3$, and $I < 24.0$ and is 50% complete down to $B = 27.0$, $V = 26.5$, and $I = 26.2$ for the fields from proposal ID 9490; fields from proposal ID 9492 are 50% complete down to $B = 27.3$, $V = 26.8$, and $I = 26.4$. See Paper I for details regarding our photometric technique.

[1] http://etacar.umn.edu/LuminousStars/M101/M101-HST-ACS-WFC- Catalog.txt

We assigned galactocentric angular distances to each star assuming an inclination angle of 18° and a position angle of 39° (Bosma et al., 1981). We then divided the stars into five 2′ wide annuli (see Figure 3.1). At a distance to M101 of 6.5 Mpc (Shappee & Stanek, 2011), each annulus has a width of ∼1.7 kpc, and the five annuli span a radial distance of ∼17 kpc. For each annulus, we calculate the observed area taking into account the coverage of the ACS fields. We identify each annulus by its radial mid-point in arcminutes. In Figure 3.2 we display the three-dimensional color-magnitude diagrams (CMDs) for each annulus: the color-coded dimension indicates the density of stars, in color-magnitude space, scaled by peak stellar density.

3.3 Modeling the Color-Magnitude Diagrams

3.3.1 Method

The method of modeling observed CMDs with synthetic CMDs to extract the SFH is a well established technique (Tosi et al., 1991; Gallart et al., 1999; Hernandez et al., 1999; Holtzman et al., 1999; Dolphin, 2002; Skillman et al., 2003; Harris & Zaritsky, 2004). We used StarFISH (Harris & Zaritsky, 2004) to derive the SFH for each of our annuli. The user-supplied parameters to StarFISH are age, stellar mass and metallicity range, the slope of the IMF, binary fraction, photometric error functions, extinction, and the distance modulus. Single-age synthetic CMDs are then created from the given parameters. The observed CMDs are modeled as the weighted sum of all the synthetic CMDs while simultaneously minimizing χ^2. The fit with the lowest χ^2 is returned as the most likely SFH.

Though we are most concerned with the massive star population of M101, our CMDs contain stellar populations with a range of ages and masses. Thus, to fit the CMDs we assume an IMF slope of -2.35 (Salpeter, 1955) for stellar masses $0.1 - 100 M_{\odot}$, a binary fraction of 0.5, and a distance modulus of $\mu_0 = 29.05$ (Shappee & Stanek, 2011). Crowding, completeness, and observational errors are incorporated into the model CMDs by supplying StarFISH with the input and output magnitudes of our artificial star tests as well as whether the artificial stars passed our quality criteria (discussed in Paper I). From these parameters, CMDs were synthesized using the Padova stellar isochrones (Marigo et al., 2008) with metallicities in the range of $0.005-0.020$, and

ages $4 - 500$ Myr spaced logarithmically. We eliminate metallicity as a free parameter by assigning values from the observed abundance gradient (Kennicutt et al., 2003) to each annulus. Similarly, we account for extinction by applying the radial extinction curve from Lin et al. (2013) to the library of synthetic CMDs. The library of synthetic CMDs was then used to model the stellar populations in each annulus. The output of StarFISH is the amplitude for each time bin, in numbers of stars, which was converted to SFR by multiplying by the mean mass and dividing by the width of the time bin. The uncertainties associated with each amplitude is the 68% confidence interval resulting from Monte Carlo simulations performed by StarFISH.

3.3.2 Evaluating the Reliability of the Star Formation Histories

We assess how well the model CMDs reproduce the observations by simulating observations drawn from the best-fit SFH. We then created residuals diagrams by subtracting the observed CMDs from the model CMDs, scaled by the number of observed stars in each color-magnitude bin. The normalized residuals are displayed in Figure 3.3 after having applied a 0.25×0.25 mag^2 median filter to increase the contrast. Based on Figure 3.3, the model CMDs adequately reproduce the observations for magnitudes brighter than $V \approx 26$, where residuals are small ($< 10\%$). At $V \approx 26$, roughly corresponding to the main-sequence turn off of the 100 Myr isochrone, the residuals increase rapidly, which we attribute to incompleteness (see §2).

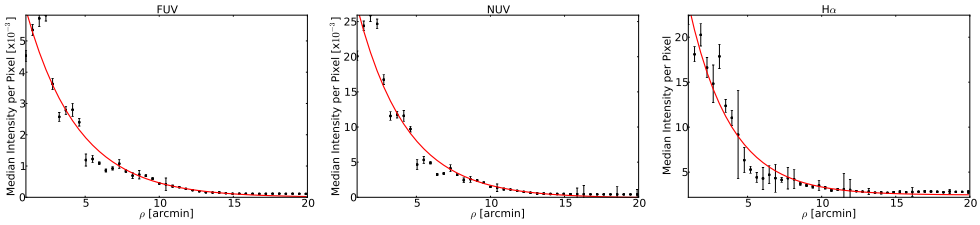

Figure 3.5: Radial profiles for FUV, NUV, and Hα. The solid lines are the best-fit exponential profiles. The best-fit scale lengths, in arcminutes, are 3.36 ± 0.18, 3.51 ± 0.23, and 2.62 ± 0.32, respectively. At the assumed distance of M101, the scale lengths correspond to 6.32 ± 0.34, 6.60 ± 0.43, and 4.93 ± 0.60 kpc.

The reliability of the reported SFRs were evaluated by performing a series of Monte Carlo simulations. We created synthetic CMDs, assuming a constant SFR, which we

then used as input to StarFISH. We then compared the input and output SFH. This test was performed one hundred times for SFRs between $10^{-2} - 10^{-7}$ $M_\odot$ yr^{-1} in steps of 0.5 dex. Our results indicate that SFRs higher than $\sim 10^{-4.5}$ $M_\odot$ yr^{-1} were consistently recovered with errors less than 15% for all ages and metallicities. Lower SFRs frequently had recovered values that differed from the input by up to 50%. Given the range in observed surface areas, the SFR of our annuli at $1'$ and $9'$ are reliable when greater than $\sim 10^{-6}$ $M_\odot$ yr^{-1} kpc^{-2}. The remaining annuli ($3'$, $5'$, and $7'$) have SFRs that are reliable down to $\sim 10^{-7}$ $M_\odot$ yr^{-1} kpc^{-2}.

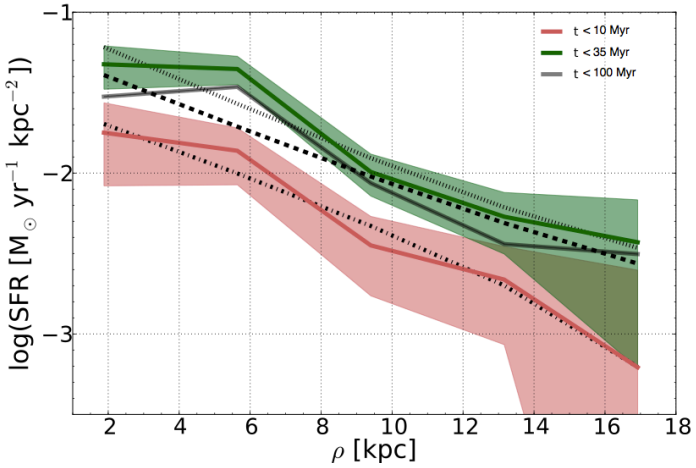

Figure 3.6: Mean SFRs as a function of radius for stars < 10 Myr, < 35 Myr, and < 100 Myr. The shaded regions surrounding the lines denote the 1σ error bars. Exponential functions were fit to each of the radial SFR profiles, with best-fit scale lengths (in kpc) of 4.65 ± 0.21 (< 10 Myr; dot-dashed line), 6.38 ± 0.26 (< 35 Myr; dashed line), and 6.30 ± 0.15 (< 100 Myr; dotted line).

3.4 Results

3.4.1 The Star Formation Histories

Since the residuals in our CMD fits are low for magnitudes brighter than $V \approx 26$, and stellar populations older than 100 Myr do not contribute to the UV and Hα emission, we only display the last 100 Myr (Figure 3.4). The overall behavior of the SFH has a clear radial dependence. The two inner annuli display discrete bursts of star formation

with peaks in SFR around 10 Myr ago and again at 20 Myr ago. At $\rho = 5'$, the peaks at 10 Myr and 20 Myr are visible in the SFH but are considerably less pronounced than those observed in the inner radii. In the outer annuli, the change in SFR is more gradual with time, although we find that the annulus at $\rho = 7'$ displays a burst in SFR at 40 Myr. Similarly, the $\rho = 9'$ annulus shows a sudden increase in SFR starting at 60 Myr ago, followed by a gradual decrease in SFR at more recent times. If we compare the SFR < 35 Myr ago to SFR $35 - 100$ Myr ago, we see that there is a decline in the relative proportion of recent star formation with radius. Consequently, a radial age gradient may exist for stars < 100 Myr old. In the following sections, we perform a more in-depth inspection of the SFH for evidence of a radial age gradient.

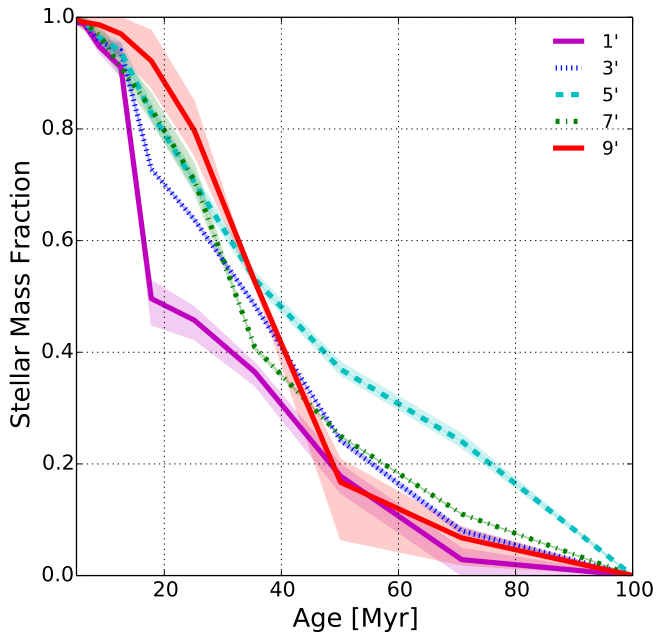

Figure 3.7: Cumulative SFH for each annulus. The stellar mass fractions are with respect to the mass formed over the last 100 Myr. The legend gives the radial center of each bin in arcminutes. The shaded regions denote the 1σ error bars.

3.4.2 Radial Variations in the Star Formation History

FUV emission from the photospheres of young O and B stars traces stellar populations with ages $\lesssim 35$ Myr, while the NUV is sensitive to older stellar populations $\lesssim 100$ Myr. Nebular Hα emission, on the other hand, provides an instantaneous glimpse of the most recent ($\lesssim 10$ Myr) bursts of massive star formation. Assuming a Kennicutt-Schmidt law (Kennicutt, 1998), the mean SFR for times < 10, < 35, and < 100 Myr should correlate with the Hα, FUV, and NUV emission profiles, respectively. Thus, we determine the mean SFR for times < 10, < 35, and < 100 Myr and plot them as a function of radius in Figure 3.6. We then fit exponential functions to each of the radial SFR profiles and display their best-fit scale lengths on the left side of Table 3.1.

To make the comparison between the radial SFR profiles and their corresponding emission profiles, we computed azimuthally averaged radial profiles, in $25''$ bins, using archival *GALEX* (Morrissey et al., 2007) and Hα (Hoopes et al., 2001) images of M101 (Figure 3.5). In our determination of the radial profiles, we found that radius at which the UV profiles reach background sky values is at $\approx 15'$. The Hα profile, on the other hand, reaches background at a radius of $10'$, which agrees well with observed Hα truncation radius of $10.6'$ determined by Martin & Kennicutt (2001). We then fit exponential functions to each of the radial emission profiles; their best-fit scale lengths are provided on the right side of Table 3.1.

There is excellent agreement between the radial SFR profiles and their corresponding radial emission profiles suggesting that the spatial variations in the SFH are well correlated with the emission properties of M101. Table 3.1 indicates that the radial SFR profiles for stars < 35 and < 100 Myr old are considerably more extended than that of stars < 10 Myr old. In the inner regions, the ratio of the SFR in the last 35 Myr to the SFR in the last 10 Myr is approximately 2, whereas at 17 kpc it increases to approximately 10 (Figure 3.6). Since this ratio does not remain static, the relative fraction of stellar populations that are < 35 Myr and < 10 Myr likely changes dramatically with radius.

To determine how the relative proportions of stars < 10, < 35, and < 100 Myr old vary with radius, we compute the cumulative SFH (Figure 3.7). The cumulative SFH shows how stellar mass has accumulated over time. The dependent variable is the fraction of stars that are older than a specified age; one minus the fraction yields the

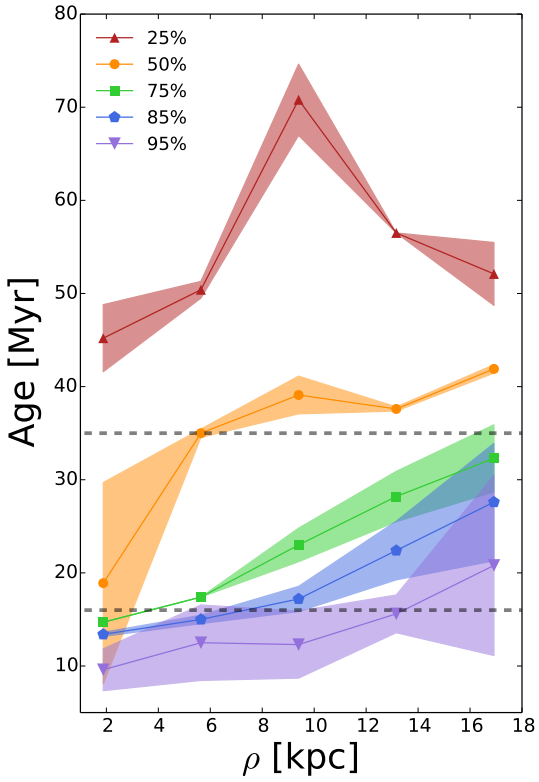

Figure 3.8: The times at which the $25\%, 50\%, 75\%, 85\%$ and 95% stellar mass fractions are reached as a function of radius. 1σ error bars are represented by the shaded regions. The horizontal lines indicate the stellar population ages that contribute 99.9% of the Hα (16 Myr) and 80% of the FUV (35 Myr) photons (Gogarten et al., 2009).

proportion of stars that are younger. By definition, 100% of the stars are older than 4 Myr (our youngest isochrone), and similarly, 100% of the stars are younger than 100 Myr. Figure 3.7 shows that the epoch of star formation occurring between $50-100$ Myr ago roughly accounts for $20\% - 25\%$ of the 100 Myr stellar mass fraction. For more recent times, we find that for a fixed age, the outer radii exhibit larger mass fractions than the inner radii, suggesting the mean stellar age increases with radius.

To better demonstrate this trend, we determine the age at which the $25\%, 50\%, 75\%, 85\%,$ and 95% mass fraction are attained for each cumulative SFH (Figure 3.8). With the exception of the annulus at $5'$ ($\rho \approx 9.5$ kpc), the age-radius relation for the 25% mass fraction is relatively flat, with each annulus achieving 25% around 50 Myr ago. The

Table 3.1. Best-Fit Exponential Scale Lengths

Time Frame	Scale Length (kpc)	Filter	Scale Length (kpc)
< 10 Myr	4.65 ± 0.21	Hα	4.93 ± 0.60
< 35 Myr	6.38 ± 0.26	FUV	6.32 ± 0.34
< 100 Myr	6.30 ± 0.15	NUV	6.63 ± 0.43

$50\%, 75\%, 85\%$, and 95% age-radius relations increase in age by approximately 10 Myr over the 17 kpc radial extent. Spectral synthesis models of Hα, FUV, and NUV emission as a function of age indicate that 99.9% of the Hα photons, and 55% of the UV photons, are emitted by stellar populations < 16 Myr old (Gogarten et al., 2009). From Figure 3.8, we find that the fraction of stars that are < 16 Myr old is $15\% - 35\%$ in the inner radii compared to $< 5\%$ at 17 kpc. For comparison, stars < 35 Myr old account for $\gtrsim 50\%$ in the inner regions and $\sim 25\%$ at 17 kpc. Thus, the data are consistent with a stellar age gradient tending towards older stars in the outer disk. If we assume that the observed trends in the SFH persist beyond 17 kpc, the fraction of stars < 10 Myr old is unlikely to be sufficient to produce significant Hα emission. Therefore, the dearth of Hα emission at large radii may be attributed to an increase in the mean stellar age with radius.

While our data are consistent with an age gradient, we must consider the possiblity that stochastic effects due to the statistical sampling of the IMF, or a high mass truncation in the IMF, are resulting in the observed trends. The data clearly indicate a radial gradient in the maximum stellar mass that has been interpreted as a gradient in stellar age: an interpretation that hinges upon the assumption of an invariant IMF. If the IMF were statistically sampled such that high mass stars were less likely to form in regions of low SFR, or in low density regions there existed a rigid upper mass limit above which stars could not form, the lack of high mass stars could be incorrectly interpreted as older stellar populations. As a result, our data are consistent with a radial age gradient that is sufficient to explain the discrepancies between the Hα and UV radial emission profiles, however, we cannot conclusively eliminate alternative explanations.

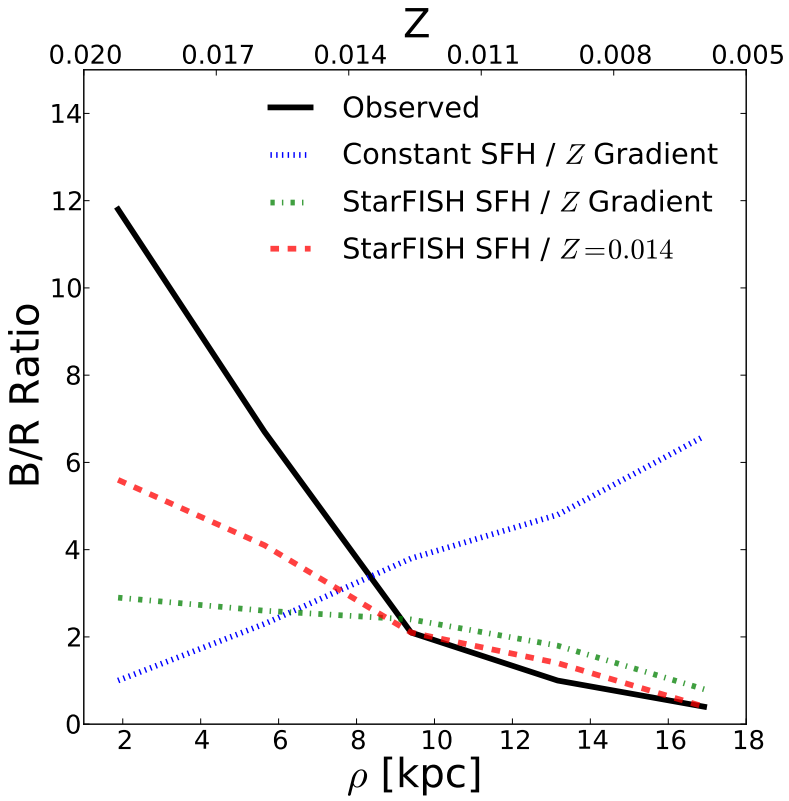

Figure 3.9: Modeled blue-to-red supergiant ratios. Model CMDs were drawn from a constant SFH with the observed metallicity gradient (dotted), the derived SFH and a metallicity gradient (dot dashed), and the derived SFH and no metallicity gradient (dashed). The observed blue-to-red supergiant ratio is given as a solid line.

3.4.3 Modeling the Blue-to-Red Supergiant Ratio

The main candidates for the determination of the B/R ratio are population age, metallicity, and stellar rotation (see Meynet et al. (2011) and references therein). Observations dictate that the B/R ratio is an increasing function with metallicity (see Eggenberger et al. (2002) and references therein). It has also been shown that the B/R ratio sensitive to stellar population age (Dohm-Palmer & Skillman, 2002; Vázquez et al., 2007; McQuinn et al., 2011) and the shape of the B/R ratio as a function of age is adequately modeled using non-rotating stellar isochrones for low metallicities ($Z < 0.009$). In Paper I, we show that the B/R ratio decreases with radius and decreasing metallicity. As

we have demonstrated in the above sections, the stellar populations in M101 increase in age with radius. Given the dependence of the B/R ratio on SFH, and the fact that there is no publically available set of rotating isochrones which span the range of metallicities in M101, the goal of this section is to use non-rotating stellar isochrones to model the B/R ratio in each annulus, including the effects of the SFH and metallicity gradient. To do so, we: i) identify blue and red supergiants in our observed CMDs, ii) examine how our selection criteria affect the predicted B/R ratios and their variation with age and metallicity, and iii) model the B/R ratio in each annulus.

In Paper I, we identified blue and red supergiants using color-color and color-magnitude criteria with a limiting absolute magnitude of $M_V < -5$. Binning the stars into three luminosity bins, we found that the B/R ratio was a decreasing function with radius, dropping by nearly a factor of 15 in all three lumninosity bins. For this study, we determine the B/R ratio in each annulus, for all stars brighter than $M_V = -5$. In Figure 3.9, we show the observed B/R ratio as a function of radius and find a similar trend to that in Paper I.

Next, we examine how the B/R ratios are expected to vary with age and metallicity when identified using our selection criteria. We created synthetic single-age CMDs from the Padova stellar isochrones (Marigo et al., 2008) for the metallicities between $0.005 - 0.020$. Each CMD includes ~ 200000 stars drawn from an IMF with slope -2.35 (Salpeter, 1955). From each synthetic CMD, we photometrically identify blue and red supergiants using the selection criteria given in Paper I. Our absolute magnitude cutoff of $M_V < -5$ corresponds to an age cutoff of ~ 40 Myr (Marigo et al., 2008), therefore we calculate the B/R ratio for ages < 40 Myr old. In our calculation, the youngest age at which the B/R ratio is calculable is set by the upper luminosity limit for red supergiants, which corresponds to an upper mass limit of $\sim 40 - 50$ $M_\odot$ (Humphreys & Davidson, 1979; Humphreys & Davidson, 1994). We show the relationship between B/R ratio and age for all six metallicities in Figure 3.10. We find that our selection criteria result in a B/R ratio that is initially very large (> 30) followed by a precipitous decline, analogous to the age dependence of the B/R ratio shown in Vázquez et al. (2007). Furthermore, the age at which the red supergiants first appear on the CMD is metallicity dependent, with red supergiants appearing as early as 7 Myr for $Z = 0.020$, and as late as 10 Myr for $Z = 0.005$ (one may equivalently interpret this as the upper

mass limit at which red supergiants may exist increasing with metallicity). While red supergiants appear earlier in high metallicity isochrones, the low metallicity isochrones predict, on average, higher B/R ratios for ages > 10 Myr.

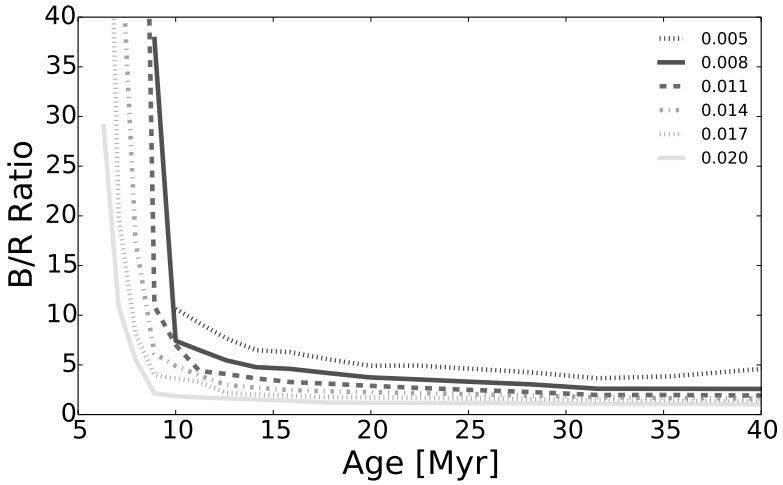

Figure 3.10: B/R ratio versus age for metallicities between $Z = 0.005$ and $Z = 0.020$. Blue and red supergiants were identified using the selection criteria from Paper I. The youngest age at which the B/R ratio is calculable is when red supergiants first appear on the CMD. Red supergiants appear as early as 7 Myr for $Z = 0.020$, and as late as 10 Myr for $Z = 0.005$. One may equivalently interpret this as the upper mass limit at which red supergiants may exist increasing with metallicity.

To test the likelihood that variations in the SFH with radius are responsible for the change in the B/R ratio with radius, we model the B/R ratio under three conditions: i) a constant SFH and observed metallicity gradient, ii) the derived SFH and constant metallicity, and iii) the derived SFH and observed metallicity gradient. To model the B/R ratio, we created model CMDs, of a single metallicity, for each annulus as the linear combination of single-age CMDs. The number of stars in the model CMD contributed by each single age CMD was determined by the SFR multiplied by width of the time bin and divided by the average mass. From our modeled CMDs, we identified blue and red supergiants more luminous than $M_V = -5$ using the selection criteria from Paper I. In Figure 3.9, we display the predicted B/R ratios and their dependence on radius for all three conditions. Additionally, we display the metallicity gradient in M101 (Kennicutt et al., 2003) as the second x-axis on Figure 3.9.

In our first condition, we created synthetic CMDs assuming a constant SFH over the last 100 Myr as well as the metallicity gradient from Kennicutt et al. (2003) (dotted line). After selecting blue and red supergiants from the synthetic CMDs, we plot the B/R ratio as a function of radius. We find that using a constant SFH, the B/R ratio is an increasing function with radius and increases with decreasing metallicity. This scenario illustrates the inability of current stellar evolution models to match observations.

In our second condition, we remove the metallicity gradient by calculating the B/R ratios in each annulus assuming $Z = 0.014$. In our calculation, we take the derived SFH into account. This condition allows us to illustrate the effect that the observed age gradient has on the predicted B/R ratios in a single metallicity environment. Figure 3.9 indicates that the radial B/R ratio trend is reversed in the presence of the apparent age gradient and the absence of the metallicity gradient (dashed line) which is unsurprising based on how the B/R ratio is expected to depend on age and metallicity (Figure 3.10). We find that for radii greater than 9 kpc, the modeled and observed B/R ratios are in good agreement; whereas inside 9 kpc they differ by as much as a factor of 2. While the agreement is interesting, M101 is not a single metallicity environment and so we must include the metallicity gradient to properly model the B/R ratio in each annulus.

Lastly, in our third condition, we created synthetic CMDs assuming the best-fit SFH as well as the metallicity gradient. With the addition of metallicity gradient, we find that the modeled B/R ratio trend (dot-dashed line) is considerably shallower than observations and at large radii (low metallicity), the models predict B/R ratios that are larger than observations by $\lesssim 2$. Studies of the B/R ratios in low metallicity galaxies have found similar agreement between model predictions and observations (Dohm-Palmer & Skillman, 2002; Úbeda et al., 2007; McQuinn et al., 2011). The largest discrepancies occur at small radii (high metallicity) where we find that the observed ratios are greater than the models predict by a factor of approximately 4. At high metallicity, the non-rotating models predict much lower B/R ratios than the observations dictate and only after adding in stellar rotation do the models and observations agree (Vázquez et al., 2007). Thus, the observed discrepancies between our modeled and observed B/R ratios may be primarily due to our use of non-rotating stellar isochrones. However, at this time, we cannot incorporate rotation into our modeled B/R ratios since there are no published rotating isochrones which span the metallicity range in M101.

3.5 Summary and Future Work

In this paper, we use 16 archival *HST*/ACS fields to determine the radial SFH of M101 and its influence on the emission properties and stellar populations. We derive the SFH from the resolved stellar populations in five $2'$ wide annuli. Our main conclusions are the following:

1. Binning the SFH into time frames corresponding to stellar populations traced by Hα ($<$ 10 Myr), FUV ($<$ 35 Myr), and NUV ($<$ 100 Myr) emission, we determined radial SFR profiles. We fit exponential functions to the radial SFR profiles and compared them to the radial emission profiles themselves. We find that radial SFR profiles and the radial emission profiles have best-fit scale lengths that are in excellent agreement. Our results showed that the $<$ 35 Myr radial SFR profile is considerably more extended than that of the $<$ 10 Myr radial SFR profile. Examining the age at which the $50\%, 75\%, 85\%$, and 95% mass fractions are attained, we find that the mass fraction for stars $<$ 16 Myr old is $15\% - 35\%$ in the inner regions, compared to less than 5% in the outer regions. The mass fraction for stars $<$ 35 Myr old is greater than 50% in the inner regions and greater than 25% in the outer regions. These findings are consistent with a radially increasing stellar age gradient which provides a natural explanation for the lack of Hα emission at large radius. However, our data cannot rule out alternative explanations such as statitical sampling of the IMF or a strongly truncated IMF.

2. We model the B/R ratio in our five annuli, examine the effects that a metallicity gradient and variable SFH have on the predicted ratios, and compare to the observed values. Holding the SFH constant, the predicted B/R ratios decrease with metallicity, a trend which is opposite to observations. Including the radially variable SFH, the radial behavior of the B/R ratio mimics that of the observed values. Moreover, we find that our modeled B/R ratios closely match the observed values at large radii (low metallicity) but are discrepant at small radii (high metallicity), which we attribute to our use of non-rotating stellar isochrones.

This is the second paper in a series on the massive star population in M101. Paper III will be a spectroscopic survey of the most luminous stars and their variability from the

multi-epoch, multi-color imaging survey using the Large Binocular Telescope (Kochanek et al., 2008).

3.6 Acknowledgments

Our research on massive stars is supported by the National Science Foundation AST-1109394 (R. Humphreys, P.I.). All of the data presented in this paper were obtained from the Mikulski Archive for Space Telescopes (MAST). STScI is operated by the Association of Universities for Research in Astronomy, Inc., under NASA contract NAS5-26555. Support for MAST for non-HST data is provided by the NASA Office of Space Science via grant NNX09AF08G and by other grants and contracts. We thank the anonymous referee for a careful reading and detailed report which helped to improve this paper signicantly.

Chapter 4

The Photometric Variability and Spectroscopy of the Most Luminous Stars (Grammer et al., 2014)

Abstract

We present moderate-resolution optical spectra for 50 of the brightest stars in the direction to M101 as well as light curves for stars with $V \lesssim 20.5$ from the multi-epoch $UBVR$ images from the Large Binocular Telescope. We separate the spectroscopially confirmed members of M101 into four groups: hot supergiants, intermediate supergiants, emission-line stars, and LBVs. Several stars in each group are discussed in detail. Of the spectroscopically confirmed members, we find that eight meet our criterion for variability. Based on the spectra and light curves, we present new light curves for the known LBV V2 and identify three new LBV candidates: 9492_14_11998, V4, and V9. Additionally, we identify 20 new variables in M101. Lacking spectra, we separated the variables, by their photometric properties, into three groups: hot, intermediate, and cool. We find two hot stars with V-band variability of ± 1 magnitude; we flag these stars as LBV candidates.

Of the intermediate and cool variables, we identify several stars with low- to moderate-amplitude variability with amplitudes of $0.1 - 0.5$ magnitudes.

4.1 Introduction

The classical or normal LBVs are observationally identified as luminous and hot stars that exhibit significant photometric and spectroscopic variability. During quiescence, the spectrum of an LBV is similar to a B-type supergiant or Of/late-WN star. In most cases, LBVs undergo "eruptions" which are characterized by photometric variability of $1 - 2$ magnitudes and significantly enhanced mass loss rates (Humphreys & Davidson, 1994; Vink, 2012). The increased mass loss rates result in the development of an optically thick, pseudo-photosphere with an apparent spectral type of A to F (T_{eff} ~7000 K). As a result, the visual luminosity of the star increases, although the bolometric luminosity remains unchanged (Humphreys & Davidson, 1994). The time-scale for these eruptions is between 10-40 years with the minima and maxima lasting several years.

Very rarely, LBVs display extreme outbursts similar to the giant eruptions of η Car and P-Cygni. These objects have been called giant eruption LBVs (Humphreys & Davidson, 1994), η Car variables (Humphreys et al., 1999), and η Car analogs (Van Dyk, 2005). These giant eruptions have luminosities that approach the lower limit for true supernovae ($M_V \approx -14$) and have spectroscopic features similar to Type IIn supernovae which presumably arise from the strong interaction between the ejecta and the circumstellar medium from prior mass loss episodes (Turatto et al., 1993). As a result, these giant eruptions are often mis-classified as true supernovae. However, the temporal evolution of their photometric and spectroscopic properties reveal that they are sub-luminous and their spectra do not evolve into true supernovae. The discovery of these events has lead to their description as "supernova impostors" (Van Dyk & Matheson (2012) and references therein).

Recently, supernova surveys have lead to the identification of an increasing number of these non-terminal optical transients with a wide range of properties. Some of these optical transients appear to be similar to the giant eruptions of the η Car variables, while others are more akin to the variability of normal LBVs. A very small fraction of the optical transients originate from lower luminosity, heavily obscured progenitors that

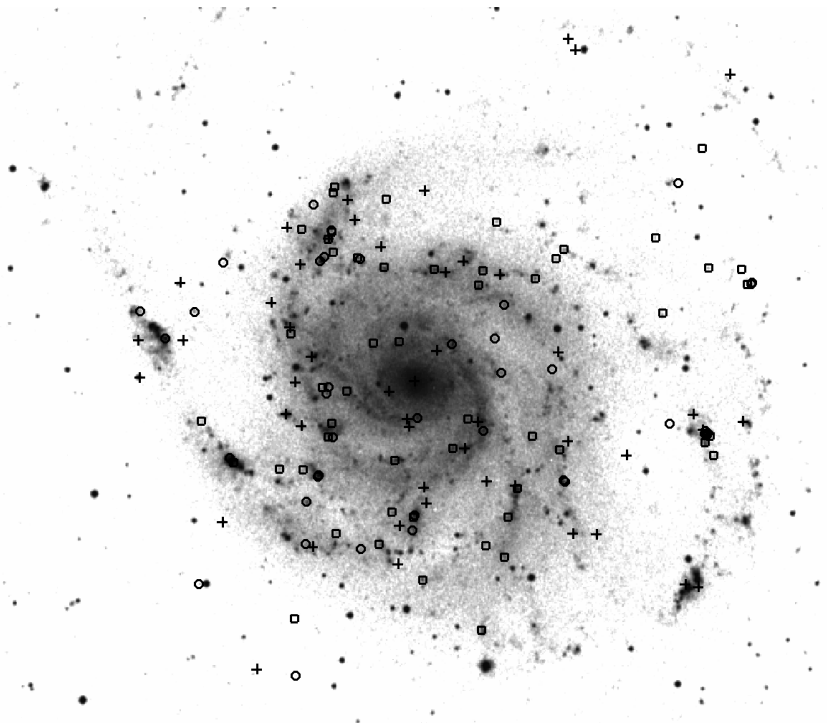

Figure 4.1: POSS II red image of M101. Spectroscopic targets observed with MMT/Hectospec are shown as crosses and LBT/MODS as boxes. Targets without spectra are shown as circles.

may be extreme asymptotic giant branch (AGB) stars or in a post red supergiant stage of evolution (Thompson et al., 2009; Khan et al., 2010; Bond, 2011). The continued monitoring of these optical transients has led to the realization that in some cases the apparent terminal explosion is preceded by smaller eruptions, e.g. SN2005gl (Gal-Yam et al., 2007; Gal-Yam & Leonard, 2009), SN2006jc (Pastorello et al., 2007) and most recently the peculiar SN2009ip (Mauerhan et al., 2013; Pastorello et al., 2013; Fraser et al., 2013; Margutti et al., 2013). Consequently, the connection between LBVs, giant eruptions, and true supernovae has come into question.

Due to the extreme rarity of the giant eruption LBVs, very little is known about their progenitors and and evolutionary state. To shed light on the nature of these rare stars and evolutionary states, an improved census of the most massive, evolved stars is necessary. Given their rarity, the number of known LBVs and hypergiants is very small. Thus, our understanding of the late stages of stellar evolution is greatly hindered

by small number statistics. The work presented here is part of a larger survey of the evolved massive star populations in nearby galaxies (Humphreys et al., 2013; Grammer & Humphreys, 2013; Humphreys et al., 2014).

This paper is the third in a series on the massive star content in M101. In the first two papers, we presented the photometric analysis and identification of the luminous and massive star populations, here we present multi-epoch imaging and spectroscopy for the most luminous stars. In the next section, we describe our target selection, observations, and data reduction. In §3 we discuss the targets for which have spectra and light curves. In §4, we discuss the light curves for targets that do not have spectra. The final section will summarize our conclusions

4.2 Data and Observations

4.2.1 Target Selection

The targets for our spectroscopic and variability study were selected from two sources. The majority were selected from the Hubble Legacy Archive (HLA) aperture photometry of *HST*/ACS images; specifically images from the proposal identification numbers 9490 (Nov. 2002) and 9492 (Jan. 2003). From the HLA photometry, we selected sources that were brighter than $V \approx 20.5$. Since the images of M101 are crowded, particularly in the spiral arms, we later performed our own photometry using Dolphot (Dolphin, 2000) to create a catalog of high precision photometry even in crowded regions (Grammer & Humphreys, 2013, hereafter Paper I). We refer to photometry from Paper I as the catalog photometry. We cross-identified targets selected from the HLA with the catalog using a tolerance of $0.1''$ in radial separation. We note that a few of the targets with $V < 20.5$ in the HLA photometry are much fainter in the catalog. The targets with differences in V larger than a few tenths of a magnitude are in regions where aperture photometry is inappropriate (e.g. crowded regions). We visually inspected the surrounding region of each unmatched target and found that all cases, the unmatched targets were located in parts of the galaxy where photometry was likely to be highly compromised.

In addition to the targets selected from *HST*/ACS photometry, we included blue supergiants and known luminous variables from Sandage & Tammann (1974) and Sandage

Table 4.1. Members of M101

Catalog ID	Star ID	α_{J2000}	δ_{J2000}	V	$(B-V)$	Group	Variability	A_V	Comments
J140220.98+542004.38	9492_14_11998	14:02:20.98	54:20:04.38	19.40	0.19	LBV Cand.	BVR	$0.6-1.4$	Be; P-Cyg H, He I; Fe II em.; crowded
J140227.30+541952.50	9492_14_8847	14:02:27.30	54:19:52.50	19.69	0.38	Im. SG	BVR	0.2	F5 I
—	B4	14:02:27.89	54:16:18.43	—	—	Em. Line	—	—	Em. Line; H II region
J140228.83+542014.03	9492_14_14450	14:02:28.83	54:20:14.03	19.74	0.34	Im. SG	$UBVR$	0.9	Early A I; Fe II, weak [Fe II] em.
—	V9	14:02:29.92	54:16:19.91	—	—	LBV Cand.	$UBVR$	—	See text
J140248.46+541935.80	9490_c2_14120	14:02:48.46	54:19:35.80	20.10	0.19	Im. SG	—	$0.2-0.3$	Late A I
J140256.71+541834.09	9490_02_152	14:02:56.71	54:18:34.09	20.30	0.20	Im. SG	—	0.3	A5 I
J140259.37+542323.89	9490_a3_10940	14:02:59.37	54:23:23.89	21.49	-0.06	Em. Line	—	$0.6-0.7$	Of/WN; N III, He I & II, O II em.
J140301.84+541949.62	9490_02_991	14:03:01.84	54:19:49.62	20.17	0.00	Hot SG	—	0.4	B3 I
J140302.61+542001.39	9490_02_1239	14:03:02.61	54:20:01.28	20.02	0.20	Im. SG	—	≈ 0	Early A I; comp.
J140304.70+541925.00	9490_02_598	14:03:04.70	54:19:25.00	20.07	0.30	Hot SG	—	1.7	B0 I; P-Cyg H, He I; Fe II and [Fe II] em.; strong WN feature
J140305.13+542342.14	9490_a3_14757	14:03:05.13	54:23:42.14	20.32	-0.03	Hot SG	—	0.3	B3 I; weak WN feature; comp. spectrum
J140307.95+542326.81	9490_a3_11594	14:03:07.95	54:23:26.81	21.51	0.06	Hot SG	—	0.6	B3 I; weak WN feature; H and [Fe II] em.
J140309.19+542138.77	9490_01_6951	14:03:09.19	54:21:38.77	19.96	0.09	Hot SG	—	0.3	B9 I; weak WN feature; comp. spectrum
J140311.06+541830.96	9490_a2_20839	14:03:11.06	54:18:30.96	19.95	0.33	Im. SG	V	0.7	A5 I
J140311.32+542518.55	9490_03_6943	14:03:11.32	54:25:18.55	20.18	0.11	Im. SG	—	0.2	A2 I; comp. spectrum
J140313.44+541954.44	9490_02_1086	14:03:13.44	54:19:54.44	19.90	-0.02	Hot SG	—	0.2	B5 I; H em.
J140313.74+542004.56	9490_02_1340	14:03:13.74	54:20:04.56	20.11	0.28	Im. SG	—	0.3	F0 I; H em.
J140314.80+541737.93	B162	14:03:14.80	54:17:37.93	19.52	0.09	Hot SG	—	0.5	B5 I; P-Cyg Hα em.
J140314.98+541645.26	V4	14:03:14.98	54:16:45.26	22.02	0.05	LBV Cand.	$UBVR$	—	See text
J140316.64+542042.04	9490_01_3663	14:03:16.64	54:20:42.04	21.99	-0.05	Hot SG	—	0.1	B5 I
J140322.26+542437.69	9490_03_5290	14:03:22.27	54:24:37.62	19.98	0.42	Im. SG	—	0.9	A8 I
J140323.43+542504.84	9490_03_6537	14:03:23.44	54:25:04.76	20.37	0.51	Im. SG	—	1.2	Late A I; comp. spectrum
J140326.37+542411.63	9490_03_3806	14:03:26.37	54:24:11.63	20.22	0.13	Hot SG	—	$0.6-0.9$	Early B I; weak WN feature; He I λ4471 em.
J140328.35+541707.58	9490_a1_416	14:03:28.35	54:17:07.58	19.90	1.00	Im. SG	—	$0.4-1.0$	Late F I
J140328.86+542128.94	9490_01_6401	14:03:28.86	54:21:28.94	19.91	0.70	Im. SG	—	$1.5-1.7$	Late A I
J140330.73+542335.77	9490_03_1487	14:03:30.73	54:23:35.66	19.86	0.58	Im. SG	—	1.4	A5 I
—	9490_01_8757	14:03:32.28	54:22:09.19	—	—	Im. SG	V	—	Late F I
J140332.78+542009.89	9490_a1_7093	14:03:32.78	54:20:09.89	20.20	0.31	Hot SG	—	$1.2-1.6$	Early B I; WN feature; P-Cyg He I; Fe II & [Fe II] em.
J140332.88+542425.99	V2	14:03:32.88	54:24:25.99	20.69	0.13	LBV Cand.	$UBVR$	—	See text
J140341.18+541905.30	9490_b1_3762	14:03:41.18	54:19:05.30	22.13	0.23	Em. Line	—	—	Strong WN feature; H, He I, Fe II, [Fe III], C III & IV, N II em.

Note. — Spectroscopic targets observed with Hectospec on the MMT. Units of right ascension are hours, minutes, and seconds; units of declination are degrees, minutes, and seconds. Sources are sorted by increasing RA. The V and $(B-V)$ magnitudes are from the Grammer & Humphreys (2013) catalog. The Variability column denotes the bands in which the target meets our variability criteria. The total extinction towards each target is estimated based on the difference between observed and intrinsic color.

Table 4.2. Foreground Stars

Catalog ID	Star ID	α_{J2000}	δ_{J2000}	V	$(B-V)$	Variability	Spectral Type
—	9492_12_5654	14:02:23.33	54:28:01.68	—	—	UB	M4 V
—	9490_c2_12822	14:02:39.23	54:19:16.83	—	—	$UBVR$	K7 V
J140243.90+541727.85	B53	14:02:43.90	54:17:27.85	21.30	0.58	—	F0-F2 III
J140247.62+541728.90	9490_c2_1281	14:02:47.62	54:17:28.90	19.87	0.43	—	Late-A
J140247.76+542833.56	9492_09_25840	14:02:47.76	54:28:33.56	19.91	0.57	U	F8 III/V
—	9492_09_27729	14:02:48.88	54:28:48.76	—	—	$UBVR$	M2 V
J140250.09+542138.09	9490_02_2795	14:02:50.09	54:21:38.05	20.11	0.76	R	G8 V
J140301.20+541839.71	B65	14:03:01.20	54:18:39.71	18.96	0.31	—	Late A III
J140310.60+541809.18	9490_a2_17826	14:03:10.60	54:18:09.18	22.45	0.47	—	A3 V (WD)
J140312.62+542056.72	9490_01_4552	14:03:12.62	54:20:56.72	19.56	0.34	—	F2 III
J140318.13+542400.97	9490_03_3062	14:03:18.13	54:24:00.97	19.04	0.69	—	G5 V
—	9490_01_4409	14:03:31.38	54:20:53.67	—	—	—	G4 V
J140335.25+542242.89	9490_c1_3304	14:03:35.25	54:22:42.89	22.10	1.60	U	M5 V
—	9490_b2_21	14:03:36.93	54:14:18.72	—	—	—	F8 V
J140342.55+541740.49	9490_a1_1828	14:03:42.55	54:17:40.49	19.03	0.79	BV	F8 V
—	9490_c1_1056	14:03:49.06	54:21:49.73	—	—	BVR	M2 V
—	9490_c1_3679	14:03:49.62	54:23:08.74	—	—	U	M0 V
—	9490_b1_11450	14:03:55.82	54:20:58.20	—	—	—	M4 V
J140356.08+542149.39	9490_c1_1033	14:03:56.08	54:21:49.32	19.08	0.90	B	G8 V

Note. — Spectroscopic targets observed with Hectospec on the MMT. Units of right ascension are hours, minutes, and seconds; units of declination are degrees, minutes, and seconds. Sources are sorted by increasing RA. The *HST*/ACS magnitudes, for recovered sources, are provided.

(1983). The blue supergiants and luminous variables were originally identified by photographic images. Since precise astrometry is required for our study, we used a Sloan Digital Sky Survey (SDSS) g image of M101 to identify the blue supergiants and known variables by eye. Many of the Sandage (1983) targets resided in regions of significant crowding which made positive identification difficult. Thus, we were only able to include 7 stars: B4, B53, B65, B162, V2, V4, and V9.

4.2.2 Multi-Epoch Imaging

M101 has been monitored as part of a variability survey of 25 nearby (< 10 Mpc) galaxies using the twin 8.4m Large Binocular Telescope (LBT) (Kochanek et al., 2008). Between March 2008 and January 2013, M101 was observed using the Large Binocular Camera (LBC) in the R-band with the red-optimized LBC-Red camera while simultaneously cycling through observations in the UBV filters with the blue-optimized LBC-Blue camera (Giallongo et al., 2008). Our collaborator J. Gerke performed the basic data reduction steps including overscan correction, bias subtraction, and flat fielding with the IRAF *MSCRED* package, as well as the subsequent analysis of the images. Though M101 was observed even in sub-optimal conditions, only images with a point spread

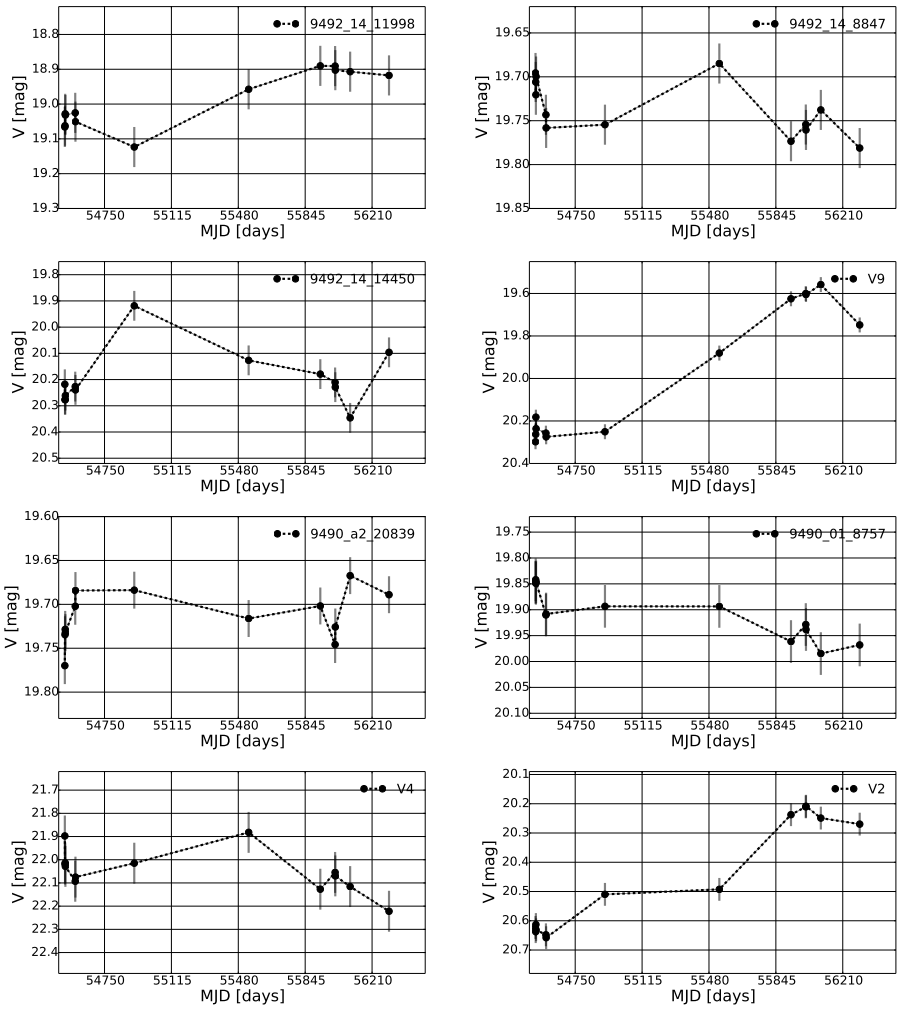

Figure 4.2: Light curves for spectroscopic targets that meet our criterion for variability. Foreground stars are not shown. The x-axis grid lines correspond to 365 days.

function (PSF) with a full width half max (FWHM) $\lesssim 2''$ are analyzed.

For the variability analysis, the ISIS image subtraction package (Lupton, 1998; Alard, 2000) was used to process the multi-epoch LBT images. The image subtraction works by matching a reference image to each epoch and subtracting it to leave only the sources which have time-variable flux. The reference image was created by identifying the epoch with the best seeing and then median combining the exposures of

that epoch. The astrometric solutions were determined using the IRAF package *MSCTPEAK* and SDSS stars (Ivezić et al., 2007) in the FOV. For each epoch, the R-band image serves as the as the astrometric reference image for all four filters which ensures identical astrometric solutions between filters. By doing this, any ambiguity associated with cross-matching sources between filters is minimized. The typical astrometric errors are $0.1''$.

The light curves for the stars with HLA V-band magnitudes $\lesssim$20.5 were extracted using ISIS. Instrumental magnitudes for each epoch were converted to $UBVR$ magnitudes using photometric calibrations based on SDSS photometry which was transformed from the SDSS *ugriz* filter system to the $UBVR$ system using the prescription described by (Jordi et al., 2006). The resulting photometry has photometric errors that are $\lesssim 0.06$ magnitudes. For each target, we calculate the root-mean-square (RMS), with respect to the median magnitude, as a measure of stellar variability. We identify targets as variable sources, for further analysis, if their RMS variability is greater than the median photometric error. The V-band light curves for spectroscopic targets which meet our criterion for variability are displayed in Figure 4.2

4.2.3 Spectroscopy

Our motivation for this study is to examine the spectra and photometric variability of the most luminous stars in M101. Using spectra and light curves, we identify LBVs, hypergiants, and other possible progenitors of the giant eruptions. At the time when we were selecting targets for spectroscopy, we did not yet have LBT light curves for the targets with HLA V-band magnitudes $\lesssim$ 20.5. Since we could not obtain spectra for every target, we prioritized targets for spectroscopy by roughly estimating their variability using an "absdiff" image. The absdiff image was created by taking the absolute value of the difference between the reference image, described above, and all other images. Then, the subtracted images were convolved with a 2 pixel Guassian filter and summed.

In the absdiff image, the "brighter" the source, the more variable it is likely to be. All stars with HLA V-band magnitudes $\lesssim$20.5 were then overlaid onto the absdiff image. Priority for spectroscopy was assigned by degree of variability and V-band magnitude. Thus the brightest stars with clear indications of variability received the highest priority.

We selected 56 of the brightest and most variable targets for spectroscopy with the Multiple Mirror Telescope (MMT), 46 of the fainter targets were selected for spectroscopy with the LBT.

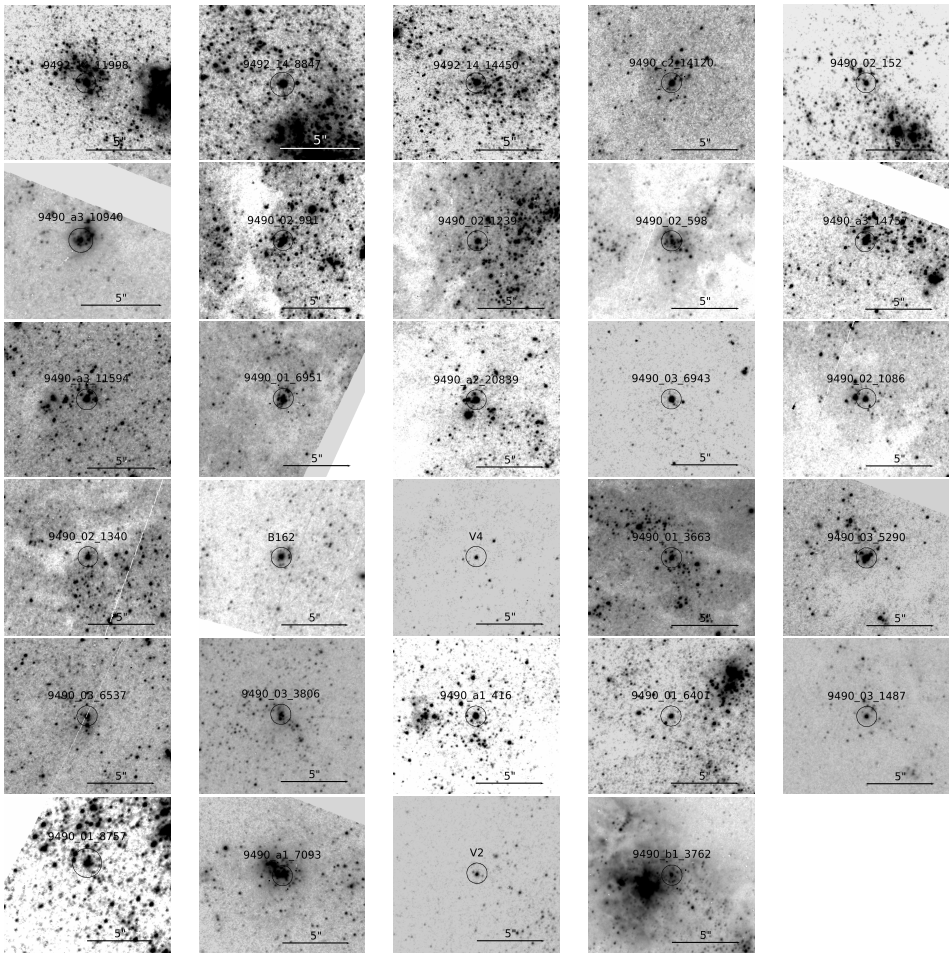

Figure 4.3: *HST*/ACS V images of the confirmed members of M101. The black circles are 1.5″ in diameter and the same size as the Hectospec fibers. The lines at the bottom are 5″ long for scale.

The MMT observations were taken in June 2012 with the Hectospec multi-object spectrometer (MOS; Fabricant et al., 1998). Hectospec[1] is a fiber-fed MOS with a 1° FOV and 300 fibers; each fiber subtends 1.5″ on the sky. We observed each FOV with the 600 mm^{-1} grating with the blue tilt centered on 4800Å and the red tilt centered on 7300Å. Total integrated exposure times are 14400 seconds in the blue and 10800 seconds

in the red. The 600 mm^{-1} grating affords a spectral coverage of $\sim$ 2500Å with 0.54Å $pixel^{-1}$ resolution. The blue and red spectra were reduced using an exported version of the CfA/SAO SPECROAD package for Hectospec data E-SPECROAD[2]. Using E-SPECROAD, we bias subtracted, flat-fielded, wavelength calibrated, and sky subtracted the spectra. The IRAF task `sensfunc`, in the *ONEDSPEC* package, was used to flux calibrate the spectra against the standard Feige-66.

After flux calibration, we continuum rectified the spectra which are shown in Figures 4.4-4.7. We note that only the spectra for our confirmed members of M101 are provided in the paper. We display the spectral range 3800Å to 5500Å since the majority of the important spectral features for our analysis reside in this wavelength range. As is evident, nearly all of the spectra suffer from nebular contamination. In Table 4.2.1 we provide identifiers, astrometry, single epoch photometry, and spectral types for our Hectospec targets that are confirmed members; the foreground stars are in Table 4.2.1.

The 46 stars assigned to LBT observations were observed using the Multiple Object Dual Spectrograph (MODS) (Pogge et al., 2006). MODS has a 6.5′ FOV, a spectral range of 3200Å to 10000Å, and moderate resolution (R $\sim$ 1800). Since the MODS FOV is considerably smaller than Hectospec, four masks were required to cover the disk of M101. The 46 stars were then assigned to one of the four fields. The LBT observations were taken in May 2012 and June 2013. Unfortunately, problems with the reduction pipeline has prevented us from including the LBT spectra in our analysis. A future paper will provide the analysis of the LBT/MODS spectra. Identifiers, astrometry, photometry, and MODS field number (for targets observed with LBT) are provided in Table 4.5.

[1] http://www.cfa.harvard.edu/mmti/hectospec.html

[2] External SPECROAD was developed by Juan Cabanela for use on Linux or MacOS X systems outside of CfA. It is available online at http://iparrizar.mnstate.edu.

4.3 Hectospec Targets

In this section we separate the spectra into four groups: hot supergiants, intermediate supergiants, emission line sources, and candidate LBVs. We describe the criteria for membership in each subsection. For each group, we discuss the spectra, photometry, and light curves of the most interesting or representative targets. In Table 4.2.1 we provide identification information, astrometry, photometry, group membership, and some comments regarding the spectra and variability. For reference, we assume a distance modulus, derived from the tip of the red giant branch, of $(m - M)_0$ $= 29.05 \pm 0.06(\text{random}) \pm 0.12(\text{systematic})$ magnitudes (Shappee & Stanek, 2011). The foreground extinction towards M101 is $\text{E}(B - V) = 0.01$ (Schlegel et al., 1998) which corresponds to a visual extinction of $A_V = 0.03$ magnitudes assuming a Galactic extinction law (Cardelli et al., 1989). For stars with spectral types, we estimate the internal extinction by comparing observed colors to the theoretical intrinsic colors of (Flower, 1996, see Table 4.2.1).

4.3.1 Spectral Classification

For the classification of our spectroscopic targets, we assigned spectral types by examining the absorption features in each spectrum, using the Balmer lines when available. For stars with spectral type O−B5, we compared the relative intensities of Si II $\lambda\lambda$4128-4130 to Si III λ4552, He I λ4471 to Mg II λ4481, and He II λ4541 to He I λ4471. Luminosity classes for stars O5−O9 were assigned by comparing the relative intensities of the Si IV $\lambda\lambda$4089-4116 to He I λ4026 and λ4144; the luminosity classes for B0−B5 were assigned based on the relative intensities of Si III λ4552 to He I λ4387, and O II to He I. Since the Si III lines become very weak at around B5, the spectral types of the later B-type stars (B5−B9) were classified by comparing He I λ4471 to Mg II λ4481. The luminosity classes for the later B-type stars were determined by the general widths of lines and the strength of the O II $\lambda\lambda$4070-4076, λ4348, and λ4416.

With the disappearance of the He I lines in the early A stars and the metallic spectrum gaining strength, we used the relative intensities of the Ca II K line to either Hδ or Mg II λ4481 as our primary temperature diagnostic for stars earlier than A7. The stars with spectral types A7−F3 were classified by comparing the neutral metallic

species Ca I λ4226, Fe I λ4383, and Mn I λ4030, in addition to the Ca II K line, to Hδ or Mg II λ 4481. The luminosity classes for stars A0−F3 were determined by comparing the strengths of the Fe II/Ti II blends $\lambda\lambda$4172-4179 and $\lambda\lambda$4395-4400, as well as Fe II λ4233, to the luminosity-insensitive Ca I λ4226 and Fe I λ4383 lines. The transition from early F to later types is characterized by the appearance of molecular absorption by CH $\lambda\lambda$4300 (G-band) which occurs around F3. Thus, for types later between F3−G0, we compared the intensities of the G-band along with the neutral species of Ca I, Fe I, and Mn I, to Hδ to assign spectral types. If Balmer lines were in emission, we resorted to a more qualitative assessment of the strengths of G-band and neutral metallic absorption lines to determine spectral types. We compared Fe II/Ti II blends to Ca I and Fe I lines, in addition to the positive identification of the O I $\lambda\lambda$7774 triplet, to assign luminosity classes.

The transition from G-type stars to early K is marked by the increasing strength of molecular and neutral metallic absorption, and the decreasing strength of the Balmer lines. We classified stars G0−K3 by comparing Ca I λ4226 and Fe I λ4383 to Hγ, and Mg I $\lambda\lambda$5167-5172-5183 to Hβ. When H not in absorption, we used the ratio of Mn I $\lambda\lambda$4032 to Fe I λ4046 to determine the spectral type. Additionally, we qualitatively examined the strengths of the G-band and MgH $\lambda\lambda$5000-5200 absorption bands, however, they were not used as primary temperature criteria since they are known to be sensitive to luminosity. As for the luminosity classes of the later-type stars, we compared Sr II $\lambda\lambda$4077-4216 to the luminosity insensitive lines of Fe I $\lambda\lambda$4046-4064-4072. The molecular absorption bands of CN at $\lambda\lambda$3883 and $\lambda\lambda$4215 were used as secondary indicators of high luminosity.

For stars K3−M0, we compared the intensities of Ca I λ4226 to Fe I λ4383 to determine the spectral type. However, in stars later than M0, the molecular absorption of TiO dominates the morphology of the stellar spectra and so we used the depth of the TiO bands as the primary temperature criterion for stars later than M0. In mid- to late K stars, the strengths of CN and MgH are inversely correlated with luminosity; MgH has a much lower dissociation energy than CN which results in a stronger CN absorption in luminous stars. Therefore, to assess the luminosity of stars K3−M0, we compared the strengths of the MgH and CN bands. Given the strong luminosity dependence of Ca I λ4226, we determined the luminosity of the mid to late M stars by the relative

intensities of Ca I λ4226 to the strength of the TiO bands.

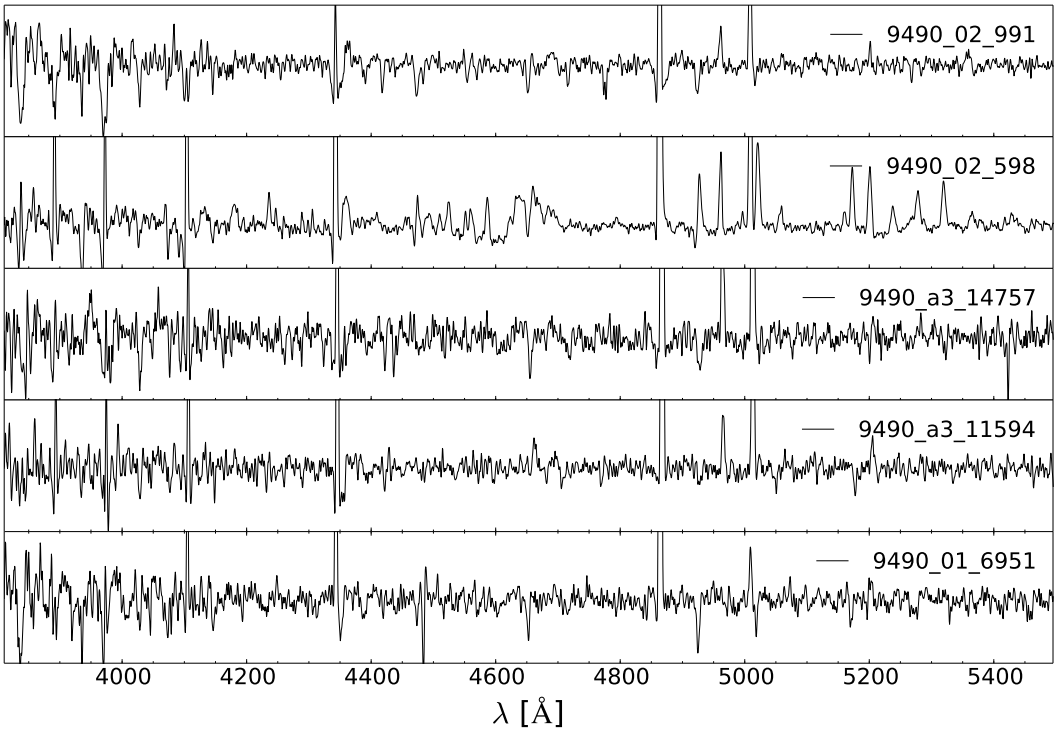

Figure 4.4: Spectra for the hot supergiants. The spectra have been continuum rectified and smoothed to reveal the absorption features. Here we show only the spectral range 3800Å-5500Å to better illustrate the lines used to determine spectral types and luminosity classes.

4.3.2 Hot Supergiants

The hot supergiant group consists of luminous O- and B-type supergiants. To be included in this group, we require the absorption spectrum to be strong enough to make at least an estimate of the spectral type. Many of the stars included have emission as well. In this section we describe targets with interesting spectral features and/or photometric variability.

9490_02_598 (B0 I) – The absorption line spectrum of 9490_02_598 shows strong Si IV $\lambda\lambda$4090-4116, Si III λ4552, C III $\lambda\lambda$4650, and He $\lambda\lambda$4026-4144 absorption indicating it is an early B star (Figure 4.4). The Balmer series, as well as the He I lines beyond

λ4144, are in emission and show strong P-Cygni profiles. Strongly in emission are lines of Fe II, [Fe II], and the broad N III WN feature. The terminal velocity, determined from P-Cygni profiles, is normally done by measuring the blue edge of the absorption component. Because the spectra are moderate resolution and low S/N, we can more reliably determine the wind velocity from the minima. We find a wind velocity of 392.0$\pm$ 12.6 kms^{-1} which on the low end, but in the range for normal early-type supergiants (Crowther et al., 2006; Mokiem et al., 2007).

The catalog photometry for 9490_02_598 is $V = 20.07$ and $(B - V) = 0.30$. Based on the spectrum of 9490_02_598, we would assume an intrinsic color of $(B - V)_0 \approx$ -0.25 (Flower, 1977, 1996). There are many explanations for the differences in color but the most likely is internal extinction. Inspection of the *HST*/ACS V image shows that 9490_02_598 is a point source located in a crowded region. 9490_02_598 was not identified as a point source in the LBT images due to poorer resolution, thus we do not have variability information. The spectrum is strikingly similar to an LBV in quiescence (Humphreys & Davidson, 1994) but without a light curve we cannot say with any certainty that 9490_02_598 is an LBV candidate.

9490_a3_11594 (B3 I) – The spectrum for 9490_a3_11594 is displayed in Figure 4.4. The strength of Si III λ4552, S II $\lambda\lambda$4128-4130 and He I λ4471, λ4009, λ4026, and λ4144 indicate 9490_a3_11594 has a spectral type of roughly B3. The relative strength of the O II $\lambda\lambda$4070-4076 to He I λ4026 indicates high luminosity. The emission lines of 9490_a3_11594 are primarily nebular, however, the H lines show some indication of weak P-Cygni profiles. He I λ4471 and λ5875, and weak Fe II and [Fe II] are also in emission.

The catalog photometry for 9490_a3_11594 is $V = 21.5$ and $(B - V) = 0.06$. We note that HLA and LBT photometry show 9490_a3_11594 to be $\approx$2 magnitudes brighter and $\approx$0.3 magnitudes redder than the catalog photometry. The crowded region in which 9490_a3_11594 is located (Figure 4.3 implies that magnitudes obtained by aperture photometry are significantly affected by the neighboring stars. Thus, we are inclined to trust the catalog magnitudes. Though affected by crowding, the multi-epoch photometry for 9490_a3_11594 display no variability in magnitude or color. 9490_a3_11594 is likely a normal B supergiant.

B162 (B5 I) – B162 was identified as a blue supergiant in M101 by Sandage (1983).

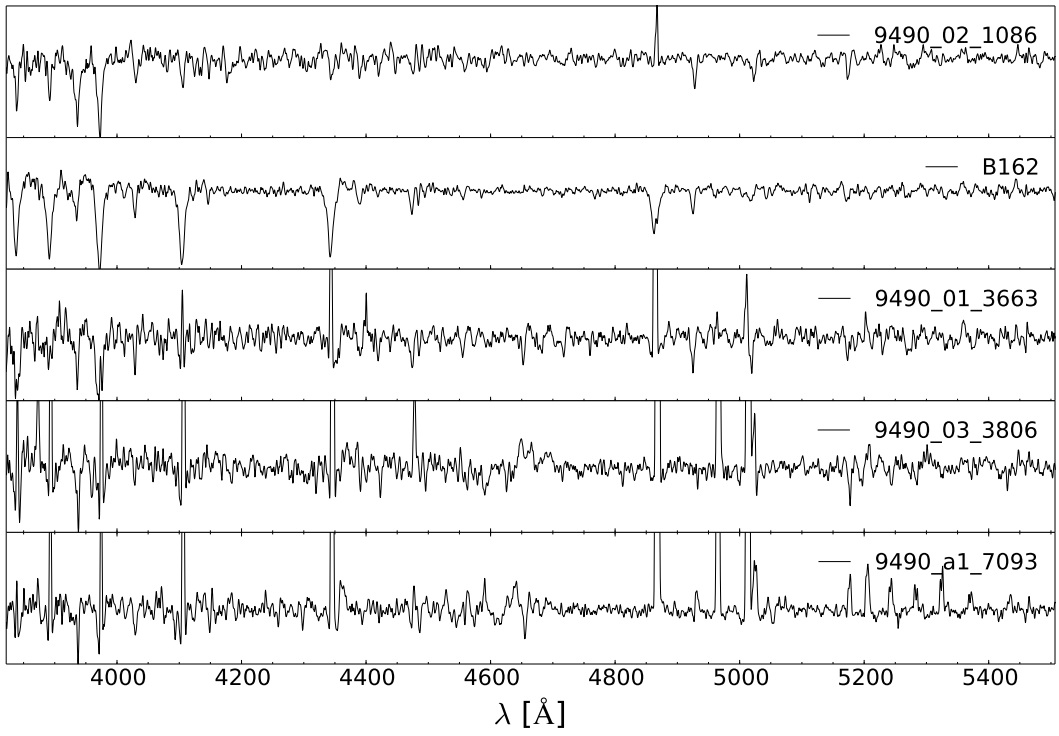

Figure 4.4: (Continued). Same as above.

Followup spectroscopy by Humphreys & Aaronson (1987) confirmed its membership and estimate the spectral type to be late B to early A. Humphreys & Aaronson (1987) mention that B162 may be a composite based on the width of the Balmer lines. Our spectrum of B162 (Figure 4.4) is one of the few without any nebular contamination and based on the ratio of He I λ4471 to Mg II λ4481, we suggest a spectral type of B5; the ratio of Si III λ4552 to He I λ4387, as well as the presence of the high luminosity indicator O I $\lambda\lambda$7774, confirms B162 is a supergiant.

The catalog photometry for B162 indicates it is extremely luminous with a V-band magnitude of $V = 19.52$. As a result, B162 is saturated in the LBT images thus precluding us from assessing its variability; the original discovery of B162 by Sandage (1983) found no evidence for variability, however, their sensitivity was considerably lower. The observed color for B162 is $(B - V) = 0.09$ and is approximately 0.2 magnitudes redder than its spectral type prescribes. Correcting for extinction and using the bolometric correction for a B5 supergiant, we estimate the bolometric magnitude for B162 to be M_{bol} = -10.88, thus placing B162 in the LBV instability strip on the HR diagram (Humphreys & Davidson, 1994; Vink, 2012).

9490_a1_7093 (Early B I) – Many of the absorption features that we would normally use to classify a star of this type are blended with emission lines. Consequently we rely on the strength of the He I lines λ4026, λ4144, and λ4387, as well as Mg II λ4481 to classify 9490_a1_7093 as an early B supergiant. C III and O II are also in absorption and support our classification. Fe II and [Fe II] emission lines, as well as the P-Cygni profiles of He I λ4471 and λ4922, indicate a strong stellar wind. Measuring the wind velocity from the P-Cygni minima, we find a velocity of 323.5 ± 9.2 km s^{-1}.

The catalog color and magnitude for 9490_a1_7093 are $(B-V) = 0.31$ and $V = 20.20$, respectively. 9490_a1_7093 is located in a very crowded region (Figure 4.3) which the lower resolution of the LBT cannot resolve. Consequently, we do not have information on its variability. Since we were unable to assign a precise spectral type to 9490_a1_7093, we compute the likely extinction for early-B spectral types and find that the total extinction to be as little as $A_V = 1.2$ mag and as much as $A_V = 1.7$ mag which is unsurprising given that 9490_a1_7093 is embedded in a region of intense star formation.

The remaining hot supergiants are all typical supergiants with little to no stellar emission, i.e. nebular contamination, and no indication of variability. The catalog

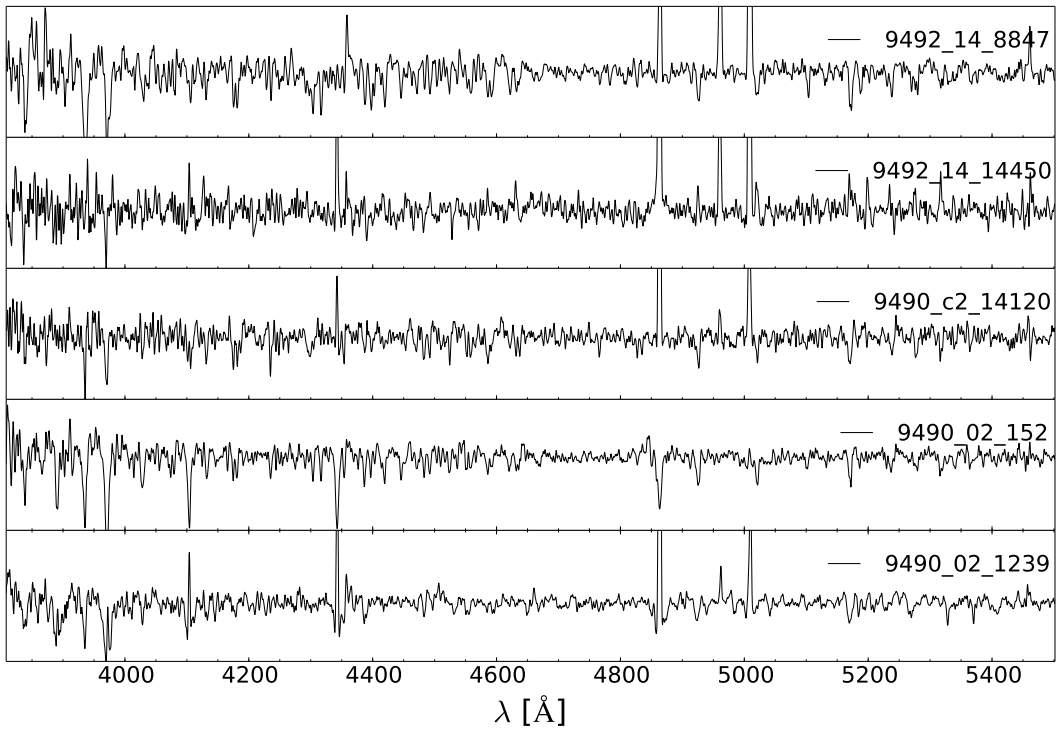

Figure 4.5: Spectra for the intermediate supergiants. The spectra have been continuum rectified and smoothed to reveal the absorption features. Here we show only the spectral range 3800Å-5500Å to better illustrate the lines used to determine spectral types and luminosity classes.

photometry, visual extinction, spectral types, and any other notes regarding the target are given in Table 4.2.1.

4.3.3 Intermediate Supergiants

The intermediate supergiants group includes the visually most luminous A- to F-type stars. The intermediate supergiants, or yellow supergiants, often have strong emission due stellar winds and mass loss. Due to the degree of nebular contamination, none of stars from this group have emission lines that are unequivocally stellar in origin. Here we discuss the more interesting targets in this group, particularly the variables.

9492_14_8847 (F5 I) – The spectrum for 9492_14_8847 is shown in Figure 4.5 and shows its strongest spectral features are the strong Ca II H and K lines as well as the Fe

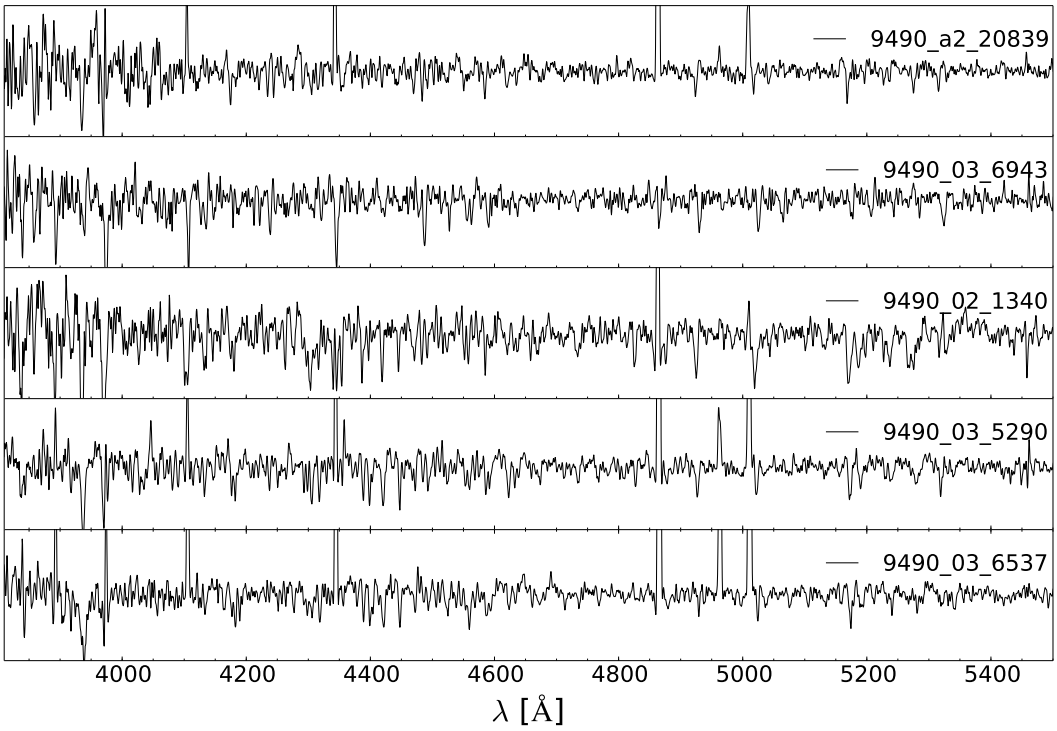

Figure 4.5: (Continued). Same as above.

II/Ti II blend at $\lambda\lambda$4172-4179. The presence of a G-band indicates 9492_14_8847 has a spectral type that is later than ≈F2. We estimate 9492_14_8847 to be approximately F5 by examining the lines of Ca I λ4226, Fe I λ4046 and and 4383 lines, and Mn I $\lambda\lambda$4032; we note that we were not able to use the Balmer lines in our spectral classification due to nebular contamination. The strong singly-ionized Fe and Ti lines at $\lambda\lambda$4172-4179, $\lambda\lambda$4395-4400, λ4417, and λ4444, as well as the Sr λ4078 and λ4215 lines indicate high luminosity.

The V-band light curve for 9492_14_8847 (Figure 4.2) shows only minor variability that is on the order of ≈0.1 magnitudes in amplitude. The catalog photometry for 9492_14_8847 is V = 19.69 and $(B-V)$ = 0.38. The observed color is only marginally redder than expected suggesting 9492_14_8847 is not embedded in dust. Adopting the bolometric correction for an F5 supergiant (BC = 0.18; Flower, 1977, 1996)), the bolometric luminosity of 9492_14_8847 is M_{bol} = -9.18. Furthermore, the *HST*/ACS V image shows that 9492_14_8847 is on the periphery of a star-forming region (Figure 4.3) but appears to be a single point source. Thus, we conclude that 9492_14_8847 is an intermediate supergiant which occupies the same part of the HR diagram as the yellow hypergiants in M31 and M33 (Humphreys et al., 2014).

9492_14_14450 (Early A I) – Figure 4.5 displays the blue side of the spectrum for 9492_14_14450. The relative strength of He I λ4471 to Mg II λ4481, as well as strength of Fe I and Ca I lines, indicates 9492_14_14450 has a spectral type of late B to early A; the low signal-to-noise (S/N) of the spectrum prevents a more refined spectral type. Redward of Hβ, Fe II and [Fe II] lines are in emission. The line profiles for Hβ and Hα have very broad wings that are asymmetric to the red indicating Thompson scattering.

Based on the catalog photometry, 9492_14_14450 had an apparent magnitude of V = 19.74 (M_V = -9.31) and an observed color of $(B-V)$ = 0.34 in January 2003. The multi-epoch photometry from the LBT shows variability on the order of ≈0.4 magnitudes (Figure 4.2) with a maximum of V = 19.95 in March 2009 (MJD 54912). Given that the observed color is much redder than an early-A supergiant and that 9492_14_14450 is located in a very crowded, star forming region, it is likely that there is significant internal extinction. Even without correcting for extinction, 9492_14_14450 is very near the empirical upper luminosity limit on the HR diagram; correcting for extinction will place it above.

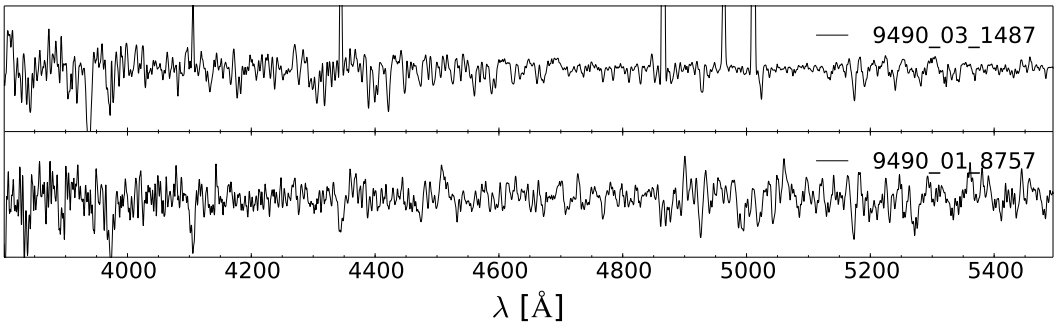

Figure 4.5: (Continued). Same as above.

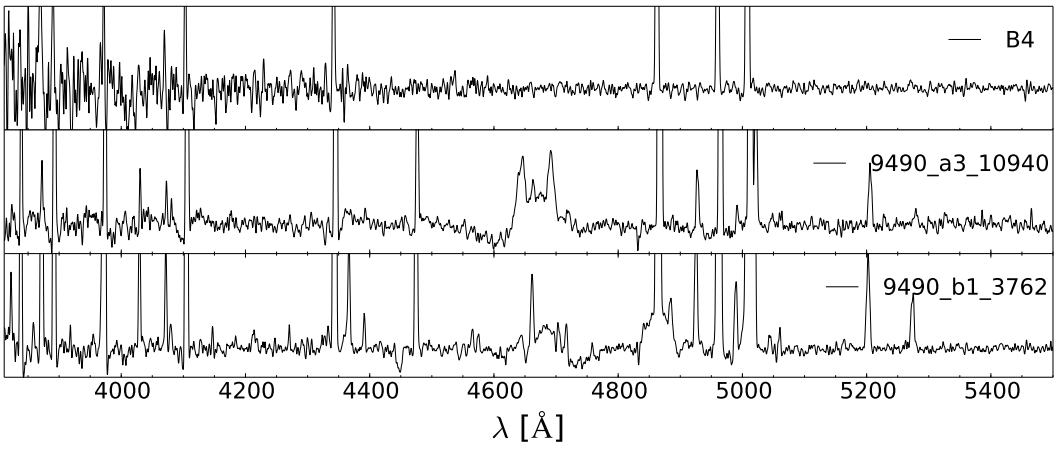

Figure 4.6: Spectra for the emission-line sources. The spectra have been continuum rectified and smoothed. Here we show only the spectral range 3800Å-5500Å.

9490_01_8757 (Late F I) – The spectrum of 9490_01_8757 has low S/N with only the strong metallic lines, G-band, and Balmer lines clearly visible (Figure 4.5). Comparing the Ca I λ4226 and Fe I λ4383 lines to Hδ, we estimate the spectra type to be a late F. The Fe II/Ti II blends are weak but indicate 9490_01_8757 is likely a supergiant. Despite being in apparent isolation (Figure 4.3), we do not find a corresponding catalog source for 9490_01_8757. We speculate that it may be due to the fact that 9490_01_8757 is in close proximity to the ACS chip edge and so the quality of the photometry may have been low. 9490_01_8757 meets our variability criteria in the V-band and its light curve (Figure 4.2) indicates 9490_01_8757 has decreased in brightness by $\approx$0.1 magnitudes.

The catalog photometry, visual extinction, spectral types, and any other notes regarding the remaining intermediate supergiants are given in Table 4.2.1.

4.3.4 Emission-Line Sources

The emission-line group is composed of targets with a blue continuum and strong emission lines. The distinction between targets in this group and the hot supergiants group is the lack of absorption features permitting the estimation of a spectral type. The stars in this group have similar features to the Fe II emission-line stars of M31 and M33 (Humphreys et al., 2014).

9490_a3_10940 (Of/WN) – The spectrum of 9490_a3_10940 is dominated by strong H and He I emission as well as the broad N III feature seen in WN stars (Figure 4.6). Some of the weaker emission lines include He II λ4686, O II $\lambda\lambda$4070-4076, and Fe II. Based on the spectral features, it is likely that 9490_a3_10940 is an Of/WN star. The catalog magnitude for 9490_a3_10940 is $V = 21.49$ which is much fainter than our cutoff of $V \lesssim 20.5$ based on HLA photometry. Inspection of the V-band ACS image (Figure 4.3) shows that 9490_a3_10940 is in a crowded region which has likely skewed the HLA aperture photometry to brighter magnitudes. The observed color of 9490_a3_10940 is $(B - V) = -0.06$ which is approximately 0.2 magnitudes redder than we would expect for a star as hot as 9490_a3_10940. Though we do not have a precise spectral type for 9490_a3_10940, the insensitivity of $(B - V)$ to hot stars allows us to make an estimate of the extinction. Since O-type stars have a $(B - V)$ <-0.25 (Flower, 1977, 1996), the extinction towards 9490_a3_10940 is roughly 0.6-0.7 magnitudes. Correcting for extinction and adopting a bolometric correction of -3.0, we estimate the bolometric luminosity to be $M_{bol} \approx -11.2$.

9490_b1_3762 – The spectrum of 9490_b1_3762 is shown in Figure 4.6. Many of the emission features are nebular owing to the fact that 9490_b1_3762 is located in the giant star-forming complex NGC 5461 (Figure 4.3). Despite the strong nebular contamination, the Hα and Hβ line profiles have very broad wings suggesting a very strong stellar wind. We find He I, C III $\lambda\lambda$4647-4652, and C IV λ4658 absorption lines indicating an underlying hot star. Furthermore, Fe II, [Fe II], and [Fe III] emission lines are present.

9490_b1_3762 is located in a very crowded and nebulous region which, unlike *HST*/ACS,

the LBT cannot resolve. As a result, we cannot asses the photometric variability of 9490_b1_3762 from the LBT. The catalog photometry for 9490_b1_3762 are $V = 22.13$ and $(B - V) = 0.23$. The emission lines from the highly-ionized species we see in the spectrum can only be produced by the radiation field of an OB-type star with $(B-V) < 0$. Since the observed color is much redder than we expect for an OB-type star, it is likely that 9490_b1_3762 is highly reddened or a blend of objects.

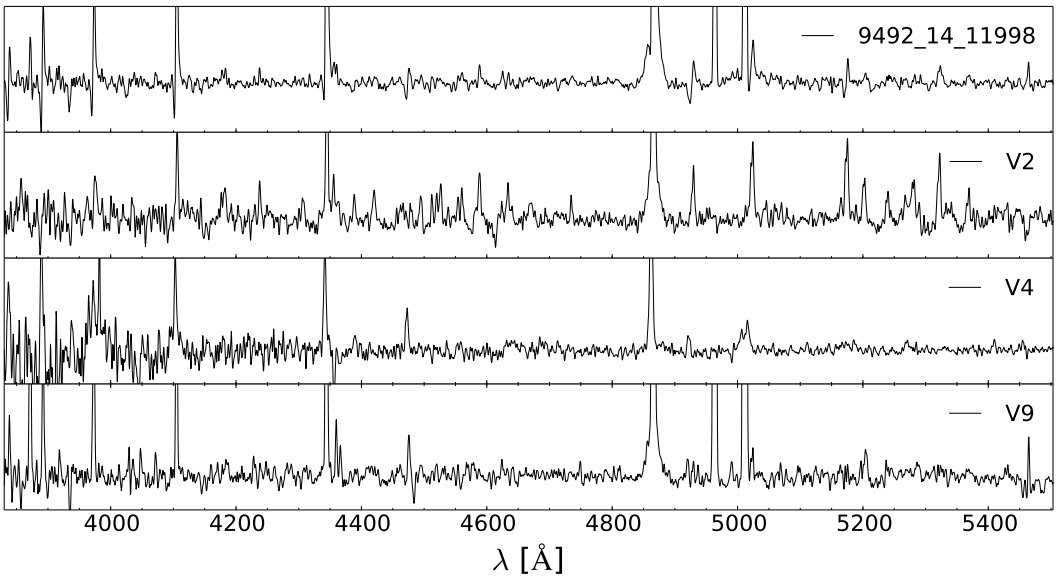

Figure 4.7: Spectra for the LBV candidates. The spectra have been continuum rectified and smoothed. Here we show only the spectral range 3800Å-5500Å.

4.3.5 Candidate LBVs

A census of the irregular blue variables in M101 was first conducted by Sandage & Tammann (1974) which identified nine bright blue variables (V1 - V9). Subsequent photometric studies have confirmed the variable nature of V1 and V2, and added a tenth (V10; Sandage, 1983). Fifty-year historical light curves for the candidate LBVs V1, V2, and V10 are presented in Sandage (1983). V3 through V9 are known to be variable, and are considered to be candiate LBVs, but lack historical light curves. Here we present the light curves and spectra for V2, V4, and V9. In addition, we add a candidate LBV: 9492_14_11998.

9492_14_11998 (Be) – The spectrum of 9492_14_11998 is dominated by He I and Balmer emission lines with strong P-Cygni profiles which can be seen in Figure 4.7. The line profiles of Hα and Hβ have very broad wings and are asymmetric to the red, a feature characteristic of Thompson scattering. While there is some Fe II in emission, the lines are not very strong. From the Balmer and He I lines with P-Cygni profiles, we estimate the wind velocity to be 368.9 ± 9.3 km s^{-1} which is somewhat higher than the wind velocities of the M31 and M33 LBVs (Humphreys et al., 2014) but on the low end for normal OB supergiants (Crowther et al., 2006; Mokiem et al., 2007).

The V-band light curve for 9492_14_11998 is given in Figure 4.2 and shows that the star has steadily increased in brightness by approximately 0.2 magnitudes over the last 4 years. While the eruptive states of LBVs typically involve a change in visual brightness by $1 - 2$ magnitudes, the duration is usually $10 - 40$ years (Humphreys & Davidson, 1994).

The spectrum for 9492_14_11998 was obtained at its current visual maximum. The catalog photometry, which were obtained in January 2003, indicate 9492_14_11998 had an apparent magnitude that is slightly fainter ($V = 19.40$) than its present value. Its observed color in 2003 was $(B - V) = 0.19$ and based on our LBT photometry, has not changed. We note that the observed color is considerably redder than we would expect for a B supergiant, and given the low foreground extinction in the direction to M101, it is likely that the observed color is due to internal extinction.

If we assume an intrinsic color of $(B-V)_0 \approx -0.1$ corresponding to a mid-B (Flower, 1977, 1996) and a Galactic extinction curve, the internal visual extinction is $A_V \approx 0.9$ magnitudes. Correcting the *HST*/ACS visual magnitude for the internal extinction, we find that 9492_14_11998 has an absolute visual magnitude of $M_V = -10.55$ magnitudes. Adopting the bolometric correction (BC) for a mid-B supergiant (BC $\approx$ -1.05; Flower, 1977, 1996), 9492_14_11998 has a bolometric luminosity of M_{bol} = -11.6 which places it well above the empirical upper luminosity boundary. Visual inspection of the *HST*/ACS V image (Figure 4.3) shows that 9492_14_11998 resides in a crowded region which leads us to conclude that the photometry of 9492_14_11998 are likely contaminated by neighboring stars. Despite the uncertainties introduced by crowding, the spectral features of 9492_14_11998 are similar to an LBV in quiescence. Continued monitoring will be necessary to determine whether or not 9492_14_11998 is truly an LBV.

V2 – V2 is one of the three confirmed LBVs in M101 (Sandage, 1983). Humphreys & Aaronson (1987) describe the spectrum as having Hα, Hβ, [O II] λ3727, and Fe II in emission. Our higher resolution and S/N spectrum confirms the described features and reveals broad-winged Hα and Hβ emission lines, as well as [O I], [O II], [N II], [S II], and Fe II in emission. Fe II redward of Hβ, and [O I] and [O II] all have split-emission-line profiles. These characteristics along with the fact that there is no [O III] $\lambda\lambda$4959-5007 in emission suggests the [O I], [O II], [N II], and [S II] lines are originating from the circumstellar environment rather than a nearby H II region. Furthermore, the *HST*/ACS V-band image (Figure 4.3) shows that V2 is essentially in isolation and there is no indication of an H II region within the fiber.

The 50-year historical light curve for V2 is shown in Sandage (1983). Over the 50 years it was monitored, V2 has faded from $V \approx 19.1$ in 1910 to $V \approx 20.3$ in 1960. Our 4.5-year V-band light curve (Figure 4.2) indicates V2 is increasing in brightness from $V = 20.6$ in 2008 to $V = 20.25$. The current spectrum shows V2 to be that of a hot star and, therefore, in quiescence. Followup photometry and spectroscopy will be crucial to monitor its evolution.

V4 – The spectrum of V4 is shown in Figure 4.7 and is fairly noisy despite smoothing with a $\sigma = 1$ Gaussian kernel. The spectrum is primarily composed of strong H, He I, [N II], and [S II] emission lines. Normally in an H II region the [N II] and [S II] emissions lines are accompanied by strong [O II] and [O III]. Since we do not see the strong [O III] $\lambda\lambda$4959-5007 lines, the [N II] and [S II] emissions lines may be produced by the circumstellar medium. The spectrum of V4 also shows Fe II emission throughout, although the lines are not particularly strong.

Though V4 was originally identified as a variable star in M101, Sandage & Tammann (1974) did so by blinking between photographic images. Consequently, there is no historical light curve for V4. The LBT light curve for V4 displays variability with a minimum-to-maximum amplitude of approximately 0.4 magnitudes in the V-band (Figure 4.2). At visual maximum V4 has a V-band magnitude of $V = 21.9$. The catalog photometry from observations taken in 2003 show V4 to be at $V = 22.02$. Sandage & Tammann (1974) list the visual minimum and maximum for V4 to be $V = 22.2$ and $V = 19.9$, respectively. Assuming their photometry to be accurate, V4 is currently at its visual minimum and the oscillations we see are likely the low-amplitude variations

commonly superposed on to the longer time scale LBV minima and maxima.

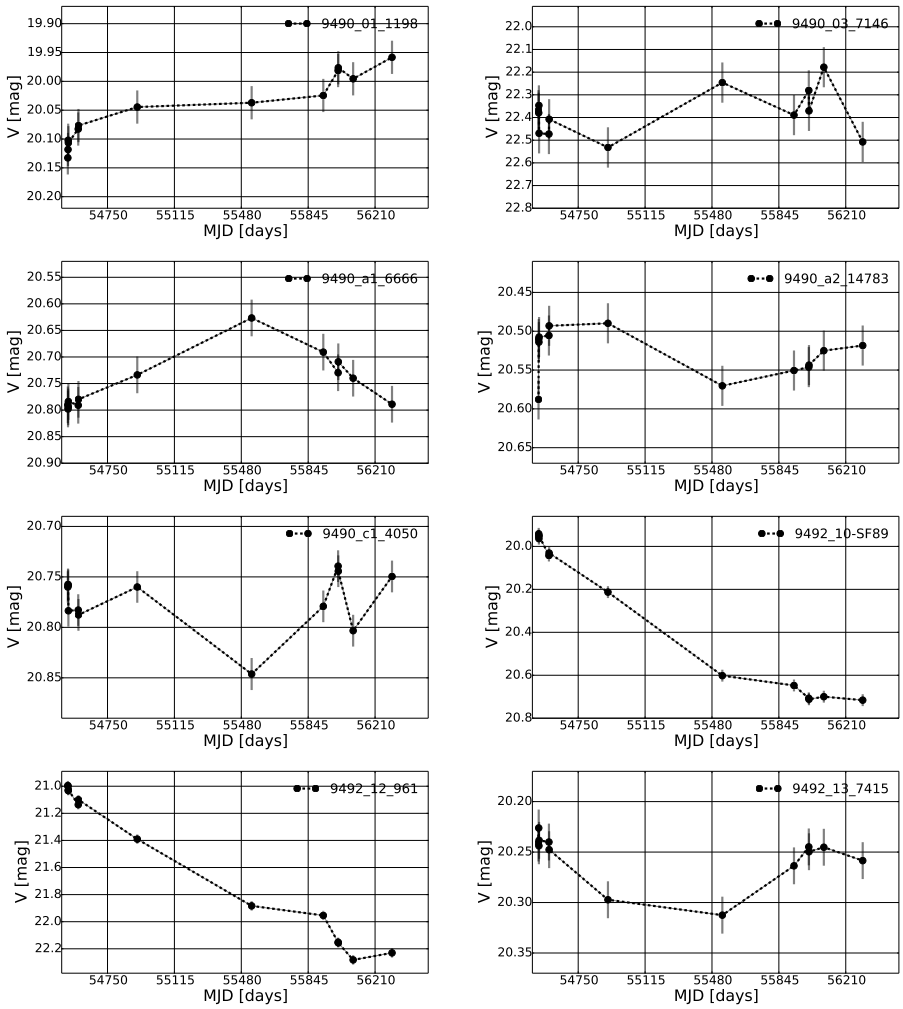

Figure 4.8: The V-band light curves for the hot variables (i.e. targets that meet our criterion for variability and have $(B-V) \leq 0.2$). The x-axis grid lines represent 365 days.

V9 – Figure 4.7 shows the spectrum of V9 which is has strong H and He I in emission. The Hβ and Hα lines have broad, asymmetric wings indicating a strong stellar wind. We do not see any indication of P-Cygni profiles, however, this could be due to the large amount of nebular contamination filling in the absorption lines. O I and Fe II emission lines are present but weak. V9 is located on the periphery of a large star-forming

complex which is not within the *HST*/ACS footprint. However, we have examined the LBT images (not displayed here) and find that though the complex is not resolved, V9 is located far enough away to be in relative isolation. It is unlikely that the spectrum is a composite.

The V-band light curve for V9 indicates that the star has increased in visual brightness by approximately 0.8 magnitudes over the last 4 years. Similar to V4, V9 was originally identified as a variable star in M101 by blinking between photographic images. Table 5 in Sandage & Tammann (1974) provide the minima and maxima: V_{min} = 20.3 (1950) and V_{max} = 19.5 (1927/1947). Our LBT light curve shows that V9 has increased in brightness froms V = 20.2 in 2008 to V = 19.6 in 2012; the most recent data suggest V9 may be fading again. The spectrum for V9 shows that it is a hotter star and so it is unlikely that we are seeing V9 in a state of LBV eruption (which should have the spectrum of a cooler star). Between the spectrum and variability, it is very likely that V9 is an LBV. Continued spectral and photometric monitoring will be crucial for confirmation.

4.4 The Variables Without Spectra

In this section, we present the light curves for the targets without spectra that meet our criterion for variability. We separate the variables by their photometry into three groups: hot (O−B), intermediate (A−F), and cool (G−M). Assuming zero reddening, the selection criteria for our groups corresponds to $(B-V) < 0$, $0 < (B-V) < 0.9$, and $(B-V) > 0.9$, respectively. Based on the our estimates of A_V for our spectroscopically confirmed memebers (Table 4.2.1), the majority of the stars are likely to be at least somewhat reddened. Therefore, we have relaxed our selection criteria to: hot [$(B-V) \leq 0.2$], intermediate [$0.2 < (B-V) < 1.0$], and cool [$(B-V) > 1.0$]. When available, we used the *HST*/ACS catalog photometry to assign stars to groups. For targets that were not recovered in the catalog, we used the LBT photometry. We stress that the LBT colors are unlikely to be precise in crowded regions.

We have LBT spectra for many of the stars in this section. However, at the time of this writing, software issues with the reduction and extraction pipeline have prevented us from including the spectral analysis for these stars. Consequently, we cannot determine

the nature of the stars in this section. A future paper will discuss the spectra along with the light curves.

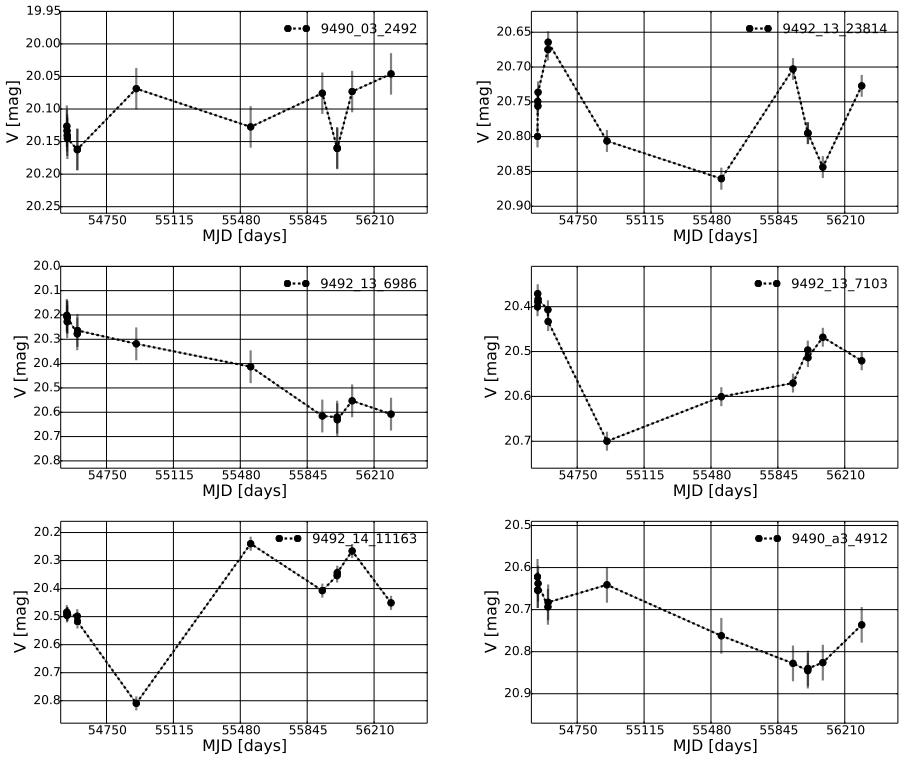

Figure 4.9: The V-band light curves for the intermediate variables (i.e. targets that meet our criterion for variability and have $0.2 < (B - V) \leq 1.0$). The x-axis grid lines represent 365 days.

4.4.1 Hot Variables

Figure 4.8 shows the V-band light curves for all the hot variables. The majority have photometric variability on the order of a few tenths of a magnitude. Two of the stars, 9492_10_SF89 and 9492_12_961, show changes in V-band that are ≈1 magnitude. In both cases, the stars are fading. The *HST*/ACS images were taken in January 2003. In 2003, 9492_10_SF89 and 9492_12_961 had V-band magnitudes of $V = 21.22$ and $V = 20.94$, respectively. In March 2008, the LBT V-band magnitudes did not differ by more than a tenth of a magnitude compared to 2003. Though we do not have data

between 2003 and 2008, the similarities suggest that their recent decline in brightness may be a recent development or alternatively the stars may be semi-periodic. Given their photometric colors and variability, 9492_10_SF89 and 9492_12_961 may be LBVs. Spectral analysis and photometric monitoring will be necessary for confirmation.

4.4.2 Intermediate Variables

The V-band light curves for the variables with $0.2 < (B-V) \leq 1.0$ is provided in Figure 4.9. Our color criteria for the intermediate group could include supergiant Cepheids. To ensure that we have not re-identified any known Cepheids, we have cross-referenced the astrometry of the intermediate variables with the Shappee & Stanek (2011) catalog of M101 Cepheids and removed any matches.

The intermediate variables have photometric properties that overlap with the intermediate supergiants and LBVs in maximum light (Humphreys & Davidson, 1994). It is typical for A to F supergiants to exhibit variability on the order $0.1-0.2$ magnitudes known as α Cygni variability (van Genderen & Sterken, 2002). LBVs in maximum light can also exhibit α Cygni variability, during an extended maximum light, but is higher in amplitude ($\pm$0.5 magnitudes; van Genderen et al., 1997b,a). The variables presented here primarily exhibit α Cygni variability typical of intermediate supergiants.

The stars 9492_13_6986 and 9492_13_11163 show larger amplitude variability that is $\approx$0.5 magnitudes. In the case of 9492_13_11163, the difference between the January 2003 *HST*/ACS and March 2008 LBT V-band magnitudes is quite large: 9492_13_11163 was brighter by 0.5 magnitudes in 2003. Without a spectrum, we cannot say with any certainty that these stars are not typical intermediate-type supergiants, however, their variability suggests they could be LBVs at maximum light. Significant followup observations are necessary for confirmation.

4.4.3 Cool Variables

Finally, we present the V-band light curves for the stars which meet our variability criterion and have $(B-V) > 1.0$. This group consists of red supergiants and, likely, foreground K and M dwarfs. The stars in this group exhibit variability in the V-band that is $0.2-0.4$ magnitudes in amplitude which is typical of K and M supergiants

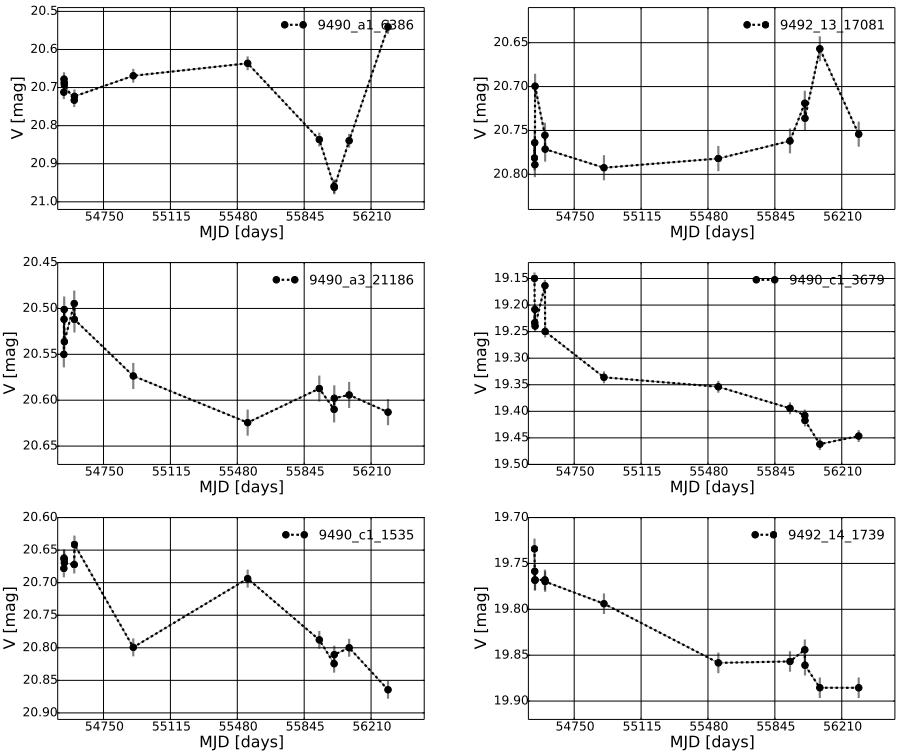

Figure 4.10: The V-band light curves for the cool variables (i.e. targets that meet our criterion for variability and have $(B - V) > 1.0$). The x-axis grid lines represent 365 days.

(Meynet et al., 2011, and references therein), but based on the analysis of Grammer & Humphreys (2013), it is likely that a large fraction of the cool variables are foreground. We present the light curves here, but defer the analysis to a future paper which will include the spectra.

4.5 Summary and Future Work

We obtained optical MMT spectra for 50 of the brightest stars in the direction to M101. We examined the spectra and classified each star by its absorption and emission features. We find that 31 of the 50 targets are members of M101. We separated the members into four groups: hot supergiants, intermediate supergiants, emission-line stars, and candidate LBVs.

In addition to spectroscopy, we have obtained multi-epoch $UBVR$ photometry for all stars with $V \lesssim 20.5$[3]. Of the confirmed members of M101, 8 of the 31 met our criterion for variability. We present new light curves for the known LBV candidates, V2, V4, and V9, and based on the spectra and light curves, we identify a new candidate: 9492_14_11998.

For the stars without spectra, we separated the variables into three groups: hot, intermediate, and cool. In the hot stars group, we identified eight previously unidentified variables, two of which have V-band variability of ± 1 magnitude and may be LBVs. Of the intermediate stars, we identify four variables which show V-band variability with amplitudes of roughly $0.1 - 0.3$ magnitudes which is typical of intermediate supergiants. In addition, we identify two variables with larger amplitude oscillations and may be LBVs in maximum light. Six cool variables are identified and show V-band variability with amplitudes of $0.2 - 0.4$ magnitudes.

Followup spectra and continued photometric monitoring of V2 and the three LBV candidates will be necessary for confirmation and to determine the nature of their observed variability. Furthermore, when the LBT/MODS reduction pipeline is completed, spectral analysis will shed light on the nature of the blue, intermediate, and cool variables with photometric variations greater than $\sim$0.5 magnitudes.

Table 4.3. Remaining Targets

Catalog ID	Star ID	α_{J2000}	δ_{J2000}	V	$(B-V)$	Variability	LBT/MODS Field
J140219.79+542315.29	9492_13_7415	14:02:19.79	54:23:15.29	20.26	0.16	VR	
J140219.85+542313.67	9492_13_7103	14:02:19.85	54:23:13.67	20.37	0.82	VR	
J140220.43+542313.06	9492_13_6986	14:02:20.43	54:23:13.06	20.48	0.31	BVR	Field 4
J140221.34+542333.72	9492_13_11152	14:02:21.34	54:23:33.72	20.63	1.05	BVR	Field 4
J140225.55+541917.18	9492_14_1816	14:02:25.55	54:19:17.18	20.85	0.15	—	Field 4
J140226.24+541944.04	9492_14_6605	14:02:26.24	54:19:44.04	20.68	0.09	—	Field 4
J140226.53+542335.74	9492_13_11533	14:02:26.53	54:23:35.74	20.23	1.41	$UBVR$	Field 4
J140226.64+541948.25	9492_14_7655	14:02:26.64	54:19:48.25	20.74	0.08	—	
J140226.75+541945.84	9492_14_7028	14:02:26.75	54:19:45.84	20.54	0.49	—	
J140226.97+541951.38	9492_14_8521	14:02:26.97	54:19:51.38	20.78	0.06	—	
J140227.03+541947.64	9492_14_7490	14:02:27.03	54:19:47.64	21.02	0.01	—	
J140227.68+542619.32	9492_12_961	14:02:27.68	54:26:19.32	20.94	0.20	$UBVR$	Field 4
J140231.47+542531.44	9492_13_23814	14:02:31.47	54:25:31.44	20.78	0.82	$UBVR$	
J140232.51+542001.39	9492_14_11163	14:02:32.51	54:20:01.39	20.09	0.47	$UBVR$	
J140234.99+542416.67	9492_13_17081	14:02:34.99	54:24:16.67	20.53	1.35	$UBVR$	Field 4
—	9492_14_1739	14:02:39.24	54:19:16.77	—	—	$UBVR$	
J140248.90+541840.10	9490_c2_10368	14:02:48.90	54:18:40.10	20.74	0.16	—	
J140249.10+541842.08	9490_c2_10564	14:02:49.10	54:18:42.08	20.24	0.13	—	
J140249.39+542359.14	9490_b1_16197	14:02:49.39	54:23:59.14	21.02	0.31	—	Field 3
J140249.83+541924.17	9492_09_3069	14:02:49.83	54:19:24.20	20.88	0.25	—	Field 1
J140250.63+542346.86	9490_a3_15563	14:02:50.63	54:23:46.86	20.63	0.06	—	Field 3
J140251.11+542114.51	9490_03_4663	14:02:51.11	54:21:14.51	20.60	0.49	U	
J140253.82+542319.14	9490_a1_5661	14:02:53.82	54:23:19.14	20.86	-0.04	—	Field 3
J140254.07+541942.89	9490_02_867	14:02:54.07	54:19:42.89	20.73	0.04	U	Field 1
J140256.45+541830.42	9490_a2−SF10	14:02:56.45	54:18:30.42	20.40	0.00	—	Field 1
J140257.81+541750.64	9490_a3_1058	14:02:57.81	54:17:50.64	20.85	0.42	—	Field 1
J140258.34+541656.35	9490_a2_7168	14:02:58.34	54:16:56.35	20.88	0.72	—	Field 1
J140258.67+542242.49	9490_01_7533	14:02:58.67	54:22:42.49	20.77	0.11	—	
	9490_a1_6666	14:02:59.11	54:21:09.22	—	—	VR	
—	9490_a3_21186	14:02:59.99	54:24:36.05	—	—	$UBVR$	Field 3
J140300.13+542156.52	9490_02_3047	14:03:00.13	54:21:56.52	20.47	0.12	—	
J140301.82+541514.87	9490_a2_39	14:03:01.82	54:15:14.87	20.86	0.51	—	Field 1
J140302.00+542329.58	9492_10−SF89	14:03:02.00	54:23:29.58	20.22	0.18	$UBVR$	Field 3
J140302.70+542308.88	9492_10−SF162	14:03:02.70	54:23:08.88	21.38	0.92	—	Field 3
J140306.60+541924.56	9490_02_584	14:03:06.60	54:19:24.56	20.68	0.14	—	Field 1
J140306.84+542147.95	9490_02_2905	14:03:06.84	54:21:47.95	19.96	-0.06	—	
J140309.76+542330.52	9490_a3_12519	14:03:09.76	54:23:30.52	20.35	0.03	—	Field 3
J140311.11+541623.59	9490_a2−SF112	14:03:11.11	54:16:23.59	21.12	0.05	—	Field 1
J140312.18+542006.40	9490_02_1378	14:03:12.18	54:20:06.40	20.42	0.01	—	
J140312.52+541752.55	9490_a2_15263	14:03:12.52	54:17:52.55	20.92	0.09	—	
J140312.62+541749.85	9490_a2_14783	14:03:12.62	54:17:49.85	20.70	0.20	V	Field 1
J140312.81+541732.17	9490_a2_12011	14:03:12.81	54:17:32.17	20.84	0.13	—	
J140315.13+542151.19	9490_01_7652	14:03:15.13	54:21:51.19	20.62	0.13	—	Field 3
J140315.66+541907.72	9492_10_5190	14:03:15.66	54:19:07.72	21.30	-0.01	—	Field 1
J140316.03+541756.22	9490_a2_15969	14:03:16.03	54:17:56.22	20.28	0.23	U	Field 1
J140317.37+542506.89	9490_03_6586	14:03:17.37	54:25:06.89	20.47	1.34	U	Field 3
J140317.62+542332.53	9490_03−SF55	14:03:17.62	54:23:32.53	21.27	0.06	—	Field 3
J140317.99+541712.08	9490_a2_9284	14:03:17.99	54:17:12.02	21.29	0.00	—	Field 1
—	9490_a3_4912	14:03:19.25	54:21:49.12	—	—	$UBVR$	Field 3
J140320.92+541705.60	9490_a2_8459	14:03:20.92	54:17:05.60	20.53	0.38	U	
J140321.42+542344.09	9490_03_1988	14:03:21.42	54:23:44.09	20.46	1.26	—	
J140321.81+542346.00	9490_03_2120	14:03:21.81	54:23:46.00	20.31	0.11	—	Field 3
J140323.24+542042.68	9490_a2_17072	14:03:23.24	54:20:42.68	20.82	0.30	—	Field 2

Table 4.3 (cont'd)

Catalog ID	Star ID	α_{J2000}	δ_{J2000}	V	$(B-V)$	Variability	LBT/MODS Field
J140324.77+541726.74	9490_a1_1294	14:03:24.77	54:17:26.74	20.90	0.15	—	Field 1
J140325.40+541939.04	9490_a1_6386	14:03:25.40	54:19:39.04	20.59	1.40	BVR	
J140325.45+542522.94	9490_03_7146	14:03:25.45	54:25:22.94	20.66	0.02	V	Field 3
J140325.57+542353.02	9490_03_2492	14:03:25.57	54:23:53.02	20.29	0.64	V	Field 3
J140325.58+541957.65	9490_01_1198	14:03:25.58	54:19:57.60	20.58	0.10	VR	Field 2
J140325.70+542514.88	9490_03_6836	14:03:25.70	54:25:14.88	20.27	0.04	R	Field 3
J140325.90+542420.88	9490_03_4390	14:03:25.90	54:24:20.88	22.61	0.01	—	Field 3
J140325.98+542422.82	9490_03_4520	14:03:25.98	54:24:22.82	20.02	0.41	—	
J140326.19+541939.47	9490_c1_1362	14:03:26.19	54:19:39.47	20.81	0.66	—	Field 2
J140326.21+542047.87	9490_01_4031	14:03:26.21	54:20:47.87	20.67	0.01	U	
J140326.38+542411.30	9490_02_2637	14:03:26.38	54:24:11.30	20.69	-0.04	—	Field 3
J140326.45+542038.36	9490_01_3379	14:03:26.45	54:20:38.36	20.65	0.07	—	
J140327.03+542346.36	9490_03_2142	14:03:27.03	54:23:46.36	21.08	-0.06	—	
J140327.10+542046.79	9490_01_3977	14:03:27.10	54:20:46.79	20.82	0.09	—	Field 2
J140327.60+541846.80	9490_a1_4198	14:03:27.60	54:18:46.80	20.75	0.01	—	
J140327.67+542340.92	9490_03_1822	14:03:27.67	54:23:40.92	19.69	0.40	—	
J140327.71+541844.93	9490_a1_4062	14:03:27.71	54:18:44.93	20.89	0.05	—	
J140328.82+542458.03	9490_03_6315	14:03:28.82	54:24:58.03	20.15	0.84	U	
J140329.43+541809.97	9490_a3_7830	14:03:29.43	54:18:09.97	20.54	0.25	—	
J140329.51+541712.23	9490_a1_627	14:03:29.51	54:17:12.23	20.81	0.19	—	
J140330.07+541853.28	9490_c1_1485	14:03:30.07	54:18:53.28	20.52	0.30	U	Field 2
J140330.32+541954.19	9490_01_991	14:03:30.32	54:19:54.19	20.80	-0.06	—	
J140330.61+542424.48	9490_c2_2831	14:03:30.61	54:24:24.48	20.45	0.77	UV	Field 3
—	9490_b2_14	14:03:30.91	54:14:10.48	—	—	—	
—	9490_b1_14323	14:03:32.13	54:22:00.47	—	—	—	Field 2
J140333.74+541854.61	9490_a1_4710	14:03:33.74	54:18:54.61	20.57	0.48	—	Field 2
—	9490_b1_3388	14:03:40.92	54:19:02.68	—	—	—	Field 2
—	9490_03_3779	14:03:41.57	54:19:08.47	—	—	UB	
J140342.85+542336.96	9490_c1_4050	14:03:42.85	54:23:36.96	20.65	0.20	UBV	
J140346.10+541959.52	9490_b1_8183	14:03:46.10	54:19:59.52	20.77	0.07	—	Field 2
—	9490_c1_1535	14:03:46.17	54:16:15.68	—	—	$UBVR$	
—	9490_c1_3069	14:03:47.38	54:22:29.50	—	—	$UBVR$	
—	9490_c1_3679	14:03:49.63	54:23:8.74	—	—	BV	
J140351.93+542152.78	9490_c1_1292	14:03:51.93	54:21:52.78	20.33	-0.02	—	
J140355.88+542229.46	9490_c1_3067	14:03:55.88	54:22:29.46	20.30	0.11	—	

Note. — Remaining targets, some of which were observed with LBT/MODS. Units of right ascension are hours, minutes, and seconds; units of declination are degrees, minutes, and seconds. Sources are sorted by increasing RA. The *HST*/ACS magnitudes, for recovered sources, are provided.

[3] Based off aperture photometry performed by the HLA. We later performed PSF photometry and show that some of the targets are blends and thus their V-band magnitudes are much fainter than 20.5. See §2 for details.

Chapter 5

Summary

Using archival *BVI HST*/ACS images we have created a catalog of stars covering a large fraction of the M101 optical disk. Unprecedented spatial resolution paired with excellent characterization of the *HST*/ACS point spread function and detectors have allowed for the minimization in the numbers of non-stellar sources, such as background galaxies and unresolved clusters, and the ability to maintain high photometric precision and depth even in regions where stellar crowding is extreme.

From the catalog, we have identified luminous massive star candidates, for future study, using color-magnitude and color-color diagrams. We separated the luminous massive star candidates into three subsets: luminous OB type stars and blue supergiants, yellow supergiants, and red supergiants. We modeled the foreground contamination in the direction of M101 using the Besançon Galactic population synthesis model (Robin et al., 2003) and conclude that using our selection criteria, $\sim 100\%$ of the 25,603 luminous OB type stars and blue supergiants, $60-80\%$ of the 3,105 yellow supergiants, and $85-95\%$ of the 2,294 red supergiants are likely members of M101. Examining the spatial distributions of our candidates, we find that the blue and yellow supergiants share a common distribution however the red supergiants are more common in the outer parts of the galaxy, supported by color-magnitude diagrams at various radii. Additionally, we show that the ratio of blue to red supergiants (B/R ratio) declines smoothly with radius. Converting radius to metallicity, we observe a decrease of roughly two orders of magnitude over 0.5 dex in metallicity.

Furthermore, we derive the star formation history (SFH) of the resolved massive star

population in the catalog. We separate stars radially into five 2′-wide annuli. Binning the SFHs into time frames corresponding to stellar populations traced by Hα ($<$ 10 Myr), FUV ($<$ 35 Myr), and NUV ($<$ 100 Myr) emission, we determined radial SFR profiles. We fit exponential functions to the radial SFR profiles and compared them to the radial emission profiles themselves. We find that radial SFR profiles and the radial emission profiles have best-fit scale lengths that are in excellent agreement. Our results show that the $<$ 35 Myr radial SFR profile is considerably more extended than that of the $<$ 10 Myr radial SFR profile. Examining the age at which the $50\%, 75\%, 85\%$, and 95% mass fractions are attained, we find that the mass fraction for stars $<$ 16 Myr old is $15\% - 35\%$ in the inner regions, compared to less than 5% in the outer regions. The mass fraction for stars $<$ 35 Myr old is greater than 50% in the inner regions and greater than 25% in the outer regions. These findings are consistent with a radially increasing stellar age gradient which provides a natural explanation for the lack of Hα emission at large radius. However, our data cannot rule out alternative explanations such as statistical sampling of the IMF or a strongly truncated IMF.

Taking the just-derived SFH into account, we model the B/R ratio in all 5 of our annuli. We then compare the predicted B/R ratios to the observed values. Our results show that holding the SFH constant, the predicted B/R ratios decrease with metallicity, a trend which is opposite to observations. If we include the radially variable SFH, the behavior of the B/R ratio is similar to observations. Overall, we find that our modeled B/R ratios closely match the observed values at large radii (low metallicity) but are discrepant at small radii (high metallicity), which we attribute to our use of non-rotating stellar isochrones.

High-precision photometry is a powerful tool for the study of stellar populations as a whole but spectra of individual stars is required to determine their evolutionary state, mass loss properties, luminosity, etc. Therefore, we obtained optical MMT spectra for 50 of the brightest stars in the direction to M101. We examined the spectra and classified each star by its absorption and emission features. We find that 31 of the targets are members of M101, which we then separate into four groups: hot supergiants, intermediate supergiants, emission-line stars, and LBVs.

In addition to spectroscopy, we have obtained multi-epoch $UBVR$ photometry for stars with $V \lesssim 20.5$ (see text). Of the confirmed members of M101, 8 of the 31 met

our criterion for variability. We present light curves for the known LBV candidates, V2, V4, and V9, and introduce a new candidate: 9492_14_11998.

For the stars without spectra, we separated the variables into three groups: hot, intermediate, and cool. In the hot stars group, we identified eight previously unidentified variables, two of which have V-band variability of ± 1 magnitude and may be LBVs. Of the intermediate stars, we identify four variables which show V-band variability with amplitudes of roughly $0.1 - 0.3$ magnitudes which is typical of intermediate supergiants. In addition, we identify two variables with larger amplitude oscillations and may be LBVs in maximum light. Six cool variables are identified and show V-band variability with amplitudes of $0.2 - 0.4$ magnitudes.

Followup spectra and continued photometric monitoring of V2, V4, V9, and 9492_14_11998 will be necessary for confirmation and to determine the nature of their observed variability. Furthermore, when the LBT/MODS reduction pipeline is completed, spectral analysis will shed light on the nature of the blue, intermediate, and cool variables with photometric variations greater than $\sim$0.5 magnitudes.

References

Alard, C. 2000, A&AS, 144, 363

Alberts, S., et al. 2011, ApJ, 731, 28

Allende Prieto, C., Lambert, D. L., & Asplund, M. 2001, ApJ, 556, L63

Barmby, P., Kuntz, K. D., Huchra, J. P., & Brodie, J. P. 2006, AJ, 132, 883

Bertelli, G., Bressan, A., Chiosi, C., Fagotto, F., & Nasi, E. 1994, A&AS, 106, 275

Bik, A., Lamers, H. J. G. L. M., Bastian, N., Panagia, N., & Romaniello, M. 2003, A&A, 397, 473

Boissier, S., et al. 2007, ApJS, 173, 524

Bond, H. E. 2011, ApJ, 737, 17

Bosma, A., Goss, W. M., & Allen, R. J. 1981, A&A, 93, 106

Bresolin, F., Kennicutt, R. C. J., & Stetson, P. B. 1996, AJ, 112, 1009

Brunish, W. M., Gallagher, J. S., & Truran, J. W. 1986, AJ, 91, 598

Cardelli, J. A., Clayton, G. C., & Mathis, J. S. 1989, ApJ, 345, 245

Castor, J. I., Abbott, D. C., & Klein, R. I. 1975, ApJ, 195, 157

Chandar, R., Ford, H. C., & Tsvetanov, Z. 2001, AJ, 122, 1330

Chen, C. H. R., Chu, Y. H., & Johnson, K. E. 2005, ApJ, 619, 1

Conti, P. S. 1978, ARA&A, 16, 371

Crowther, P. A., Lennon, D. J., & Walborn, N. R. 2006, A&A, 446, 279

Dohm-Palmer, R. C., & Skillman, E. D. 2002, AJ, 123, 1433

Dolphin, A. E. 2000, PASP, 112, 1383

Dolphin, A. E. 2002, MNRAS, 332, 91

Eggenberger, P., Meynet, G., & Maeder, A. 2002, A&A, 386, 576

Fabricant, D. G., Fata, R. G., & Epps, H. W. 1998, in Society of Photo-Optical Instrumentation Engineers (SPIE) Conference Series, Vol. 3355, Optical Astronomical Instrumentation, ed. S. D'Odorico, 232–241

Flower, P. J. 1977, A&A, 54, 31

—. 1996, ApJ, 469, 355

Franchetti, N. A., et al. 2012, AJ, 143, 85

Fraser, M., et al. 2013, MNRAS, 433, 1312

Gal-Yam, A., & Leonard, D. C. 2009, Nature, 458, 865

Gal-Yam, A., et al. 2007, ApJ, 656, 372

Gallart, C., Freedman, W. L., Aparicio, A., Bertelli, G., & Chiosi, C. 1999, AJ, 118, 2245

García-Benito, R., Pérez, E., Díaz, Á. I., Maíz Apellániz, J., & Cerviño, M. 2011, AJ, 141, 126

Giallongo, E., et al. 2008, A&A, 482, 349

Goddard, Q. E., Kennicutt, R. C., & Ryan-Weber, E. V. 2010, MNRAS, 405, 2791

Gogarten, S. M., Dalcanton, J. J., Murphy, J. W., Williams, B. F., Gilbert, K., & Dolphin, A. 2009, ApJ, 703, 300

Grammer, S., Humphreys, R. K., & Gerke, . 2014, In Prep

Grammer, S., & Humphreys, R. M. 2013, AJ, 146, 114

—. 2014, The Astronomical Journal, 148, 58

Harris, J., & Zaritsky, D. 2004, AJ, 127, 1531

Hartwick, F. D. A. 1970, Astrophys. Lett., 7, 151

Hernandez, X., Valls-Gabaud, D., & Gilmore, G. 1999, MNRAS, 304, 705

Hodge, P. W., Gurwell, M., Goldader, J. D., & Kennicutt, R. C. J. 1990, ApJS, 73, 661

Holtzman, J. A., et al. 1999, AJ, 118, 2262

Hoopes, C. G., Walterbos, R. A. M., & Bothun, G. D. 2001, ApJ, 559, 878

Humphreys, R. M. 1979, ApJS, 39, 389

—. 1980, ApJ, 241, 598

Humphreys, R. M., & Aaronson, M. 1987, AJ, 94, 1156

Humphreys, R. M., Aaronson, M., Lebofsky, M., McAlary, C. W., Strom, S. E., & Capps, R. W. 1986, AJ, 91, 808

Humphreys, R. M., & Davidson, K. 1979, ApJ, 232, 409

—. 1984, Science, 223, 243

Humphreys, R. M., & Davidson, K. 1994, /pasp, 106, 1025

Humphreys, R. M., Davidson, K., Grammer, S., Kneeland, N., Martin, J. C., Weis, K., & Burggraf, B. 2013, ApJ, 773, 46

Humphreys, R. M., Davidson, K., & Smith, N. 1999, PASP, 111, 1124

Humphreys, R. M., & McElroy, D. B. 1984, ApJ, 284, 565

Humphreys, R. M., & Strom, S. E. 1983, ApJ, 264, 458

Humphreys, R. M., Weis, K., Davidson, K., Bomans, D. J., & Burggraf, B. 2014, ApJ, 790, 48

Ivezić, Ž., et al. 2007, AJ, 134, 973

Jordi, K., Grebel, E. K., & Ammon, K. 2006, A&A, 460, 339

Kennicutt, Jr., R. C. 1984, ApJ, 287, 116

—. 1988, ApJ, 334, 144

—. 1998, ApJ, 498, 541

Kennicutt, R. C. J., Bresolin, F., & Garnett, D. R. 2003, ApJ, 591, 801

Khan, R., Stanek, K. Z., Prieto, J. L., Kochanek, C. S., Thompson, T. A., & Beacom, J. F. 2010, ApJ, 715, 1094

Kochanek, C. S., Beacom, J. F., Kistler, M. D., Prieto, J. L., Stanek, K. Z., Thompson, T. A., & Yüksel, H. 2008, ApJ, 684, 1336

Koda, J., Yagi, M., Boissier, S., Gil de Paz, A., Imanishi, M., Donovan Meyer, J., Madore, B. F., & Thilker, D. A. 2012, ApJ, 749, 20

Kuntz, K. D., Snowden, S. L., Pence, W. D., & Mukai, K. 2003, ApJ, 588, 264

Lai, S.-P., Chu, Y.-H., Chen, C.-H. R., Ciardullo, R., & Grebel, E. K. 2001, ApJ, 547, 754

Langer, N., & Maeder, A. 1995, A&A, 295, 685

Larsen, S. S. 2002, AJ, 124, 1393

Lee, J. C., et al. 2011, ApJS, 192, 6

Lin, L., Zou, H., Kong, X., Lin, X., Mao, Y., Cheng, F., Jiang, Z., & Zhou, X. 2013, ApJ, 769, 127

Lupton, W. 1998, in Society of Photo-Optical Instrumentation Engineers (SPIE) Conference Series, Vol. 3351, Telescope Control Systems III, ed. H. Lewis, 210–221

Luridiana, V., & Peimbert, M. 2001, ApJ, 553, 633

Maeder, A., Lequeux, J., & Azzopardi, M. 1980, A&A, 90, L17

Margutti, R., et al. 2013, ArXiv e-prints

Marigo, P., Girardi, L., Bressan, A., Groenewegen, M. A. T., Silva, L., & Granato, G. L. 2008, A&A, 482, 883

Martin, C. L., & Kennicutt, Jr., R. C. 2001, ApJ, 555, 301

Massey, P. 1998, ApJ, 501, 153

Massey, P., & Johnson, O. 1998, ApJ, 505, 793

Mauerhan, J. C., et al. 2013, MNRAS, 430, 1801

McQuinn, K. B. W., Skillman, E. D., Dalcanton, J. J., Dolphin, A. E., Holtzman, J., Weisz, D. R., & Williams, B. F. 2011, ApJ, 740, 48

Meurer, G. R., et al. 2009, ApJ, 695, 765

Meylan, G., & Maeder, A. 1982, A&A, 108, 148

Meynet, G., Georgy, C., Hirschi, R., Maeder, A., Massey, P., Przybilla, N., & Nieva, M.-F. 2011, Bulletin de la Societe Royale des Sciences de Liege, 80, 266

Mihos, J. C., Harding, P., Spengler, C. E., Rudick, C. S., & Feldmeier, J. J. 2013, ApJ, 762, 82

Mokiem, M. R., et al. 2007, A&A, 465, 1003

Morrissey, P., et al. 2007, The Astrophysical Journal Supplement Series, 173, 682

Oskinova, L. M. 2005, MNRAS, 361, 679

Pastorello, A., et al. 2007, Nature, 447, 829

—. 2013, ApJ, 767, 1

Pellerin, A. 2006, AJ, 131, 1

Pleuss, P. O., Heller, C. H., & Fricke, K. J. 2000, A&A, 361, 913

Pogge, R. W., et al. 2006, in Society of Photo-Optical Instrumentation Engineers (SPIE) Conference Series, Vol. 6269, Society of Photo-Optical Instrumentation Engineers (SPIE) Conference Series

Robin, A. C., Reylé, C., Derrière, S., & Picaud, S. 2003, A&A, 409, 523

Rosa, M. R., & Benvenuti, P. 1994, A&A, 291, 1

Salpeter, E. E. 1955, ApJ, 121, 161

Sandage, A. 1983, AJ, 88, 1569

Sandage, A., & Tammann, G. A. 1974, ApJ, 194, 223

Schlegel, D. J., Finkbeiner, D. P., & Davis, M. 1998, ApJ, 500, 525

Shappee, B. J., & Stanek, K. Z. 2011, ApJ, 733, 124

Shara, M. M., Bibby, J. L., Zurek, D., Crowther, P. A., Moffat, A. F. J., & Drissen, L. 2013, ArXiv e-prints

Sirianni, M., et al. 2005, PASP, 117, 1049

Skillman, E. D., Tolstoy, E., Cole, A. A., Dolphin, A. E., Saha, A., Gallagher, J. S., Dohm-Palmer, R. C., & Mateo, M. 2003, ApJ, 596, 253

Stothers, R., & Chin, C.-W. 1969, ApJ, 158, 1039

Sun, W., Chen, Y., Feng, L., Chu, Y.-H., Chen, C.-H. R., Wang, Q. D., & Li, J.-T. 2012, ApJ, 760, 61

Thilker, D. A., et al. 2005, ApJ, 619, L79

—. 2007, ApJS, 173, 538

Thompson, T. A., Prieto, J. L., Stanek, K. Z., Kistler, M. D., Beacom, J. F., & Kochanek, C. S. 2009, ApJ, 705, 1364

Tosi, M., Greggio, L., Marconi, G., & Focardi, P. 1991, AJ, 102, 951

Turatto, M., Cappellaro, E., Danziger, I. J., Benetti, S., Gouiffes, C., & della Valle, M. 1993, MNRAS, 262, 128

Úbeda, L., Maíz-Apellániz, J., & MacKenty, J. W. 2007, AJ, 133, 932

van den Bergh, S. 1968, JRASC, 62, 219

Van Dyk, S. D. 2005, in Astronomical Society of the Pacific Conference Series, Vol. 332, The Fate of the Most Massive Stars, ed. R. Humphreys & K. Stanek, 47

Van Dyk, S. D., & Matheson, T. 2012, in Astrophysics and Space Science Library, Vol. 384, Eta Carinae and the Supernova Impostors, ed. K. Davidson & R. M. Humphreys, 249

van Genderen, A. M., de Groot, M., & Sterken, C. 1997a, A&AS, 124, 517

van Genderen, A. M., & Sterken, C. 2002, A&A, 386, 926

van Genderen, A. M., Sterken, C., & de Groot, M. 1997b, A&A, 318, 81

Vázquez, G. A., Leitherer, C., Schaerer, D., Meynet, G., & Maeder, A. 2007, ApJ, 663, 995

Vink, J. S. 2012, in Astrophysics and Space Science Library, Vol. 384, Astrophysics and Space Science Library, ed. K. Davidson & R. M. Humphreys, 221

Walker, M. F. 1964, AJ, 69, 744

Wang, Q. D., Immler, S., & Pietsch, W. 1999, ApJ, 523, 121

Williams, R. M., & Chu, Y.-H. 1995, ApJ, 439, 132

Zaritsky, D., & Christlein, D. 2007, AJ, 134, 135